| | |
|---|---|
| Title | Study on on-demand functionalization of hydrogel surfaces by force-induced rapid microstructure growth |
| Author(s) | Mu, Qifeng |
| Citation | 北海道大学. 博士(ソフトマター科学) 甲第15228号 |
| Issue Date | 2022-12-26 |
| DOI | 10.14943/doctoral.k15228 |
| Doc URL | http://hdl.handle.net/2115/90623 |
| Type | theses (doctoral) |
| File Information | Qifeng_Mu.pdf |

**Doctoral Dissertation**

# Study on on-demand functionalization of hydrogel surfaces by force-induced rapid microstructure growth
# (力誘起急速微細構造成長によるハイドロゲル表面のオンデマンド機能化に関する研究)

**Qifeng Mu**

Laboratory of Soft and Wet Matter

Division of Soft Matter

Graduate School of Life Science

December 2022

## Content

**List of important abbreviations**

| | |
|---|---|
| DN | Double-network |
| SN | Single-network |
| (P)AAm | (Poly)acrylamide |
| (P)NaAMPS | (Poly) 2-Acrylamido-2-methylpropanesulfonic acid sodium salt |
| (P)AMPS | (Poly) 2-Acrylamido-2-methylpropanesulfonic acid |
| MBA | *N,N′*-Methylenebisacrylamide |
| ANS | 8-Anilino-1-naphthalenesulfonic acid |
| NIPAm | *N*-isopropylacrylamide |
| AAc | Acrylic acid |
| NaSS | Sodium *p*-styrenesulfonate |
| MPTC | 3-(methacryloylamino)propyltrimethylammonium chloride |
| Si-PET | Silicon-coated polyethylene glycol terephthalate |
| $D_2O$ | Deuterium oxide |
| UV | Ultraviolet |
| ATR FT-IR | Attenuated total reflectance Fourier-transform infrared spectroscopy |
| ESR | Electron Spin Resonance |
| AFM | Atomic force microscope |

**List of important symbols**

| | |
|---|---|
| $T_\mathrm{c}$ | Fracture energy |
| $\sigma$ | Cross-section area |
| $W$ | Energy |
| $\mathbf{v}$ | Number density of elastically active network strand |
| $R_0$ | Average end-to-end length of an elastically active network strand in undeformed state |
| $n$ | Average number of repeat units along the bridging strand |
| $U$ | Energy that is stored in each repeat unit when the bridging strand scission |
| $E_b$ | Bond dissociation energy |
| $\Delta U_{act}$ | Mechanical activation energy of one carbon-carbon bond |
| $C_1$ | Feed monomer concentration for the first network |
| $x_1$ mol% | Percentage of crosslinker to monomer for the first network |
| $\mathrm{x}_1$ mol% | Percentage of initiator to monomer for the first network |
| $C_2$ | Feed monomer concentration for the second network |
| $x_2$ mol% | Percentage of crosslinker to monomer for the second network |
| $x_2$ mol% | Percentage of initiator to monomer for the second network |
| $E$ | Surface elastic modulus |
| $A$ | Absorbance |

| | |
|---|---|
| $l$ | Sample thickness |
| $\epsilon$ | Molar absorption coefficient |
| $c$ | Molar concentration of the attenuating substances |
| $I_0$ | Intensity of incident infrared light |
| $I$ | Intensity of transmitted infrared light |
| $S$ | Normalized absorption peak area |
| $\alpha$ | Proportional constant |
| $H$ | Height of microstructure |
| $d$ | Diameter of microstructure |
| $\theta_{Res}$ | Receding angle |
| $\theta_{Adv}$ | Advancing angle |

# Chapter 1: Brief Introduction

Biological systems have various mechanisms for productive responding to external mechanical forces. The unique biological structures are not mere static systems. Instead, they are actively responding to the force stimuli from the external environment, constantly adjusting their architecture to adapt their properties to the surroundings. These biological tissues or creatures could be concluded as open, nonequilibrium systems allowing for unlimited variations. Specifically, cephalopods could display dynamic skin patterns in response to stimuli for communication and camouflage. These microstructures on creature surfaces are usually formed via a surface growth mechanism, which provides us elegant paradigms for designing new biomimetic materials with specific functions and promising applications. Another a good example of this mechanobiological approach (i.e. dynamic growing) is observed in human bone development. Human bone tissues can fine-tune their properties (e.g. strength, modulus, porous and density) in response to changes in the mechanical environments thanks to the permanent remodeling of their constitutive materials. Many synthetic materials, such as polymers, or hydrogels, however, are usually considered static with no internal structures remodeling or no surface microstructures regeneration once prepared. When a destructive or cyclic mechanical force is applied to a typical synthetic polymeric material, bond scission occurs, free radical production, and the mechanical properties are compromised. In recent years, self-growing or self-strengthening polymeric materials through mechanochemical transduction have been intensely pursued to increase the lifetime and sustainability of the polymeric materials. However, these mechanochemical strategies are only limited to remodel the internal network structures through sacrificial bonds and force-triggered radical polymerization. Recent developments in the field of polymer mechanochemistry indicate that there has been a shift in the landscape of modern polymer mechanochemistry from being “destructive” to “productive”. So, can we create a biomimetic soft material surface, analogous to the skin of creatures, which adopts the destructive mechanical force to renew their surface microstructures and on-demand properties? What is the special effect of monomer species on the “grown” microstructures? How fast is the force-triggered radical polymerization? How such microstructures or patterns will affect the surface properties of hydrogels? What are the potential applications for the micropatterned hydrogel surfaces in bionics or life sciences?

The research devotes to finding a novel strategy for creating microstructures on double-network (DN) hydrogel surfaces with force-triggered radical polymerization for on-demand functions, confirming the displacement thresholds for regioselective indentation damage on the DN hydrogel surfaces, revealing the quantitative calculation of mechanoradical production in the local process zones. The specific mechanically responsive systems for productive mechanochemistry of DN hydrogels enrich the chemistry and physical microstructures of hydrogel surfaces. The multifunctional micropatterns with a variety of geometries and chemistries show promising biomimetic applications, such as effectively supporting cell selective adhesion and enhanced myogenesis.

As mentioned above, our research goal is to study the productive use of destructive mechanical force to produce radicals on DN hydrogel surfaces for physically and chemically remodeling the material surfaces and on-demand functions.

In chapter 2, the research background of this research topic (force-triggered rapid microstructures growth on the hydrogel surfaces for on-demand functions) is summarized.

In chapter 3, the synthetic produce is included, and fundament mechanical properties of various DN hydrogels are quantified by the mechanical testing.

In chapter 4, reswelling properties and revealed internal fracture of the force-triggered damage zone on hydrogel surfaces are systematically studied. The reswelling of the damaged zone confirms bond scission and radical production. The mechanoradical concentration is estimated as $2.9\times10^{-5}$ M when the indentation depth is 1000 μm. In chapter 5, rapid microstructure growth on DN hydrogel surfaces triggered by mechanical force is found, and the quantitative relationship between microstructure feature height and hysteresis energy is systematically studied. We found that the force-triggered rapid strategy is chemical species-dependent, spatially controllable, and allows fine modulation of the size and composition of microstructures. In chapter 6, various complex physical and/or chemical micropatterns on DN hydrogel surfaces are created by the force-triggered rapid microstructure growth. The results reveal that the micropatterned DN hydrogels could be used not only for directed growth and enhanced myogenesis of cell but also for water droplet directional transport. In chapter 7, the main findings and conclusions are included based on the overall work.

# Chapter 2: Background

## 2.1. Dynamic self-growing systems in nature

Living organisms can create various fascinating microstructures via a self-growth mode. The formation of microstructures and patterns through a growth model in the natural world has long been a source of fascination. Impressive examples are many and varied, ranging from the self-growth of living organisms to cell proliferation and differentiation, and from the formation of a coral reef to crystal growth. Specifically, human tissues such as muscle and bone, these biological structures are not mere static systems. Instead, they adapt to cyclic mechanical loading by adding new matter according to the loading location, energy, frequency, and time scale, a process known as mechanical adaptive remodeling or dynamic self-growing (**Figure 2-1**)[1,2]. This metabolic process allows muscle and bone to adaptively strengthen when subjected to external forces, thereby preventing structural fracture, and improving the overall mechanical strength. It is interesting to note that most metabolic process dependent on the mechanotransduction pathways. The ability to change as a mechanoresponse to the nature of their surrounding environment is capital in the development and the subsistence of living tissues. In addition to the self-growing in the bulk of living tissues, the soft and wet skins of Echinodermata (e.g. starfish and sea cucumber) or cephalopods (e.g. cuttlefish, octopuses, and squids) can grow and display dazzling patterns of shapes and colors for signaling or active camouflage in response to external stimuli (e.g. force, light, heat, moisture or electrical potential) (**Figure 2-2**)[3-5]. These natural self-growing patterns and display strategies, if successfully implemented in engineering intelligent devices, would greatly benefit various fields such as stretchable electronics, dynamic camouflage, and biomedical devices.

## 2.2. Mechanical degradation and mechanoradicals

### 2.2.1 History of mechanical degradation and mechanoradicals

Most biological systems respond to external mechanical stimuli in a self-growing manner. The biology mechanochemical transduction is highly desirable and has been the source inspiration for the scientific research in the field of polymer mechanochemistry. In recent years, polymer mechanochemistry is an emerging genre of research that investigates the use of destructive mechanical force to trigger selective chemical transformation. In the 1930s, Staudinger and co-workers observed a molecular weight reduction of poly(styrene) when subjected to mechanical mastication, and the scission of covalent bonds in the main chain was first considered[6,7]. Later in the 1950s, researchers including Melville discovered that polymer chain scission caused the ultrasonic degradation in dilute polymer solutions[8]. The mechanoradicals produced by homolytic scission of carbon-carbon (C-C) covalent bonds along the polymer backbone under mechanical force were later experimentally demonstrated by Sohma et al. using Electron Spin Resonance (ESR) or named Electron Paramagnetic Resonance (EPR)[9]. Polymer mechanochemistry, as an important branch in the modern chemistry, is based on studies of mechanoradicals, which are defined as free radicals produced by mechanical force. In fact, any mechanical treatment (e.g. ball-milling, swelling, cycle freezing-thawing, turbulent flowing, cutting, stretching, compression and indentation) causing homolytic cleavage of polymer backbones may produce mechnaoradicals. In a mechanoradical, a proton bonded to a carbon atom having an unpaired electron is named an $\alpha$-proton, while if a proton bonded to an adjacent carbon to the unpaired electron site is called a $\beta$-proton (**Figure 2-3**)[9].

### 2.2.2 Methods to detect free radicals in polymer

Free radicals are highly reactive and unstable substances, it is a challenge for researchers to separate or detect free radicals directly, because free radicals can easily gain or lose electrons from their surroundings. In order to capture highly active free radicals, most researchers adopt a strategy of first stabilizing and detecting later, that is, using a free radical scavenger (e.g. *p*-benzoquinone[10], 3,3,5,5-Tetramethyl-1-pyrolline-*N*-oxide (TMPO)[11], Butylated hydroxytoluene (BHT)[12], 2,2-Di(4-tert-octylphenyl)-1-picrylhydrazyl (DPPH)[13]). Free radicals can quickly form more stable compounds with the free radical scavengers, so that researchers can carry out subsequent detection and separation. In addition to the specific free radical scavengers, some mechaochemical reaction cascade were reported for sensing free radicals by fluorescence or color change in materials. Fitch and co-workers proposed a novel strategy to detect the mechanoradical using 3′-(p-aminophenyl) fluorescein (APF)[14]. The homolytic cleavage of covalent bonds in polymer chains produce radicals that can react with water to form hydroxyl radicals and $H_2O_2$. Hydroxyl radical can then react with the APF, producing the green-emissive fluorescein (**Figure 2-4**). This strategy can detect bond breakage with less than 5 kPa of mechanical compression, even when the mechanical properties appear unchanged by simple mechanical testing. The lower detection threshold is the biggest advantage of this strategy. Baytekin and Matsuda used the classical Fenton color reaction to detect the mechanoradical (**Figure 2-5**). Ferrous ion can be converted into ferric ion on the presence of $H_2O_2$, which complex with a selective indicator, Xylenol Orange (XO), to give the ultraviolet light/ visible light (UV/Vis) absorption peak centered at 560 nm[15,16]. To investigate the mechanical activation behavior at molecular level, free radicals (i.e. mechanoradicals) in the stretched bulk polymers can also be detected by in situ EPR spectroscopy which is a magnetic resonance technique. The *g* value of these EPR spectra was determined to be consistent with oxygen radicals and carbon radicals (2.003), indicating that the magnetic signal could be assigned to the dissociated diarylbibenzofuranone radicals (**Figure 2-6**)[17].

## 2.3. Mechanical strength of a covalent bond

### 2.3.1 Rupture force of single covalent bonds under loading

In the past decade, the development of nanoscale manipulation techniques allowing the precise application and measurement of the fracture force of single covalent bonds. The rupture force of single covalent bonds under loading can be measured with an atomic force microscope (AFM). Force-extension curves that were recorded during mechanical stretching and relaxation revealed a wealth of fingerprint-like features, such as conformational changes, supermolecular rearrangements or bond rupture[18-20]. In fact, there is a distribution of covalent bond-rupture forces when measured by AFM. Specially, the distribution interval of C-C bond rupture force is on the scale of nano force, which is around 2 nN to 6 nN[20].

In addition, the development of experimental techniques that enable the study of the effect of a mechanical force at the single-molecule or single-bond level has revolutionized the polymer mechanochemistry. In this regard, single molecule force spectroscopy (SMFS) based on atomic force microscopy (AFM), mostly conducted under ultrahigh vacuum and low temperatures, have demonstrated that researchers now have the capability to manipulate and apply mechanical forces onto individual atoms of polymer chains. SMFS is used to observe the irreversible extension of a gem-dibromocyclopropane (gDBC) functionalized polybutadiene under tension, a process akin to polymer necking at a single-molecule level (**Figure 2-8**). The electrocyclic ring opening of gDBC was monitored by SMFS, the force versus extension curves were fit to both the cusp and Bell-Evans models (BE fit above, red line, 100% gDBC, $\Delta x^{\ddagger}$ ) 1.08 Å, 34% extension)[21]. In fact, the magnitude of the externally applied fracture force determines the degree of mechanical disruption of the bond under loading[22].

### 2.3.2 Covalent bond strength calculated by density functional theory (DFT)

The rupture force of a single covalent bond in a polymer chain can be experimentally determined by atomic force microscopy (AFM). The theoretical approaches toward bond scission phenomena dealing with the macroscopic interfaces fracture were used to assist the interpretation of the experimental results of AFM. The rupture forces of covalent bonds as a functional of bond lifetime can be calculated with an Arrhenius kinetics model according to density functional theory. In the reported literatures, the model molecule $H_3CCH_2CH_3$ was chosen to calculate the bond energy ($D_e$) and fracture force ($F$) of C-C bond, which are 370.8 kJ/mol and 6.92 nN, respectively[23]. In a real, the number of carbon atoms between the crosslinking points of the polymer networks is 100−600, which is larger than the model molecule. The results of the DFT calculations are of reference significance for understanding the mechanisms of the single event (i.e. bond scission) in bulk polymeric materials.

### 2.3.3 Fracture site of polymer chains under loading

Much research has revealed that linear polymer chains in dilute solution undergo homolytic scission when exposed to ultrasound due to cavitation events. The rate of polymer chain scission depends on parameters including the frequency, intensity, and duration of ultrasound; the concentration, quality, temperature, vapor pressure, and gas solubility of the polymer solution; and the composition and molecular weight of the polymer chains[24-26]. Price and co-workers found that the rate of ultrasonic degradation is also directly proportional to polymer molecular weight for chains longer than a threshold value (typically 30 kDa). Experimentally, the polymer chain has been found to rupture near the midpoint of its backbone, where the solvodynamic forces are assumed to be the greatest. Encina and co-workers found that each oxygen-oxygen (O-O) bond is ruptured more than 5000 times faster than a C-C bond in their experimental system, they also found the rate of ultrasonic degradation of poly(vinylpyrrolidone) (PVP) is considerably 10 times faster in the oxygen-containing PVP than in the standard PVP[27]. This result was used to infer that ultrasonic degradation of a polymer occurs preferentially at weak bonds incorporated into the polymer chain.

Recently, Moore and co-workers found that ultrasound-induced site-specific scission of a polymer was accomplished by incorporating a single weak, azo linkage into the backbone of poly(ethylene glycol). These research works show that mechanically induced scission can be localized almost exclusively to a single weak site when this reactive unit is positioned near the center of the polymer backbones (**Figure 2-10**)[26]. However, if the topology of long polymer chain is considered, the distribution of strain energy on the polymer chain becomes more complex. Saitta and co-workers reported that polymer chain breaks under tension at the entrance to the knot, like a knotted rope (**Figure 2-11**)[28]. However, covalent bonds link monomer units into polymer chains, and crosslink polymer chains into polymer networks within a macroscopic material. In general, a real polymer network is heterogeneous and lack controlled structures, examples of network imperfection include dangling chains, loops, and chains of unequal lengths. Network imperfection affects mechanical properties of polymeric materials, such as strength, toughness, modulus, and fatigue-resistant. The dangling chains contribute to viscoelasticity, rubbing against the adjacent polymer chains or the solvent molecules, the loops and chains of unequal lengths cause sequential and distributed polymer chain scission due to the stress concentration in local environment[29]. Mechanical forces are distributed inhomogeneously amongst the individual polymer chain in a macroscopic polymer material[30]. For example, the mechanical force concentrated on the short chains (in red) due to the topological defects of the rigid first networks when the double networks undergo elongation (**Figure 2-12**). Therefore, the short chains would fracture prior to the long chains during the deformation. The mechanoradicals generated by the short polymer chains scission are chain-end radicals. These chain-end radicals can abstract hydrogen atoms from the adjacent polymer chains to stabilize themselves and to produce chain radicals on the H-abstracted polymer chains. The conversion of chain-end radicals in biomolecular reactions under mechanical stress was first reported by Sohma, who interprets this result in terms of the direct effect in mechanochemistry, which he considers as a dynamic process by which mechanical energy can cause chemical phenomena[9]. In summary, the site of polymer chain scission depends on the bond strength, chain entanglement, and topological defects within polymeric materials.

### 2.3.4 Fracture energy of a single polymer chain scission

Fracture of a polymeric material is inherently molecular, as it requires the scission of covalent bonds.

For example, the fracture of vulcanized rubber has been described by Lake and Thomas, they used the energy balance approach to estimate the fracture energy $T_c$ of the material (i.e. tearing energy)[31]. And they proposed that the fracture energy $T_c$ is equal to the number of bringing strand per cross-sectional area (σ) multiplied by the energy that is required to break one bridging strand ($W$), giving the equation 2-1.

$$T_c = \sigma W = \frac{1}{2} \nu R_0 n U \tag{2-1}$$

Here, $\nu$ is the number density of such elastically active network strand, $R_0$ is the average end-to-end length of an elastically active network strand in its undeformed state, $n$ is the average number of repeat units along the bridging strand, $U$ is the energy that is stored in each repeat unit when the bridging strand scission. The equation gives $\sigma = \frac{1}{2} \nu R_0$ as a mathematical estimate that the number of elastically active chains per cross-sectional area. Here, the factor of $\frac{1}{2}$ comes from the projection of the end-to-end vectors of bridging strands onto the normal of the crack plane[32]. Lake-Thomas also proposed that $W$ is proportional to the number of repeat units to give $W = nU$ (**Figure 2-13**). Note that the fracture energy in Lake-Thomas theory does not consider the energy dissipation in damage zones of real polymeric materials.

In order to break one covalent bond of strength $E_b$ when the bond is not undergoing any vibrations, an active energy must be supplied. If, however the covalent bond is under loading due to a constant force $f$ pulling on either end, the active energy required to break the covalent bond is diminished from $E_b$ to $\Delta U_{act}$. In terms of energy $\Delta U_{act}$, the Morse approximation to the interatomic potential gives the energy stored by a single covalent C-C bond at its maximum attractive force as the quarter of bond dissociation energy $E_b$ ($E_b$ = 350−370 kJ/mol). Here, the stored energy can also be called mechanical activation energy $\Delta U_{act}$ ($\Delta U_{act}$ = 88−93 kJ/mol)[33]. In fact, the quantitative adjustment to the molecular energy parameter shows that the stored elastic energy per bond of $\Delta U_{act}$ is about ~64 kJ/mol[32]. In this study, the $\Delta U_{act}$ = 88 kJ/mol is used to calculate the amount of mechanoradical in chapter 4.

## 2.4. Productive mechanochemistry in polymeric materials

In the past ten years, the field of polymer covalent mechanochemistry has witnessed great development. The early works in the field of polymer mechanochemistry were largely focused on studying the mechanical failure or degradation of polymeric materials. Once limited to the simple break of polymer chains, mechanical force can now be applied to generate a wide range of productive or useful chemistry within polymeric materials.

### 2.4.1 Biasing reaction pathways coupled with external mechanical force

Mechanical force has indeed been shown to activate covalent bonds in polymeric materials, but the usual result is polymer chain scission. Unlike light, heat, pressure or electrical potential, mechanical force as a new approach to energy input can also facilitate movement over the energy barrier of chemical reactions. Hickenboth and co-workers have shown that mechanically sensitive chemical groups can accelerate rearrangement reactions and bias reaction pathways to yield products not obtainable from purely heat or light-induced reactions[34]. Ultrasound as a method of force input can be applied to polymer to accelerate and alter the chemical reactions. Although there are practical limitations to controlling the outcome of chemical reactions using the mechanochemistry, the procedures will be generally helpful for discovering novel mechanophores, the chemical reactivities of which are triggered by mechanical force.

The mechanical force can thus clearly alter the shape of potential energy surface under mild conditions. Recent theoretical studies have shown that mechanical force loaded on cyclobutanes by stretching pendant polymer chains influences product selectivity through force-imparted nonstatistical dynamic effects on the stepwise ring-opening reaction. Liu and co-workers use computational modeling and simulations to illustrate that, besides altering energy barriers of chemical reaction, the mechanical force activates reactive intramolecular motions nonstatistically, setting up “flyby reaction trajectories” that advance directly to a product without isomerization excursions[35].

### 2.4.2 Mechanophores for stress sensing

Davis and co-workers first demonstrated that mechanical force-triggered covalent-bond activation can also be realized with mechanophore-linked elastomeric and glassy polymeric materials, by using a mechanophore (spiropyran) that changes color as it undergoes a reversible electrocyclic ring-opening reaction under mechanical force and thus allows us to directly and locally visualize the mechanochemical reaction[36]. The chameleon-like polymeric materials can change color on deformation, the transduction mechanism underpinning this mechanochemical effect could be used to make polymeric materials that respond in many other ways to mechanical force.

The incorporation of mechanochemically active functional groups (“mechanophores”) into polymeric materials has been reviewed in many reviews[37-41]. Chen and co-workers designed a luminescent mechanophore from the 1,2-dioxetane unit, which is incorporated in a rubber-like polymer network, the polymeric material can emit visible light on opening the four-membered ring[42,43]. The damaged zone around the crack tip can be directly seen where and when sacrificial bonds break as the tough elastomer is deformed by using the chemoluminescent cross-linker, bis(adamantyl)-1,2-dioxetane bisacrylate (a mechanophore, which is able to emit light when it breaks)[44]. The intensity mapping provides much more precise information to increase understanding of damage zones around the crack tip.

### 2.4.3 Mechanochemical catalysis and synthesis

Piermattei and co-workers demonstrated that activation of homogeneous catalysts with a mechanical force. The mechanochemical scission of a metal–ligand bond may be used to release the innate catalytic activity of either the ligand or the metal. Their findings bode well for the development of polymeric materials in which mechanochemical activation of latent catalysts is used for self-healing based on polymerization or crosslinking of reactive monomers[45].

Ultrasound as a fast, simple, and clean method, has been reported to synthesize macroscopic permanent hydrogels. Gelation by ultrasound can also be achieved in an initiator-free solutions. Properties of the gels can be adjusted by controlling the ultrasound dose[46]. Seminal work by Lenhardt et al. reported that gem-dichlorocyclopropanes (gDCCs) undergo mechanically assisted ring opening reactions when coupled to shear flows and that several hundreds of these reactions occur on the time scale of a single polymer chain scission[47]. Wu et al. used the single-molecule force spectroscopy to observe the irreversible extension of a gem-dibromocyclopropane (gDBC) functionalized polybutadiene under force, a process akin to polymer necking at a single-molecule level[48]. Recent work by Black Ramirez et al. shown that the same shear forces can be used to accelerate productive crosslinking reactions in mechanophores (i.e. gDBC) along polymer backbones, and it is demonstrated here that such mechanochemical reactions can be used to strengthen a polymer subjected to otherwise destructive shear forces[49].

### 2.4.4 Polymer mechanochemistry for dynamic self-strengthening materials

In mechanochemical processes, the energy required for the activation of chemical reactions is usually provided by external mechanical force, which is similar to the photochemistry, thermochemistry, or electrochemistry, where energy input is provided by light, heat, or electricity, respectively. Recent developments in covalent bond mechanochemistry have provided a mechanism by which those mechanical forces can be channeled into constructive, rather than destructive, responses, including strengthening in polymeric materials[50]. Verstraeten et al. showed that the hexaarylbiimidazole (HABI) mechanophore incorporated into a polymeric material can produce colored radicals, which can initiate secondary radical reactions yielding new polymer networks[51]. The special HABI mechanophore combines self-reporting of bond scission and reinforcement of polymeric materials.

Recent decades have witnessed a growing interest in the reinforcement, self-strengthening, or self-growing materials. Seminal work by Matsuda et al. reported a biological metabolism-inspired strategy to develop the self-growing double-network (DN) hydrogels. Unlike the traditional chemical hydrogels, the tough DN hydrogel can respond to repetitive mechanical force with an increase in their polymer amount and size and acquire further strength[52].

## References

1. Y. C. Simon, S. L. Craig. *Mechanochemistry in materials*. Ch. 1 (Royal Society of Chemistry, 2017).
2. Y. Mawani, J. F. Cawthray, S. Chang, K. Sachs-Barrable, D. W. Weekes, K. M. Wasan, and C. Orvig. In vitro studies of lanthanide complexes for the treatment of osteoporosis. *Dalton Trans.* **42**, 5999−6011 (2013).
3. Q. M. Wang, G. R. Gossweiler, S. L. Craig, and X. H. Zhao. Cephalopod-inspired design of electro-mechano-chemically responsive elastomers for on-demand fluorescent patterning. *Nat. Commun.* **5**, 4899 (2014).
4. L. M. Mäthger, L. E. J. Denton, N. J. Marshall, and R. T. Hanlon. Mechanisms and behavioural functions of structural coloration in cephalopods. *J. R. Soc. Interface* **6**, S149−S163 (2009).
5. R. Hanlon. Cephalopod dynamic camouflage. *Curr. Biol.* **17**, R400−R404 (2007).
6. H. Staudinger. Über isopren und kautschuk, 20. mitteil.: Über die kolloidnatur von kautschuk, guttapercha und balata. *Ber. Dtsch. Chem. Ges. B* **63**, 921−934 (1930).
7. H. Staudinger, W. Heuer. Über hochpolymere verbindungen, 93. mitteil.: Über das zerreißen

der faden-moleküle des polystyrols. *Ber. Dtsch. Chem. Ges. B* **67**, 1159−1164 (1934).

8. H. W. Melville, A. J. R. Murray. The ultrasonic degradation of polymers. *Trans. Faraday Soc.* **46**, 996−1009 (1950).
9. J. Sohma. Mechanochemistry of polymers. *Prog. Polym. Sci.***14**, 451−596 (1989).
10. D. S. Shtarev, A. V. Shtareva, A. I. Blokh, P. S. Goncharova, and K. S. Makarevich. On the question of the optimal concentration of benzoquinone when it is used as a radical scavenger. *Appl. Phys. A.* **123**, 602 (2017).
11. Y. F. Cheng, J. R. Liu, Q. S. Gu, Z. L. Yu, J. Wang, Z. L. Li, J. Q. Bian, H. T. Wen, X. J. Xiao, X. Hong, and X. Y. Liu. Catalytic enantioselective desymmetrizing functionalization of alkyl radicals via Cu(I)/CPA cooperative catalysis. *Nat. Cat.* **3**, 401−410 (2020).
12. S. Fujisawa, Y. Kadoma, and I. Yokoe. Radical-scavenging activity of butylated hydroxytoluene (BHT) and its metabolites. *Chem. Phys. Liquids* **130**, 189−195 (2004).
13. M. P. Dziobak, G. D. Mendenhall. 2,2-Di-(4-tert-octylphenyl)-1-picrylhydrazyl as an alkane-soluble standard for electron paramagnetic resonance studies. *J. Magn. Reson.* **50**, 274−280 (1982).
14. K. R. Fitch, A. P. Goodwin. Mechanochemical reaction cascade for sensitive detection of covalent bond breakage in hydrogels. *Chem. Mater.* **26**, 6771–6776 (2014).
15. H. T. Baytekin, B. Baytekin, and B. A. Grzybowski, Mechanoradicals created in ‘‘Polymeric Sponges’’ drive reactions in aqueous media. *Angew. Chem., Int. Ed.* **51**, 3596–3600 (2012).
16. T. Matsuda, R. Kawakami, R. Namba, T. Nakajima, and J. P. Gong, Mechanoresponsive self-growing hydrogels inspired by muscle training. *Science* **363**, 504–508 (2019).
17. K. Imato, T. Kanehara, S. Nojima, T. Ohishi, Y. Higaki, A. Takahara, and H. Otsuka. Repeatable mechanochemical activation of dynamic covalent bonds in thermoplastic elastomers. *Chem. Commun.* **52**, 10482–10485 (2016).
18. H. B. Li, M. Rief, F. Oesterhelt, and H. E. Gaub. Single-molecule force spectroscopy on xanthan by AFM. *Adv. Mater.* **10**, 316–319 (1998).
19. A. F. Oberhauser, P. E. Marszalek, H. P. Ericksson, and J. M. Fernandez. The molecular elasticity of the extracellular matrix protein tenascin. *Nature* **393**, 181–185 (1998).
20. M. Grandbois, M. K. Beyer, M. Rief, H. Clausen-Schaumann, and H. E. Gaub. How strong is a covalent bond? *Science* **283**, 1727–1730 (1999).
21. D. Wu, J. M. Lenhardt, A. L. Black, B. B. Akhremitchev, and S. L. Craig. Molecular stress relief through a force-induced irreversible extension in polymer contour length. *J. Am. Chem. Soc.* **132**, 15936–15938 (2010).
22. S. Garcia-Manyes, A. E. M. Beedle. Steering chemical reactions with force. *Nat. Rev. Chem.* **1**, 1–16 (2017).

23. M. K. Beyer. The mechanical strength of a covalent bond calculated by density functional theory. *J. Chem. Phys.* **112**, 7307–7312 (2000).
24. A. W. Basedow, K. H. Ebert. *Ultrasonic degradation of polymers in solution. Physical Chemistry* PP. 83–148 (Springer, 1977).
25. M. M. Caruso, D. A. Davis, Q. L. Shen, S. A. Odom, N. R. Sottos, S. R. White, and J. S. Moore. Mechanically-induced chemical changes in polymeric materials. *Chem. Rev.* **109**, 5755–5798 (2009).
26. K. L. Berkowski, S. L. Potisek, C. R. Hickenboth, and J. S. Moore. Ultrasound-induced site-specific cleavage of azo-functionalized poly(ethylene glycol). *Macromolecules* **38**, 8975–8978 (2005).
27. M. V. Encina, E. Lissi, M. Sarasúa, L. Gargallo, and D. Radic. Ultrasonic degradation of polyvinylpyrrolidone: effect of peroxide linkages. *J. Polym. Sci. Polym. Lett.* **18**, 757–760 (1980).
28. A. M. Saitta, P. D. Soper, E. Wasserman, and M. L. Klein. Influence of a knot on the strength of a polymer strand. *Nature* **399**, 46–48 (1999).
29. C. H. Yang, T. H. Yin, and Z. G. Suo. Polyacrylamide hydrogels. I. Network imperfection. *J. Mech. Phys. Solids* **131**, 43–55 (2009).
30. Z. S. Kean, S. L. Craig. Mechanochemical remodeling of synthetic polymers. *Polymer* **53**, 1035–1048 (2012).
31. G. J. Lake, and A. G. Thomas. The strength of highly elastic materials. *Proc. R. Soc. London, Ser. A: Math. Phys. Sci.* **300**, 108−119 (1967).
32. S. Wang, S. Panyukov, M. Rubinstein, and S. L. Craig. Quantitative adjustment to the molecular energy parameter in the Lake–Thomas theory of polymer fracture energy. *Macromolecules* **52**, 2772−2777 (2019).
33. W. Kauzmann, and H. Eyring. The viscous flow of large molecules. *J. Am. Chem. Soc.* **62**, 3113−3125 (1940).
34. C. R. Hickenboth, J. S. Moore, S. R. White, N. R. Sottos, J. Baudry, and S. R. Wilson. Biasing reaction pathways with mechanical force. *Nature* **446**, 423−427 (2007).
35. Y. Liu, S. Holm, J. Meisner, Y. Jia, Q. Wu, T. J. Woods, T. J. Martinez, and J. S. Moore. Flyby reaction trajectories: chemical dynamics under extrinsic force. *Science* **373**, 208−212 (2021).
36. D. A. Davis, A. Hamilton, J. L. Yang, L. D. Cremar, D. V. Gough, S. L. Potisek, M. T. Ong, P. V. Braun, T. J. Martínez, S. R. White, J. S. Moore, and N. R. Sottos. Force-induced activation of covalent bonds in mechanoresponsive polymeric materials. *Nature* **459**, 68−72 (2009).
37. A. L. Black, J. M. Lenhardt, and S. L. Craig. From molecular mechanochemistry to stress-responsive materials. *J. Mater. Chem.* **21**, 1655−1663 (2011).
38. R. Klajn. Spiropyran-based dynamic materials. *Chem. Soc. Rev.* **43**, 148−184 (2014).
39. Y. Yuan, and Y. L. Chen. Visualized bond scission in mechanically activated polymers. *Chinese Journal of Polymer Science*. **35**, 1315−1327 (2017).
40. N. Deneke, M. L. Rencheck, and C. S. Davis. An engineer's introduction to mechanophores.

*Soft Matter* **16**, 6230−6252 (2020).

41. Y. J. Chen, G. Mellot, D. V. Luijk, C. Creton, and R. P. Sijbesma. Mechanochemical tools for polymer materials. *Chem. Soc. Rev.* **50**, 4100−4140 (2021).
42. Y. L. Chen, A. J. H. Spiering, S. Karthikeyan, G. W. M. Peters, E. W. Meijer, and R. P. Sijbesma. Mechanically induced chemiluminescence from polymers incorporating a 1,2-dioxetane unit in the main chain. *Nat. Chem.* **4**, 559−562 (2012).
43. Y. L. Chen, and R. P. Sijbesma. Dioxetanes as mechanoluminescent probes in thermoplastic elastomers. *Macromolecules* **47**, 3797−3805 (2014).
44. E. Ducrot, Y. L. Chen, M. Bulters, R. P. Sijbesma, and C. Creton. Toughening elastomers with sacrificial bonds and watching them break. *Science* **344**, 186−189 (2014).
45. A. Piermattei, S. Karthikeyan, and R. P. Sijbesma. Activating catalysts with mechanical force. *Nat. Chem*. **1**, 133−137 (2009).
46. B. Rokita, J. M. Rosiak, and P. Ulanski. Ultrasound-induced cross-linking and formation of macroscopic covalent hydrogels in aqueous polymer and monomer solutions. *Macromolecules* **42**, 3269−3274 (2009).
47. J. M. Lenhardt, A. L. Black, and S. L. Craig. gem-Dichlorocyclopropanes as abundant and efficient mechanophores in polybutadiene copolymers under mechanical stress. *J. Am. Chem. Soc.* **131**, 10818−10819 (2009).
48. D. Wu, J. M. Lenhardt, A. L. Black, B. B. Akhremitchev, and S. L. Craig. Molecular stress relief through a force-induced irreversible extension in polymer contour length. *J. Am. Chem. Soc.* **132**, 15936−15938 (2010).
49. A. L. Black Ramirez, Z. S. Kean, J. A. Orlicki, M. Champhekar, S. M. Elsakr, W. E. Krause, and S. L. Craig. Mechanochemical strengthening of a synthetic polymer in response to typically destructive shear forces. *Nat. Chem.* **5**, 757−761 (2013).
50. J. P. Wang, I. Piskun, and S. L. Craig. Mechanochemical strengthening of a multi-mechanophore benzocyclobutene polymer. *ACS Macro Lett.* **4**, 834−837 (2015).
51. F. Verstraeten, R. Göstl, and R. P. Sijbesma. Stress-induced colouration and crosslinking of polymeric materials by mechanochemical formation of triphenylimidazolyl radicals. *Chem. Commun.* **52**, 8608−8611 (2016).
52. T. Matsuda, R. Kawakami, R. Namba, T. Nakajima, and J. P. Gong. Mechanoresponsive self-growing hydrogels inspired by muscle training. *Science* **363**, 504−508 (2019).

## Figures

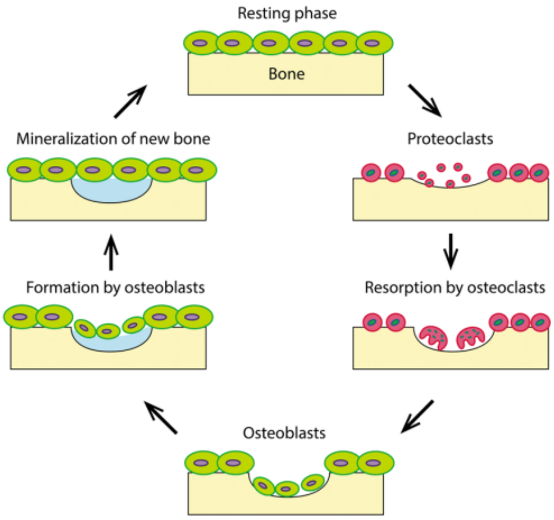

**Figure 2-1.** A schematic illustration of the bone dynamic self-growing cycle (Reprinted with the permission from ref. 1; Copyright (2017) Royal Society of Chemistry).

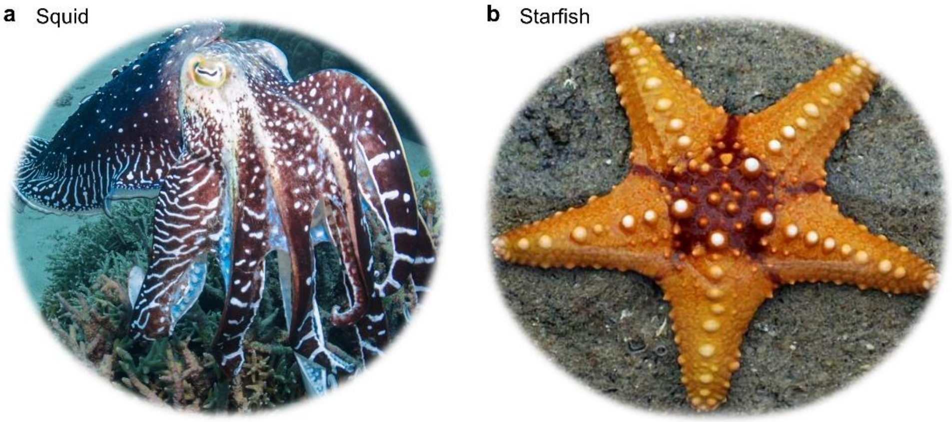

**Figure 2-2.** Images of the natural self-grown dazzling patterns on skins of the squid and starfish (Reprinted with the permission from www.pexels.com).

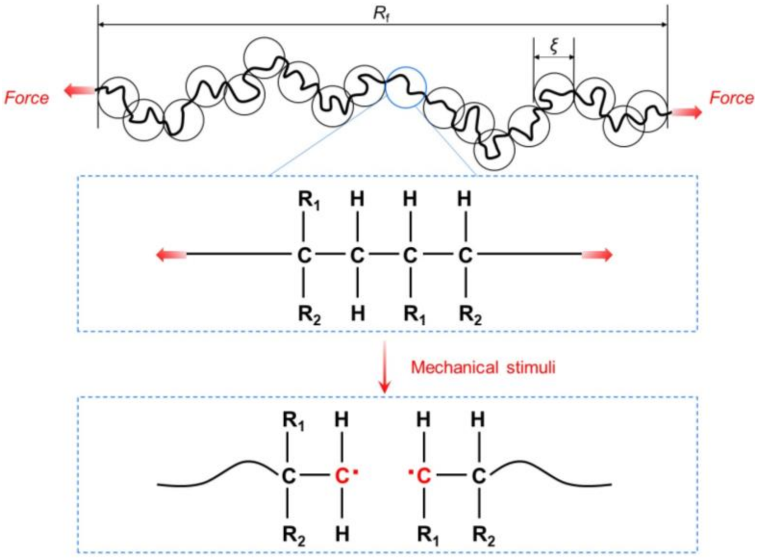

**Figure 2-3.** Polymer chains under a limit large tension, the contour length $R_f$, the blob size $\xi$, mechanoradical generation by bond homolytic scission of polymer backbone. (Redraw with the permission from ref. 9; Copyright (1989) Royal Society of Chemistry).

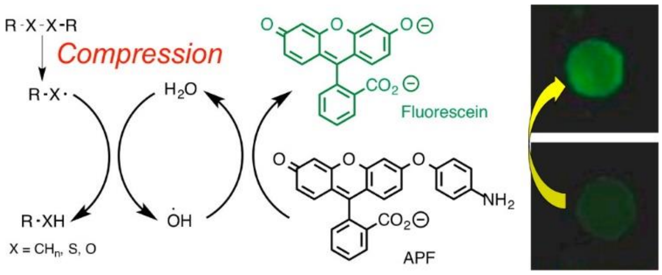

**Figure 2-4.** Proposed mechanism of fluorescence activation by mechanical compression, hydroxyl radical can then react with the APF, producing the green-emissive fluorescein. (Reprinted with the permission from ref. 14; Copyright (2014) American Chemical Society).

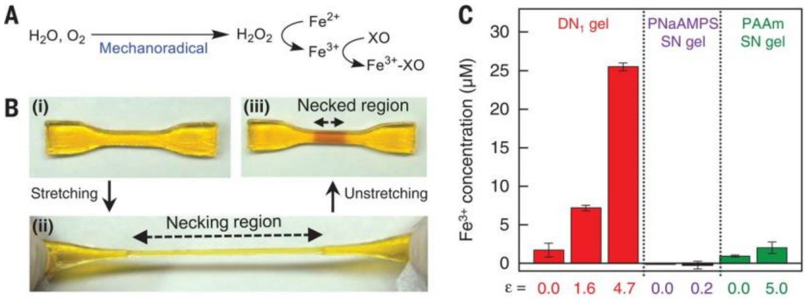

**Figure 2-5. A.** Fenton color reaction induced by mechanoradicals in hydrogel bulk, **B**. Photograph of a double-network hydrogels fed with $Fe^{2+}$, XO, and $H_2SO_4$ (i) before, (ii) during, (iii) 30 min after mechanical stretching, **C**. Estimated $Fe^{3+}$ concentrations by ultraviolet/visible (UV/Vis) absorption spectroscopy in the unstretched and stretched hydrogels. (Reprinted with the permission from ref. 16; Copyright (2019) Science).

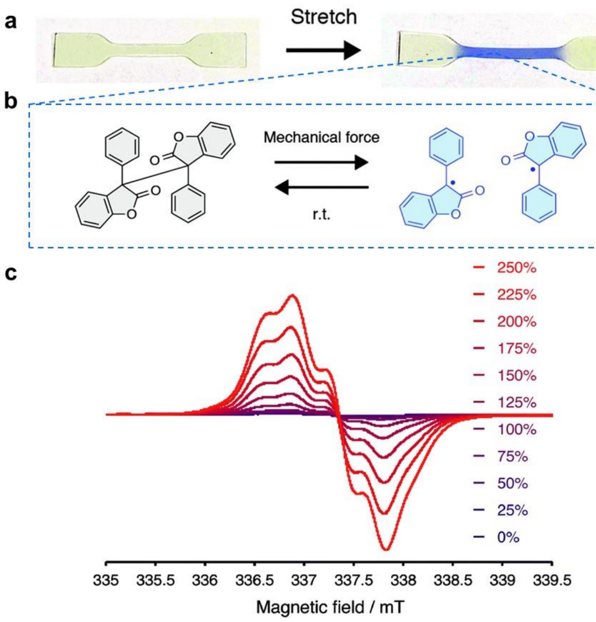

**Figure 2-6. a.** Photographs of manual stretching of dumbbell-shaped diarylbibenzofuranone (DABBF, a mechanophore) containing thermoplastic elastomer, **b.** Mechanically triggered conversion of equilibrium between colourless DABBF and blue-coloured radicals, **c.** EPR spectra of elastomer as a function of increasing strain. The intensity was normalized by the sample volume. (Reprinted with the permission from ref 17; Copyright (2016) Royal Society of Chemistry).

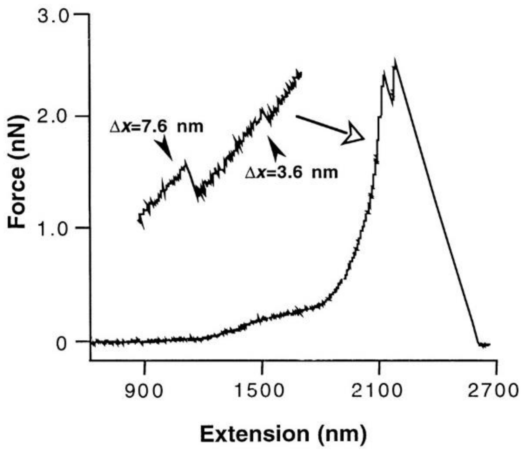

**Figure 2-7.** Force versus extension curve of amylose showing multiple ruptures in the high-force regime. The enlarged curve section of the high-force regime shows multiple irreversible ruptures leading to elongations (Δx) of the amylose chain. (Reprinted with the permission from ref 20; Copyright (1999) Science).

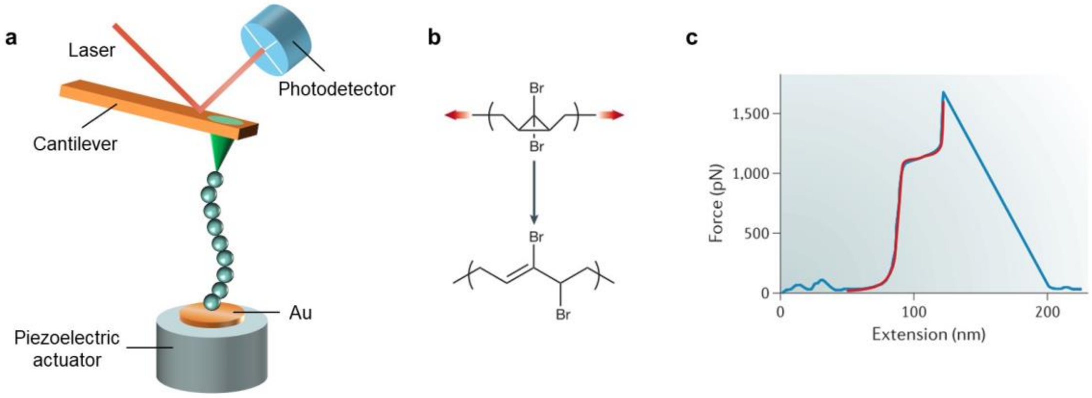

**Figure 2-8**. **a**. Schematic of the single molecule force spectroscopy (SMFS) experiment, **b**. Structure of gem-dibromocyclopropane (gDBC) which ring opens to form a 2,3-dibromoalkene product, **c**. Representative plateaus in the force–separation curves of gDBC-containing polymers. (Redraw with the permission from ref 21; Copyright (2010) American Chemical Society).

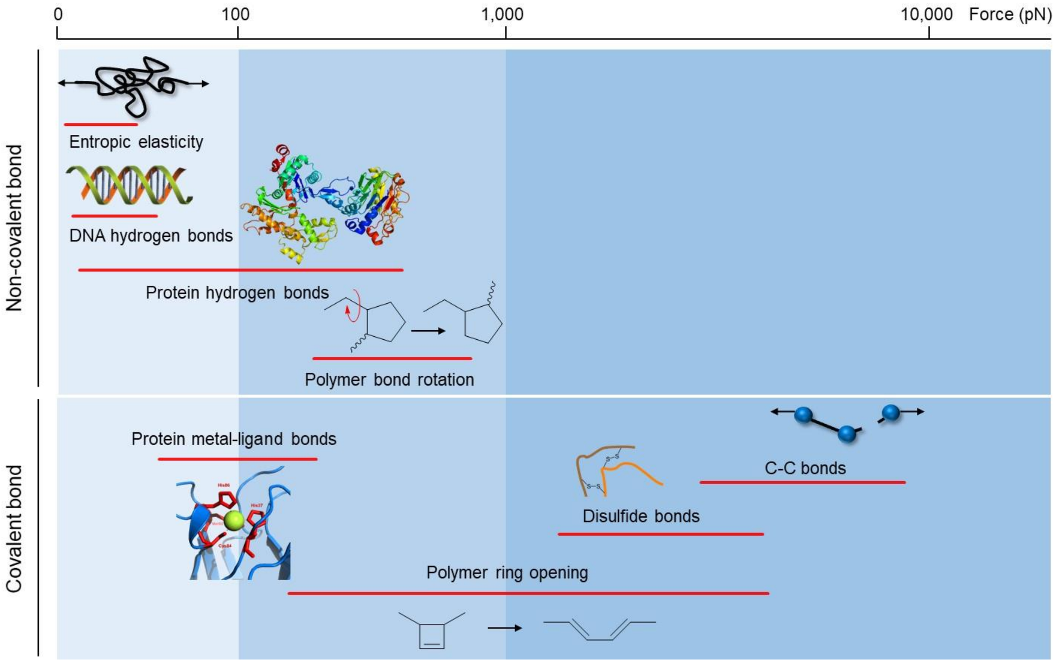

**Figure 2-9**. The magnitude of the externally applied fracture force determines the degree of mechanical disruption of the bond under mechanical loading. (Redraw with the permission from ref 22; Copyright (2017) Springer Nature).

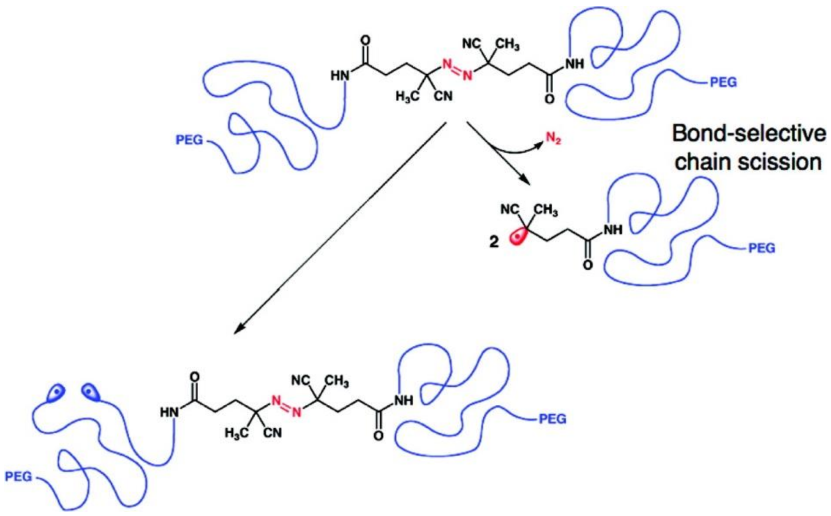

**Figure 2-10**. Selective bond break for the ultrasound-induced azo-centered PEG chains. For a 30 kDa polymer, selectivity is one bond in 1000 C−C/C−O bonds. Bond-selective chain scission is the predominant pathway. (Reprinted with the permission from ref. 26; Copyright (2005) American Chemical Society).

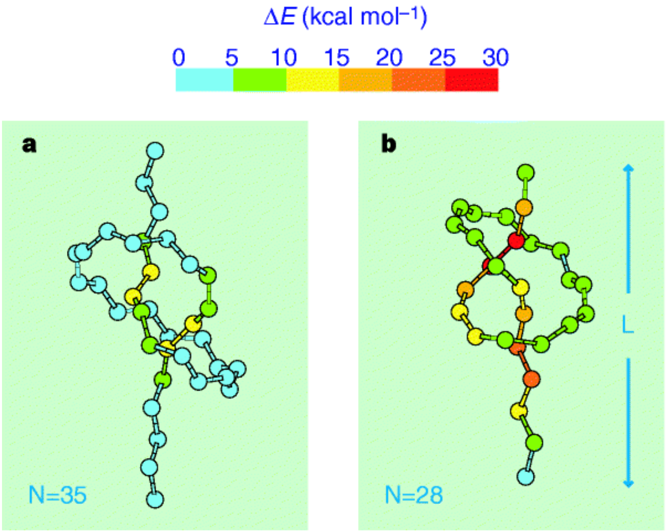

**Figure 2-11**. Strain energy distribution in a knotted polymer strand, shown are distributions in chains of 35 (a) and 28 (b) carbon atoms taken from constrained classical MD simulations. When the knot is sufficiently tightened, the strain energy localizes most on the bonds immediately outside its entrance points. (Reprinted with the permission from ref. 28; Copyright (1999) Springer Nature).

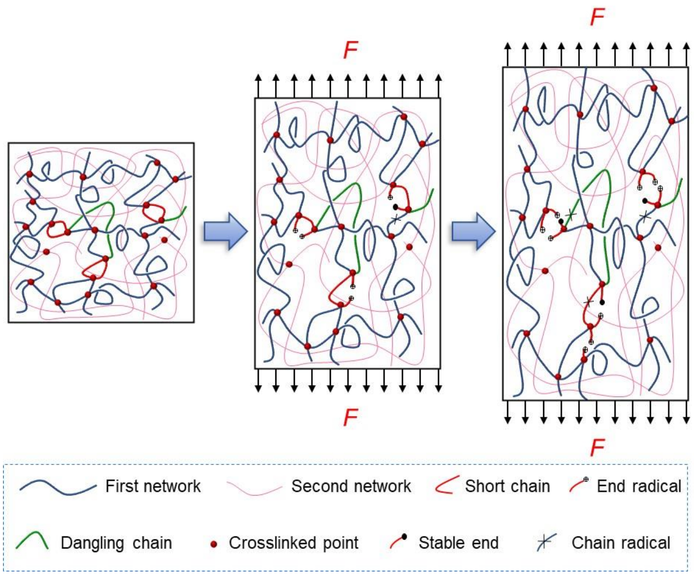

**Figure 2-12**. Schematic for polymer network deformation, polymer chain scission, free radical production, and conversion in double-network polymeric materials under mechanical loading.

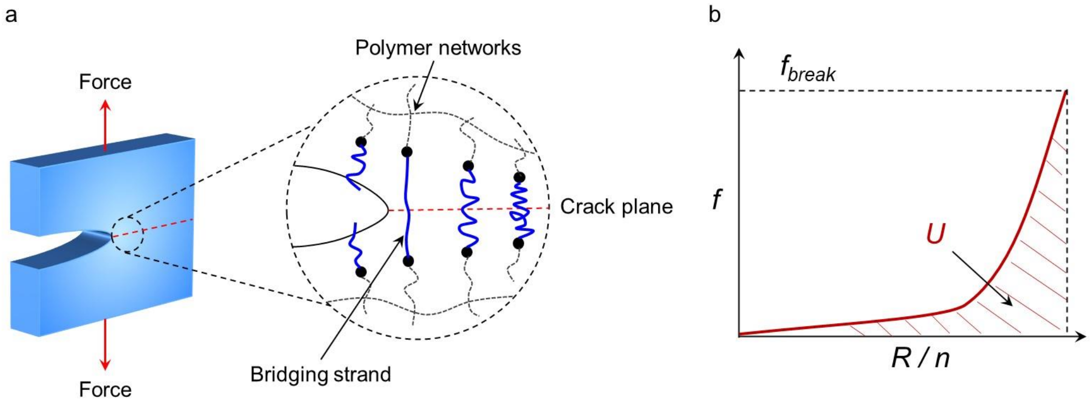

**Figure 2-13**. **a**. Schematic illustration of crack propagation at the crack tip. **b**. The energy needed to extend a polymer chain (light red shaded region *U*) under the force vs end-to-end distance curve (red curve) up to the force at which the chain breaks. (Redraw with the permission from ref. 32; Copyright (2019) American Chemical Society).

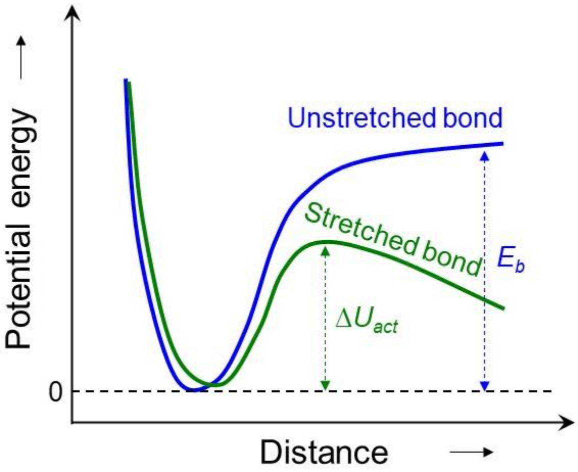

**Figure 2-14**. Functional curves of Morse potential under stretched and unstretched states. (Redraw with the permission from ref. 33; Copyright (1940) American Chemical Society).

# Chapter 3: Synthesis and Preparation of Materials

## 3.1. Introduction

In this work described in **Chapters 4-6**, the single-network (SN) and double-network (DN) hydrogels were synthesized by the reported procedure[1-3]. Herein, the DN hydrogels were composed of an anionic poly(2-Acrylamido-2-methylpropanesulfonic acid sodium salt) (PNaAMPS) first network and nonionic polyacrylamide (PAAm) second network. The schematic illustration of fabrication of DN hydrogels were shown in **Figure 3-1**, the chemical structure of first and second networks were shown in **Figure 3-10 a**. Previous research works mainly focused on the mechanical properties and toughness mechanism of DN hydrogel bulk, the poly(2-Acrylamido-2-methylpropanesulfonic acid) (PAMPS) as the first network was often used[1,3]. In this work, a sodium salt NaAMPS was used for the first network synthesis, the double-network structure was formed not only in the hydrogel bulk but also near the hydrogel surface without formation of a soft surface layer from the second network using the surface-bulk transition technology[3]. The two main reasons for our choice are: (1) In this work, force-triggered radical polymerization occurred inside and/or on DN hydrogels as shown in **Chapters 4-6**. Neutral environment of DN hydrogels ensured more normal situation and stable chemical reactions than the acidic environment; (2) The double-network structure on DN hydrogel surfaces ensured that the bond scission and radical polymerization can be triggered on DN hydrogels, when the regioselective mechanical indentation was used to damage DN hydrogel surfaces.

In this chapter, synthetic procedure and fundamental physical and chemical properties of hydrogels are presented, including mechanical properties, surface morphology, surface modulus, and surface chemical signal.

## 3.2. Experiments

### 3.2.1 Materials

Deionized water ($H_2O$) used was purified by a lab water purification system (Merck KGaA, Darmstadt, Germany). Acrylamide (AAm) was purchased from Junsei Chemical, 2-Acrylamido-2-methylpropanesulfonic acid sodium salt (NaAMPS) (49.7 wt % aqueous solution) was provided by Toa Gosei. *N,N'*-Methylenebisacrylamide (MBA), 2-oxoglutaric acid (α-keto) were purchased from

Fujifilm Wako Pure Chemical Corporation. Deuterium oxide ($D_2O$) was purchased from Fujifilm Wako Pure Chemical Corporation. All the chemicals were used as received. Silicon-coated polyethylene glycol terephthalate (Si-PET) films were purchased from Mitsui Chemicals Tohcello. Inc. Soda-lime glass plates and silicon rubbers were purchased from As One Corporation. Three-dimensional (3D) printing ink was purchased from Keyence Corporation.

### 3.2.2 Preparation of PNaAMPS SN hydrogels

Firstly, a homogeneous and transparent aqueous solution of NaAMPS ($C_1$) monomer, MBA ($x_1$ mol%) as a crosslinker, and α-keto ($x_2$ mol%) as a photo-initiator was prepared after 5 minutes of sonication. The crosslinker and initiator concentration (molar ratio, mol%) are denoted as respected to the monomer. The crosslinker concentration $x_1$ was varied from 2.0 to 6.0 mol%, and photo-initiator concentration $x_2$ was 1.0 mol%. Every precursor aqueous solution containing NaAMPS, MBA and α-keto was moved to an argon glove box (MBRAUN, oxygen concentration less than 100 ppm) to remove oxygen. The precursor solution was injected into a reaction cell that comprising two soda-lime glass plates (size: 10 cm×10 cm, thickness: 3 mm) separated by a silicone rubber (0.5 mm-3 mm) as a spacer in argon glove box. Then the reaction cell was then irradiated with ultraviolet (UV) light (365 nm, 4 W $cm^{-2}$) at least for 8 h in an argon glove box to synthesize the hydrogel. The as-prepared PNaAMPS SN hydrogels were applied for the next step (**section 3.2.4**) to synthesize DN hydrogels. When the SN hydrogel was used as the control sample, the as-prepared PNaAMPS SN hydrogel was immersed in deionized water to equilibrium swelling prior to the next experiments. Each PNaAMPS SN hydrogel was coded as ($C_1$-$x_1$-$x_2$) PNaAMPS SN hydrogel, where $C_1$, $x_1$ and $x_2$ were the monomer concentration, the crosslinker concentration molar ratio and initiator concentration molar ratio (mol%) respect to $C_1$ ($x_1$: 2-8 mol%, $x_2$: 1 mol%), respectively.

### 3.2.3 Preparation of PAAm SN hydrogels

A homogeneous and transparent aqueous solution of AAm ($C_2$) monomer, MBA ($x_1$ mol%) as a crosslinker, and α-keto ($x_2$ mol%) as a photo-initiator was prepared after at least 5 minutes of sonication. The crosslinker and initiator concentration (molar ratio, mol%) are denoted as respected to the monomer. The crosslinker concentration $x_1$ was 0.01 mol%, and photo-initiator concentration $x_2$ was 0.01 mol%. Every precursor aqueous solution containing AAm, MBA and α-keto was moved to an argon glove box (MBRAUN, oxygen concentration less than 100 ppm) to remove oxygen. The precursor solution was injected into a reaction cell that comprising two soda-lime glass plates (size: 10 cm×10 cm, thickness: 3 mm) separated by a silicone rubber (0.5-3 mm) as a spacer in argon glove box. Then the reaction cell was then irradiated with ultraviolet (UV) light (365 nm, 4 W $cm^{-2}$) at least for 8 h in an argon glove box to synthesize the SN hydrogel. The as-prepared PAAm SN hydrogel was used as the control sample, and it was immersed in deionized water to equilibrium swelling prior to the next experiments. Each PAAm SN hydrogel was coded as ($C_2$-$x_1$-$x_2$) PAAm SN hydrogel, where $C_2$, $x_1$ and $x_2$ were the monomer concentration, the crosslinker concentration molar ratio and initiator concentration molar ratio (mol%) respect to $C_2$ ($x_1$: 0.01 mol%, $x_2$: 0.01 mol%), respectively.

### 3.2.4 Preparation of PNaAMPS/PAAm DN hydrogels with controlled surfaces

The synthesized PNaAMPS SN hydrogel (**section 3.2.2**) was immersed in precursor aqueous solution of the second network (monomer concentration $C_2$ was 2.0 M, 0.01 mol% MBA, and 0.01 mol% 2-oxoglutaric acid, molar ratio with respect to AAm monomer) for one day at 4 °C. Then, the swollen PNaAMPS SN hydrogel with the second network precursor solution was sandwiched between two flat glass plates as a reaction cell. The surfaces of glass plates in contact with the hydrogel were covered with a hydrophobic silicone-coated PET (Si-PET) film. The reaction cell was compressed by a pressure of ~0.8 kPa for 12 h using the gravity of several glass plates in an argon glove box. Through this method, contact of PNaAMPS SN hydrogel with the hydrophobic surface of the cell wall was ensured, and air bubbles between the hydrogel and Si-PET film were removed as possible. The reaction cell was then irradiated with UV light at least for 8 h in an argon glove box to synthesize the PAAm network in the presence of the first pre-stretched rigid PNaAMPS network (called a surface-bulk transition technique)[3]. The synthesized DN hydrogels were immersed in deionized water for more than one day to equilibrium swelling and to remove the unreacted species. Each DN hydrogel was coded as ($C_1$-$x_1$-$x_2$/$C_2$-$x_1$-$x_2$) DN hydrogel, where $C_1$ and $C_2$ are monomer concentration for the first and second network, respectively. $x_1$ and $x_2$ were the crosslinker concentration molar ratio and initiator concentration molar ratio (mol%) respect to the corresponding monomer, respectively. The DN hydrogel was also coded as DN gel-Si-PET-0.8kPa and DN gel-glass, when the glass plates covered by hydrophobic Si-PET film and glass plates were used for the second network synthesize, respectively. The schematic illustration of fabrication of

DN hydrogels with the controlled surfaces was shown in **Figure 3-1**.

### 3.2.5 Tensile and fracture measurements

The mechanical tensile tests were performed using a commercial tensile-compressive tester (Tensilon RTC-1310A, Orientec Co., Ltd.) at a displacement velocity of 100 mm $\mathrm{min}^{-1}$ (a strain rate of 0.14 $\mathrm{s}^{-1}$) in air (25 $^{\circ}$C). Hydrogels were cut into dumbbell-shaped samples with the standard JIS-K6251-7 size (12 mm length × 2 mm width × 1.5 mm thickness). The tensile test (or uniaxial stretching) was applied to characterize mechanical properties of hydrogels, fracture stress, fracture strain, and work of extension, the stress-strain curves of hydrogels were shown in **Figure 3-2.** The cyclic tensile tests of SN and DN hydrogels were also carried out using the same tester, the cyclic stress-strain curves were shown in **Figure 3-3**.

The fracture measurements were performed to characterize hydrogel toughness (fracture energy or tearing energy) in air by using the same commercial tester mentioned above. In the fracture measurements, the samples of 1.5 mm ($t_0$) in thickness were cut into trousers-like shape with cut length $c$ based on the standard JIS-K6252 1/2 sizes (50 mm length ($L$) × 7.5 mm width ($h_0$), the cut length (or initial notch length) $c$ was 20 mm) using a cutting machine (Dumb Bell Co., Ltd.). One leg of the trouser-shaped DN hydrogel was fixed and the other leg was pulled away at a velocity of 100 mm $\mathrm{min}^{-1}$. The fracture energy $\Gamma$ was calculated using the following equation[4].

$$\Gamma = \frac{2\lambda F}{t_0} - W(\lambda) \cdot h_0 \approx \frac{2F}{t_0} \tag{3-1}$$

where $F$ and $W$ is the tearing force and the arm's stored elastic energy per unit volume during crack propagation. When the elastic deformation of the two hydrogel arms is neglected, the fracture energy is approximated as $\Gamma \approx 2F/t_0$. The stress-strain curves of hydrogels were shown in **Figure 3-4.** The mechanical properties of different hydrogels were summarized in **Table 3-1.**

### 3.2.6 Three-dimensional (3D) laser microscope observation

Different SN and DN hydrogel surfaces, the glass and silicone-coated PET (Si-PET) film were observed by a 3D laser microscope in air. Free water on hydrogel surfaces was wiped out by clean tissues prior to observation, the magnification was ×10, the resolution was 0.5 μm, the scale bar was 200 μm for each observation. The laser scanning time for each sample surface was around 50 s, surface roughness parameters $R_a$ (i.e. the arithmetic average of the roughness profile) was calculated by selecting a square area on material surfaces, as shown in **Figure 3-5** and **Figure 3-6**.

### 3.2.7 Characterization of surface modulus of hydrogel surfaces

A sphere metal indenter (radius of 0.25 mm) was used to probe the local surface elastic modulus of different hydrogels at a constant rate of 1 mm $\text{min}^{-1}$ underwater. The water environment was applied to prevent the evaporation of water from hydrogel surface. The sphere metal indenter was a rigid, frictionless, impermeable indenter. Firstly, as-prepared different hydrogels were cut into fixed square shape (size: 2 cm×2 cm, thickness: ~3.8 mm) then immersed in pure water to equilibrium state prior to the indentation measurement. The square samples were fixed on a rigid plate in a homemade box, the rigid plate was a frictionless, impermeable metal substrate. Surface elastic modulus $E$ (Pa), a parameter that characterizes the mechanical property (stiffness) of a material, was calculated by the following mathematical equation[5,6].

$$E = \frac{3}{4} l^{-\frac{3}{2}} f R^{-\frac{1}{2}} (1 - v_p^2) \tag{3-2}$$

where $l$ is depth, $f$ is indentation force, $R$ is the radius of sphere indenter, $v_\mathrm{p}$ is Poisson's ratio and set to be 0.5.

Therefore, the surface elastic modulus was calculated from the initial slope (indentation depth: 0–0.01 mm) of the $f$-$l^{3/2}$ indentation curves (**Figure 3-7**). The calculated surface modulus was the average value of three replicates, which was summarized in **Figure 3-8**. We prepared the DN hydrogel surfaces using a surface-bulk transition technique, and tough hydrogel surfaces with the first rigid networks (densely crosslinked polymer network strands) were confirmed by the surface elastic modulus measurements.

### 3.2.8 Attenuated total reflectance Fourier-transform infrared (ATR FT-IR) spectroscopy measurements

The hydrogel surface layer chemical signal was probed by an ATR FT-IR spectroscopy (FT-IR 6600 spectrometer, JASCO, Japan). With its shallow detection range (1–2 μm) and high resolution in wavenumber (~2 $\text{cm}^{-1}$), the ATR FT-IR measurements focused on the chemical group at the interface between the hydrogel and its immediate surroundings[7]. We confirmed that the first brittle network PNaAMPS is on the DN hydrogel surfaces based on the stretching vibration peak (~1042 $\text{cm}^{-1}$) of sulfonic group from PNaAMPS chains. The as-prepared DN and SN hydrogels were immersed in pure water for at least one week to equilibrium swelling, the swollen hydrogels were immersed in $D_2O$ for two days to replace $H_2O$ prior to the measurements. The wavenumber region was 1800 – 800 $cm^{-1}$, number of scans was 64, resolution was 2 $cm^{-1}$. The infrared spectra and linear polymer structure with functional groups were shown in **Figure 3-10**, infrared absorption peak at 1042 $cm^{-1}$ indicated that there is first network on the controlled DN hydrogel surfaces prepared by our surface-bulk transition technology.

## 3.3. Results and discussion

### 3.3.1 Mechanical properties of hydrogels

The mechanical properties of hydrogels describe their ability to withstand applied loads and displacements. The traditional single-network (SN) hydrogels have poor mechanical properties due to the amorphous and swollen polymer networks, which are lack of effective energy dissipation mechanism. In contrast, the DN hydrogels have excellent mechanical strength, mainly in high tensile strain, tensile stress, and high toughness (**Figure 3-2**). The yielding stress was increased with the crosslinker concentration of the first brittle network $x_1$, because yielding stress was controlled by the areal density of the first brittle network[8]. When increase $x_1$, the areal density of the first network was increased. Tough DN hydrogels derive their high toughness from large stress-strain hysteresis (**Figure 3-3**). The area between a loading and an unloading curve was the energy dissipated during the mechanical load and unload. In DN hydrogels, the hysteresis was due to the rupture of the short-chain network (i.e. the first brittle network)[9]. It was often assumed that a PAAm SN hydrogel has nearly elasticity, because the hysteresis of the cyclic mechanical loading curve was very small and narrow, almost negligible[10]. Fracture toughness, that is, the resistance to crack initiation and propagation under mechanical stress, is a critical material property. The fracture toughness of soft materials is typically characterized as the fracture energy $\Gamma$, in units of J $m^{-2}$, which represents the mechanical energy required to increase the length of a crack into forming a unit new area of the fractured surface. Here, the tearing test was used to characterize the fracture toughness of DN hydrogels. As shown in **Figure 3-4**, the two arms of a pre-cracked specimen were oppositely displaced to impose the tearing load. The toughness value was summarized in **Table 3-1**, the $DN_4$ hydrogel has the toughest performance when compared with the other DN hydrogels. The toughest $DN_4$ gels with different surfaces were typically used in **chapter 4 and chapter 5** for the study of micropatterning on DN hydrogel surfaces.

### 3.3.2 Surface modulus of different hydrogels

Modulus, is a ratio of the stress divided by the strain on a material, which is a measure of the stiffness of a material. Here, surface modulus of hydrogels was measured by mechanical indentation under water based on the Hertzian contact theory **Figure 3-7** shows the schematic illustration for indentation and curves of $f$-$l^{3/2}$, the slopes of curves are proportional to the surface elastic moduli of different hydrogels. Because the thickness of hydrogel was larger than the indentation depth, the effect from rigid substrate can be negligible. The surface modulus of hydrogels was calculated and summarized in **Figure 3-8**, the surface modulus were 661.2±88.9 kPa, 6.6±0.1 kPa, 14.1±0.3 kPa, and 683.2±52.9 kPa for 1st gel, 2nd gel, DN gel-glass and DN gel-Si-PET-0.8kPa, respectively. The highly crosslinked and pre-stretched first network was confirmed to determine large surface elastic modulus of DN hydrogels, these data suggested that the double-network structure is formed not only in the hydrogel bulk but also near the hydrogel surface without formation of a soft surface layer from the second network for DN gel-Si-PET-0.8kPa.

### 3.3.3 Surface chemical signal of different hydrogels

First, the characteristic IR absorption signal of pure water ($H_2O$) and deuterium oxide ($D_2O$) was detected by ATR-FTIR. **Figure 3-9 b** shows the obvious absorption peaks of $H_2O$ and mixture of $H_2O$ and $D_2O$. As is well known, the adsorption of $H_2O$ is represented by strong IR absorbances of $\delta$ (H-O-H) bending at 1635 $\text{cm}^{-1}$. When $D_2O$ was used instead of $H_2O$, the results showed the peak of the isotopologue H-D-O bending band centred at 1450 $\text{cm}^{-1}$, and the clear shoulder formed around 1205 $\text{cm}^{-1}$ can be attributed to D-O-D bending[11]. Second, the immersed hydrogel surfaces were detected by ATR-FTIR (**Figure 3-10 b**), the peak at ~1200 $\text{cm}^{-1}$ for different hydrogel surfaces may be attributed to bending of D-O-D. Because $D_2O$ was used instead of $H_2O$ for immersing hydrogels, and the immersion solution (mixture of $D_2O$ and $H_2O$, very low content of $H_2O$). Some hydrogen atoms of group N-H may be replaced by deuterium atom of $D_2O$, when hydrogels were immersed in $D_2O$. DN hydrogels with its second network prepared on the Si-PET film covered glass mould (coded DN gel-Si-PET-0.8kPa) show the obvious PNaAMPS signal at ~1042 $\text{cm}^{-1}$, while DN hydrogels with its second network prepared on glass mould (coded DN gel-glass) do not. These results indicate that the DN hydrogel structure is formed even at the top-most surface in the former

DN hydrogels while the surface of the latter DN hydrogels is covered by PAAm layer.

## 3.4. Summary

This chapter focuses on the mechanical properties, surface modulus, and surface chemical signal of hydrogels. A DN hydrogel consists of two interpenetrating networks with contrasting structure and mechanical properties, the first network, highly crosslinked and pre-stretched, acts as a rigid brittle skeleton and sacrificial bonds to toughen the whole hydrogel. We propose that the highly crosslinked and pre-stretched first network determines the surface modulus of DN hydrogels, the double-network structure was formed not only in the hydrogel bulk but also near the hydrogel surface without formation of a soft surface layer from the second network for DN gel-Si-PET-0.8kPa. Finally, we used the toughest DN gel-Si-PET-0.8kPa (1-4-1/2-0.01-0.01) with no soft PAAm hydrogel layer for the further study in chapter 4, 5 and 6.

## References

1. J. P. Gong, Y. Katsuyama, T. Kurokawa, and Y. Osada. Double-network hydrogels with extremely high mechanical strength. *Adv. Mater.* **15**, 1155−1158 (2003).
2. S. Ahmed, T. Nakajima, T. Kurokawa, M. A. Haque, and J. P. Gong. Brittle-ductile transition of double-network hydrogels: Mechanical balance of two networks as the key factor. *Polymer* **55**, 914−923 (2014).
3. M. Frauenlob, D. R. King, H. L. Guo, S. Ishihara, M. Tsuda, T. Kurokawa, H. Haga, S. Tanaka, and J. P. Gong. Modulation and characterization of the double network hydrogel surface-bulk transition. *Macromolecules* **52**, 6704−6713 (2019).
4. S. P. O. Danielsen, H. K. Beech, S. Wang, B. M. El-Zaatari, X. D. Wang, L. Sapir, T. Ouchi, Z. Wang, P. N. Johnson, Y. X. Hu, D. J. Lundberg, G. Stoychev, S. L. Craig, J. A. Johnson, J. A. Kalow, B. D. Olsen, and M. Rubinstein. Molecular characterization of polymer networks. *Chem. Rev.* **121**, 5042−5092 (2021).
5. C. T. McKee, J. A. Last, P. Russell, and C. J. Murphy. Indentation versus tensile measurements of Young's modulus for soft biological tissues. *Tissue Eng Part B Rev.* **17**, 155−164 (2011).
6. K. I. Hoshino, T. Nakajima, T. Matsuda, T. Sakai, and J. P. Gong. Network elasticity of a model hydrogel as a function of swelling ratio: from shrinking to extreme swelling states. *Soft Matter* **14**, 9693−9701 (2018).
7. Y. Gombert, R. Simič, F. Roncoroni, M. Dübner, T. Geue, and N. D. Spencer. Structuring hydrogel surfaces for tribology. *Adv. Mater. Interfaces* **6**, 1901320 (2019).
8. T. Matsuda, T. Nakajima, Y. Fukuda, W. Hong, T. Sakai, T. Kurokawa, U. Chung, and J. P. Gong. Yielding criteria of double network hydrogels. *Macromolecules* **49**, 1865−1872 (2016).
9. R. E. Webber, C. Creton, H. R. Brown, and J. P. Gong. Large strain hysteresis and Mullins effect of tough double-network hydrogels. *Macromolecules* **40**, 2919−2927 (2007).
10. E. Zhang, R. B. Bai, X. P. Morelle, and Z. G. Suo. Fatigue fracture of nearly elastic hydrogels. *Soft Matter* **14**, 3563−3571 (2018).
11. H. Belhadj, A. Hakki, P. K. J. Robertson, and D. W. Bahnemann. In situ ATR-FTIR study of $H_2O$ and $D_2O$ adsorption on $TiO_2$ under UV irradiation. *Phys. Chem. Chem. Phys.* **17**, 22940−22946 (2015).

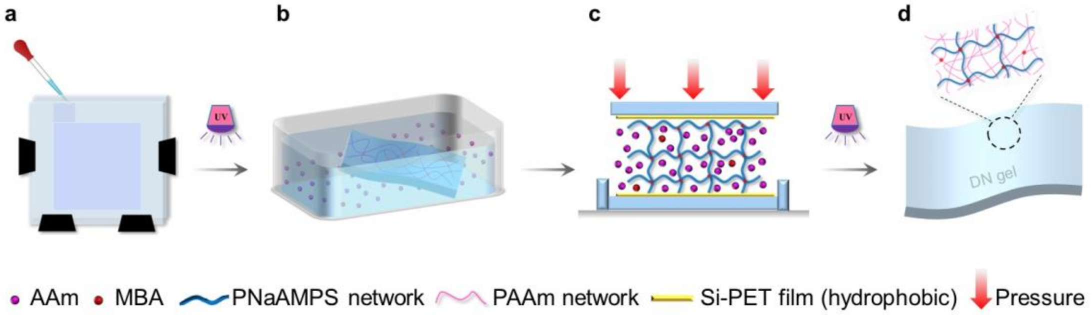

**Figure 3-1**. Schematic illustration of fabrication of tough double-network (DN) hydrogels with the double-network structure to the top-most surface layer (i.e. controlled surfaces, coded DN gel-Si-PET-0.8 kPa). **a**. The first network hydrogel was polymerized in a glass mould under UV light. **b**. The prepared first network hydrogel was immersed in the AAm monomer aqueous solution. **c**. A hydrophobic silicone-coated PET (Si-PET) film was covered on the glass mould surface by pressure (~0.8 kPa) during the second network synthesis to completely remove surface solution (residual AAm monomer aqueous solution), which also prevented the formation of the electric double layer at PNaAMPS-glass interface. Through this method, contact of PNaAMPS hydrogel with the hydrophobic surface of the Si-PET film was ensured.

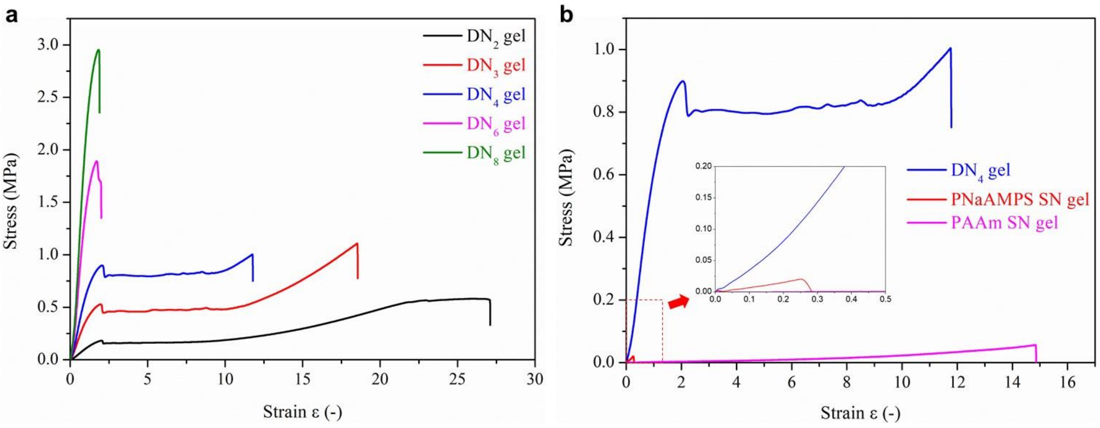

**Figure 3-2.** **a**. Tensile stress-strain curves of different DN hydrogels. Here, the DN$_2$ hydrogel is DN gel coded with 1-2-1/2-0.01-0.01. **b**. Tensile stress-strain curves of DN$_4$ gel and different SN gels. The inset figure shows the enlarged small strain region. Here, the PNaAMPS SN gel is the first network gel coded with 1-4-1, PAAm SN gel is second network gel coded with 2-0.01-0.01.

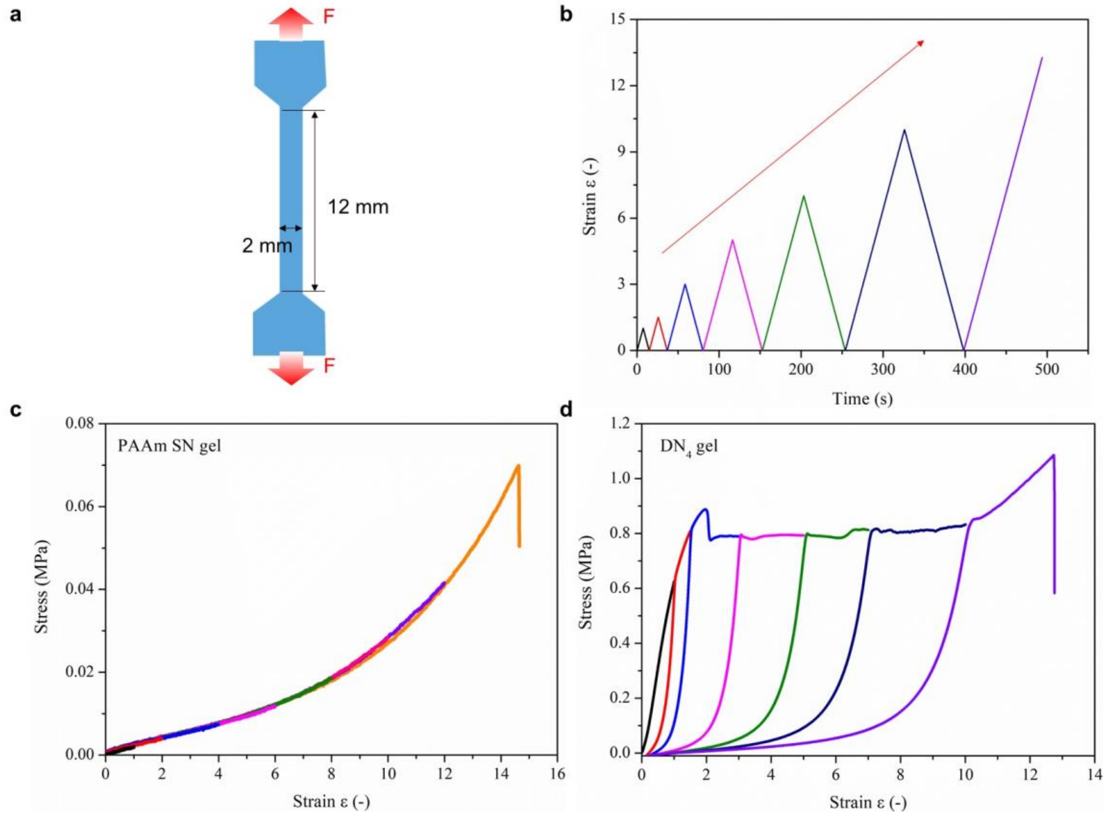

**Figure 3-3. a**. Schematic illustration for tensile tests of hydrogels (initial size of hydrogel: 12 mm length, 2 mm width, 1.5-3.0 mm thickness). **b**. Applied tensile strain changes over time for the cyclic tensile test. **c**. Stress-strain curves of cyclic tensile test of PAAm SN gel, the PAAm SN gel is second network gel coded with 2-0.01-0.01. **d**. Stress-strain curves of cyclic tensile test of DN$_4$ gel, the DN$_4$ gel is DN gel coded with 1-4-1/2-0.01-0.01.

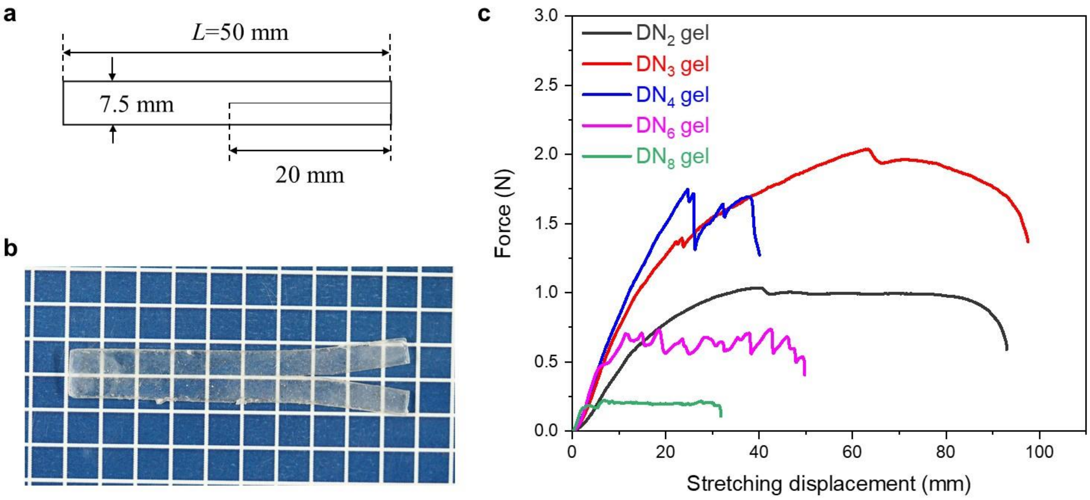

**Figure 3-4. a**. Schematic illustration for the gel size in the fracture test. **b**. Photograph of the cut gel sample with an initial notch. **c**. Force-displacement curves of different DN hydrogels in the fracture test.

**Table 3-1**. Mechanical properties of different SN and DN hydrogels (PNaAMPS SN gel, (1-4-1), PAAm SN gel (2-0.01-0.01), $DN_x$ gel (1-x-1/2-0.01-0.01)). Error ranges represent standard deviation from three replicates.

| Gel name | Fracture strain (-) | Fracture stress (MPa) | Young's modulus (MPa) | Work of extension ($J/m^3$) | Toughness ($kJ/m^2$) |
|---|---|---|---|---|---|
| $DN_2$ gel | 27.02±0.95 | 0.58±0.02 | 0.10±0.01 | 8.38±0.84 | 1.03±0.04 |
| $DN_3$ gel | 17.57±0.88 | 0.99±0.10 | 0.36±0.01 | 9.66±0.90 | 2.87±0.21 |
| $DN_4$ gel | 10.66±1.70 | 0.96±0.06 | 0.58±0.02 | 8.23±1.56 | 2.91±0.25 |
| $DN_6$ gel | 2.08±0.28 | 1.90±0.01 | 1.28±0.01 | 2.52±0.43 | 1.72±0.80 |
| $DN_8$ gel | 1.74±0.22 | 2.91±0.07 | 1.68±0.05 | 2.87±0.63 | 0.51±0.04 |
| PAAm SN gel | 14.17±0.75 | 0.06±0.01 | 0.07±0.01 | 0.003±0.001 | - |
| PNaAMPS SN gel | 0.27±0.04 | 0.02±0.01 | 0.002±0 | 0.26±0.04 | - |

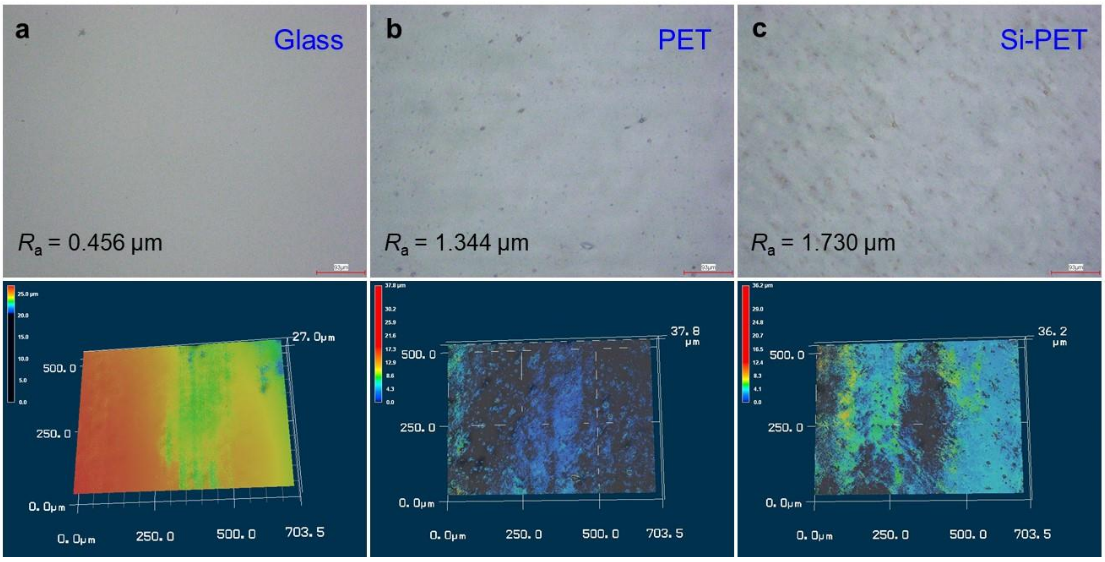

**Figure 3-5.** Surface topography (physical roughness) of different cover molds observed by 3D laser microscope in air. Here, $R_a$ was calculated as the roughness average of mold surfaces measured microscopic peaks and valleys. **a**. Glass plate surface. **b**. PET film surface. **c**. Silicone-coated PET film surface. Scale bars, 200 µm.

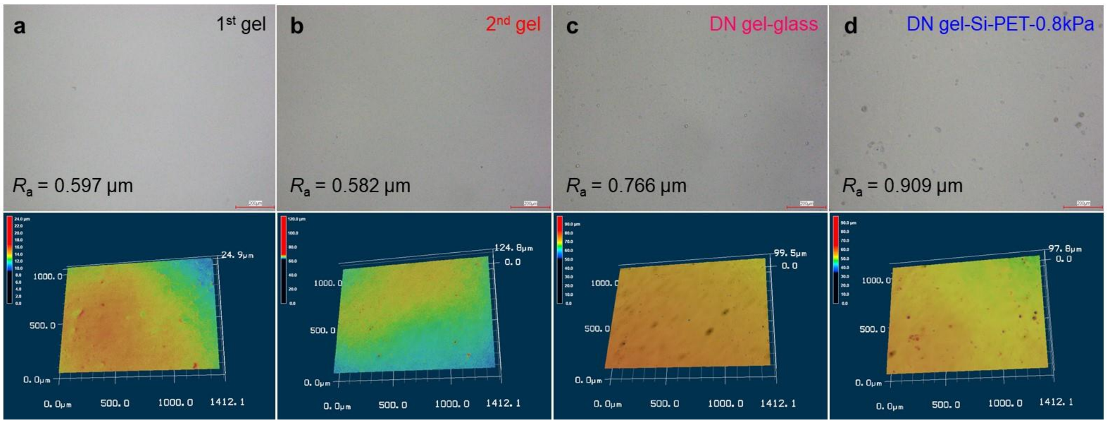

**Figure 3-6.** Surface topography (physical roughness) of different hydrogels observed by 3D laser microscope in air. Here, $R_a$ was calculated as the roughness average of gel surfaces measured microscopic peaks and valleys. **a**. 1st gel (PNaAMPS gel, coded with 1-4-1). **b**. 2nd gel (PAAm gel, coded with 2-0.01-0.01). **c**. DN gel-glass (DN gel (coded with 1-4-1/2-0.01-0.01) prepared between glasses). **d**. DN gel-Si-PET-0.8kPa (DN gel (coded with 1-4-1/2-0.01-0.01), the second network of DN gel was prepared between silicon-coated PET film under the pressure of ~0.8 kPa). Scale bars, 200 µm.

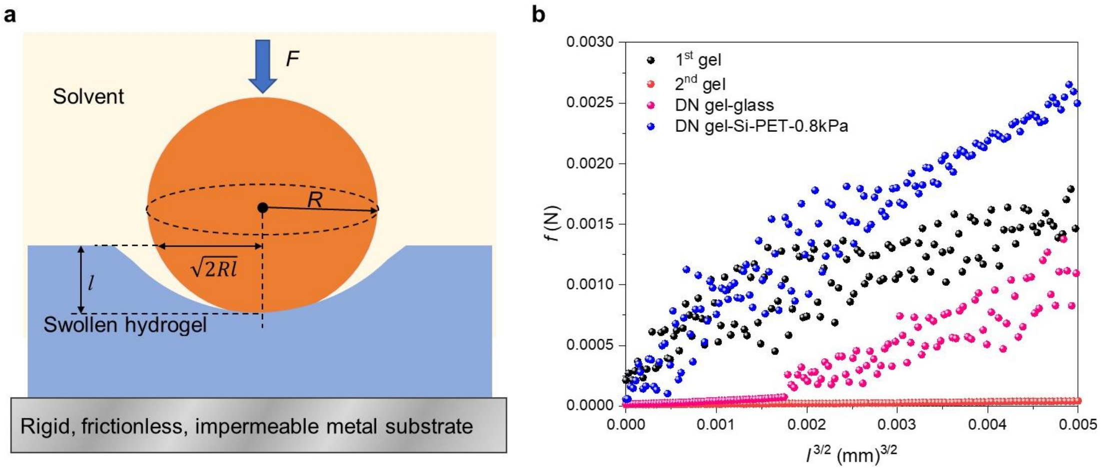

**Figure 3-7.** **a**. Schematic illustration for hydrogel surface indentation measurements under water using a sphere metal indenter. Hydrogel thickness was 3.5–5 mm, which was far larger than the indentation depth (~0.029 mm) in the experiments. **b**. Indentation curves of $f$-$l^{3/2}$ for different indentation measurements, the slopes of curves are proportional to the surface elastic moduli of different hydrogels. DN hydrogels with its second network prepared on Si-PET film covered glass mould show the almost same modulus as the single first network, while DN hydrogels with its second network prepared on glass mould show a lower modulus than the single first network. These results again indicate that the double-network structure is formed even at the top-most surface in the former DN hydrogels while the surface layer of the latter DN hydrogel is covered by the soft second network.

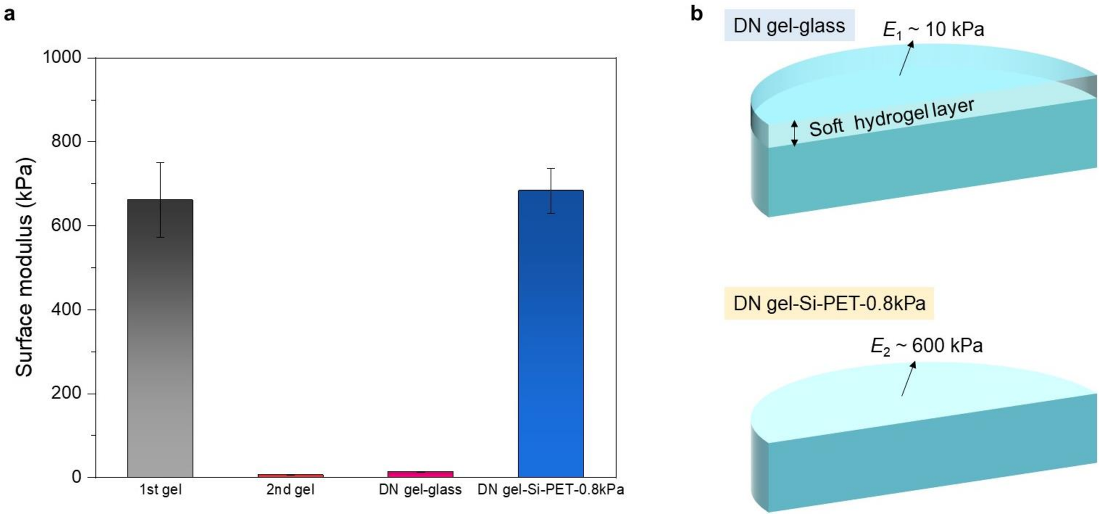

**Figure 3-8. a**. Surface modulus of different hydrogels. Error ranges represent standard deviation from three replicates. Some error bars are hidden by the histogram. **b**. Schematic illustration for DN gel-glass surface with soft hydrogel layer, and DN gel-Si-PET-0.8kPa with higher modulus.

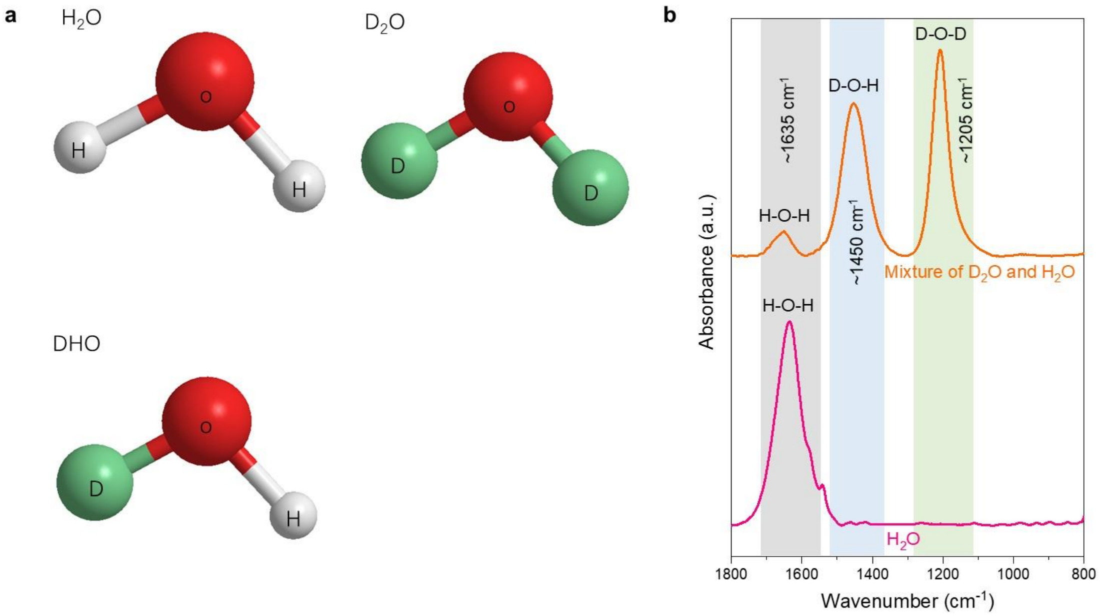

**Figure 3-9. a**. Three-dimensional molecular structures of $H_2O$, $D_2O$, and DHO. **b**. ATR-FTIR spectra of pure $H_2O$ and $D_2O$-$H_2O$ mixtures.

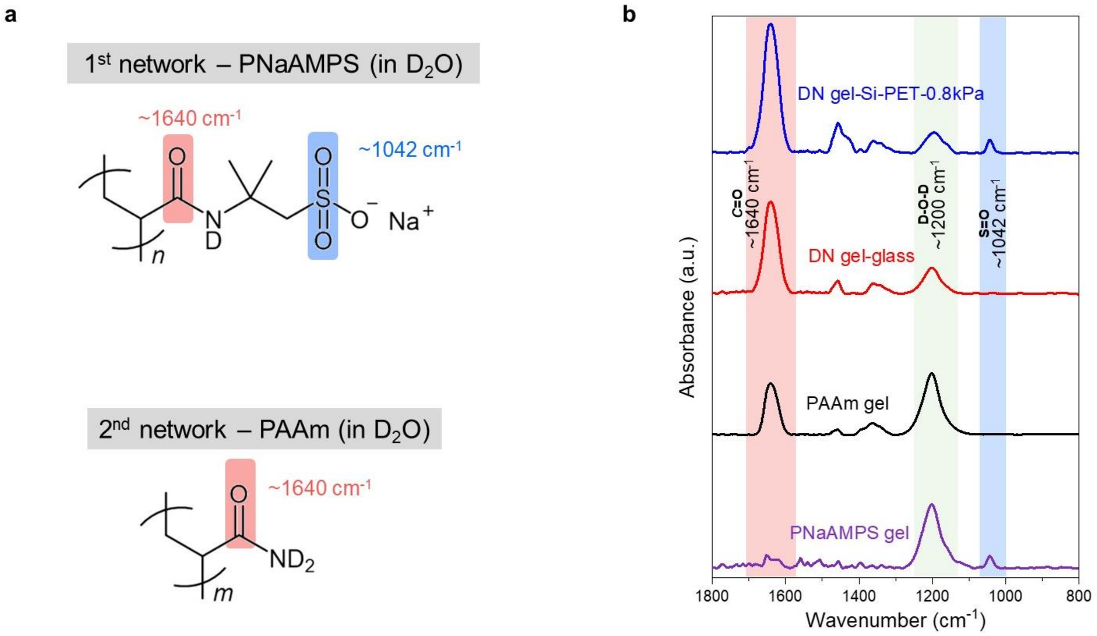

**Figure 3-10. a**. Polymer network structures with functional groups. **b**. DN hydrogels with its second network prepared on the Si-PET film covered glass mould (coded DN gel-Si-PET-0.8kPa) show the obvious PNaAMPS signal at ~1042 cm$^{-1}$, while DN hydrogels with its second network prepared on glass mould (coded DN gel-glass) do not. These results indicate that the DN hydrogel structure is formed even at the top-most surface in the former DN hydrogels while the surface of the latter DN hydrogels is covered by PAAm hydrogel.

# Chapter 4: Mechanical Properties, Regioselective Damage and Reswelling of DN Hydrogel Surfaces

## 4.1. Introduction

The double-network (DN) structure is a novel and generic strategy for toughening soft materials. DN structure comprises two interpenetrating polymeric networks with contrasting structures and mechanical properties[1]. The first network, highly crosslinked and pre-stretched, acts as a rigid but brittle skeleton at the molecular scale, which determines the elastic modulus of bulk DN hydrogels. The second network, sparsely crosslinked and relatively concentrated, is soft and stretchable. Owing to such contrasting structures, lots of the brittle first network strands can break during large deformation without causing catastrophic failure of bulk hydrogel, because the second network carries load once the strands in the first network break, which redistributes stress to other first network strands around the broken strands[2-4]. The resistance to crack initiation and propagation has been recognized as a critical material property. The toughening mechanisms of DN hydrogel are based on the energy dissipation from polymer strand scission of the first brittle network (i.e. sacrificial bonds)[3]. The energy dissipation zone around the crack tip is very large, the length scale of the dissipation zone is around ~1 mm for DN and hybrid tough hydrogels, the energy dissipation in this zone is quantified by the fracture energy, $\Gamma$, which represents the mechanical energy dissipated during crack advance per unit area[5]. The fracture energy of DN hydrogels obtained by tearing test can be as high as ~2000 J/m$^2$. However, the single-network (SN) hydrogel is so weak and easily brittle. Upon cyclic mechanical stretching, SN hydrogel shows nearly elasticity with negligible strain hysteresis, while DN hydrogel shows Mullin’s effect with large strain hysteresis[6]. Most pioneering studies have focused on the bulk mechanical properties of DN hydrogels, mechanical properties of the DN hydrogel surface have attracted rarely attention. Herein, DN hydrogel prepared by the surface-bulk transition technology[7] has a tough surface with modulus of ~600 kPa. In contrast, PAAm SN hydrogel has a soft surface with modulus of ~10 kPa. The first brittle network on the top-most surface layer of DN hydrogel determines the elastic modulus of whole hydrogel surface. In this study, we need to understand not only the bulk mechanical properties but also the mechanical properties, mechanical damage, and reswelling of DN hydrogel surfaces.

In this chapter, we study the mechanical properties, and fast reswelling of the process zones on DN hydrogel surfaces. We compared the mechanical properties of DN hydrogel surface with that of SN hydrogel surface. Computer simulation for the mechanical indentation on hydrogel surfaces was carried out using the commercial COMSOL Multiphysics software. The fast reswelling of the process zones on DN hydrogel surfaces was observed by a three-dimensional (3D) laser microscope. The qualitative and quantitative experiment results show the big differences between DN hydrogel surface and SN hydrogel surface.

## 4.2. Experiments

### 4.2.1 Materials

Deionized water ($H_2O$) used was purified by a lab water purification system (Merck KGaA, Darmstadt, Germany). Acrylamide (AAm) was purchased from Junsei Chemical, 2-Acrylamido-2-methylpropanesulfonic acid sodium salt (NaAMPS) (49.7 wt % aqueous solution) was provided by Toa Gosei. *N,N′*-Methylenebisacrylamide (MBA), and 2-oxoglutaric acid (α-keto) were purchased from Fujifilm Wako Pure Chemical Corporation. Inc. Soda-lime glass plates and silicon rubbers were purchased from As One Corporation.

### 4.2.2 Cylindrical indentation measurements

The single/cyclic mechanical indentation measurements were carried out using a Shimadzu Autograph AG-X 10N tensile machine in air at 25 °C. To characterize the mechanical properties of SN hydrogel and tough DN hydrogel surfaces without feeding monomers and crosslinker, a cylindrical steel indenter with smooth cutting edge (diameter of ~568 μm) was fixed on load cell by screw, the hydrogels were cut into disc shape (diameter of ~15 mm) then glued to a rigid glass plate from Matsunami company of Japan (S2112) prior to the mechanical indentation test. The single/cyclic indentation velocity was 1 mm $min^{-1}$. The deformed or damaged zones on hydrogel surfaces were immediately observed by a laser microscope after the mechanical indentation. The maximum force and hysteresis energy were obtained by the highest point of indentation curves and area beneath the force-displacement curves, respectively.

### 4.2.3 Simulation of hydrogel surface under mechanical deformation

Herein, the mechanical parameters of each hydrogel surface structural model were constructed in the finite element simulation using the commercially available COMSOL Multiphysics 5.6, Solid Mechanics (SM) module). The simulation unit cell of hydrogel was 20 mm in width and 5 mm in height, the simulation unit cell of steal indenter was 0.64 mm in width and 6 mm in height, the parameter of chamfer around the indenter edge was 0.04 mm (i.e. the distance to vertex), so the indenter diameter is around 0.57 mm, smaller than 0.64 mm. The material parameters (e.g. surface elastic modulus) of hydrogels were obtained from the mechanical indentation test. The density of PAAm hydrogel was set to 1.13 g cm$^{-3}$, density of DN hydrogel was set to 1.15 g cm$^{-3}$. In order to obtain a convergent value, Poisson's ratio was set to 0.45 for PAAm and DN hydrogel. It should be emphasized that the linear elastic solid model was considered for PAAm hydrogel. The elastoplastic solid model was considered for DN hydrogel owing to the yielding behaviour when experienced tensile stress.

### 4.2.4 Observation of different hydrogel surfaces and steel indenters by a three-dimensional (3D) laser microscope

Different hydrogel surfaces were observed in air by a 3D laser microscope (VK-9710, Keyence Co., Ltd.). Free water on hydrogel surfaces was wiped out by the clean tissues prior to the observation. The magnification was ×10, and the resolution was 0.5 μm for each observation. Surface roughness value $R_a$ was calculated by selecting a small square area (500 μm length × 500 μm width) on hydrogel surfaces. Side and top surfaces of the cylindrical steel indenters were also observed by the laser microscope, as shown in **Figure 4-1**. The process zones and reswollen zones on hydrogel surfaces were also observed by the laser microscope, the profile and size of microstructures were measured by a software VK Analyzer, as shown in **Figure 4-3**.

### 4.2.5 Ultrafast reswelling of the process zone on DN hydrogel surfaces

Firstly, the process zones on DN hydrogel surfaces were created by regioselective indentation under deionized water (cylindrical steel indenter diameter was ~568 μm, displacement was ~1000 μm). The small process zone (thickness of ~1000 μm and diameter of ~600 μm), the two-dimensional area was around ~0.1 mm$^2$. The time-lapse microscope observation show that the morphology of process zones changed over the immersion time, height of reswollen microstructure changed over the immersion time, the fast reswelling was finished within 1 min. The height $H$ of a DN hydrogel surface for different total immersion times $t$ were characterized as follows. First, an indented DN hydrogel surface was observed by the microscope in air ($t$ = 0 s, **Figure 4-13 a (i)**). The hydrogel was then immersed in water for 10 s, picked up from water and wiped by clean tissues, then observed by the microscope in air ($t$ = 10 s, **Figure 4-13 a (ii)**). Afterwards, the hydrogel was immersed in water for 20 s followed by the microscope observation in the same manner (total immersion time $t$ = 10 + 20 = 30 s). Such protocol was repeated several times for this DN hydrogel surface, resulting in $H$ as a function of $t$ up to 300 s. Error bar represents standard deviation for three replicates. Scale bar, 200 μm.

## 4.3. Results and discussion

### 4.3.1 Mechanical behaviors of different hydrogel surfaces

As swollen polymer networks in water, single-network (SN) hydrogels are usually brittle. Here, the surface of the prepared hydrogel was locally pressed using a cylindrical steel indenter with a diameter d = 568 μm and displacement $L_{\max}$ = 1000 μm without feeding any monomers in air. PAAm hydrogel exhibited nearly linear force-displacement curves upon cyclic mechanical indentation. The near-perfect elasticity results from the large amount of water molecules between the polymer chains. Because water has low viscosity and lubricates the PAAm polymer chains[8]. Three replicates were carried out for the mechanical indentation on PAAm hydrogel surfaces, the fitting function for the average force-displacement curve shows that the slope is $3.71\times10^{-3}$, PAAm hydrogel surface is highly hydrated and soft. Unlike the nearly elastic SN hydrogel, the DN gel-glass and DN gel-Si-PET-0.8kPa were tough and show nonlinear deformation at displacement above 0.2 mm. DN gel-Si-PET-0.8kPa shows bigger force response when the displacement was 1.0 mm. There is a soft PAAm layer of several micrometers thick on DN gel-glass surface, which acts as a soft and elastic barrier to make the hydrogel surface softer. The rigid skeleton (i.e. first network) on DN gel-Si-PET-0.8kPa surface determines the modulus of hydrogel surface, which also toughens the DN hydrogel surface.

### 4.3.2 Computer simulation of the mechanical indentation on hydrogel surfaces

Herein, the mechanical deformation and stress distribution around the indentation tip of hydrogel surfaces were simulated using the finite element simulation. The distribution of stress around the indentation tip is shown by different colours, because PAAm SN hydrogel is nearly elastic, the dissipation zone is very small, or almost negligible, there is a very small difference in stress distribution around the indentation tip. In contrast, DN hydrogel shows different or gradient colours around the indentation tip, which indicates the gradient stress distributions around the tip. Large and nonlinear deformation should be considered around the indentation tip for the tough DN hydrogel[9].

### 4.3.3 Quantifying regioselective internal fracture on DN hydrogel surfaces

Herein, the internal fracture on hydrogel surface was quantified by the hysteresis energy $U_{\mathrm{hys}}$ and maximum force $F_{\mathrm{max}}$ of the DN hydrogel surface as a function of the indentation displacement $L_{\mathrm{max}}$. Upon cyclic mechanical indentation, DN hydrogel effectively dissipated energy around the indentation tip, as indicated by the pronounced strain hysteresis[10]. In contrast, the nearly elastic PAAm SN hydrogel exhibited negligible strain hysteresis in cyclic indentation. The dissipated mechanical energy was considered for homolytic cleavage of the first brittle network strands in the pressed region. To compare the tiny mechanical differences between DN gel-glass and DN gel-Si-PET-0.8kPa surfaces, various load displacements were used to detect the hysteresis energy and maximum force for DN gel-glass and DN gel-Si-PET-0.8kPa hydrogel surfaces. Because an excessively large $L_{\mathrm{max}}$ (>1000 μm) induced surface microcracks, $L_{\mathrm{max}}$ was controlled in the range of 0–1000 μm to avoid the formation of microcracks. Here, $U_{\mathrm{hys}}$ was estimated from $U_{\mathrm{hys}} = \int_0^{L_{\mathrm{max}}} (F_{\mathrm{load}} - F_{\mathrm{unload}})\mathrm{d}L$, where $F_{\mathrm{load}}$ and $F_{\mathrm{unload}}$ are the mechanical force values of the indentation loading and unloading curves, respectively. There was a linear relationship between maximum force and displacement for DN gel-glass. However, the relationship between hysteresis energy and displacement was complex and non-linear. At small displacement $L_{\mathrm{max}}$ (< 500 μm), there was a linear relationship between $L_{\mathrm{max}}$ and $U_{\mathrm{hys}}$, with a slope of $4.6\times10^{-8}$ J $\mu m^{-1}$. The DN gel-glass hydrogel surface underwent larger deformation at $L_{\mathrm{max}}$ above 500 μm, where the energy dissipation increased sharply. The DN gel-Si-PET-0.8kPa surface was stiffer than that of DN gel-glass, because the rigid first network was exposed on the surface of DN gel-Si-PET-0.8kPa. When the indentation displacement was 100 μm, the hysteresis energy was $0.8\times10^{-7}$ J for DN gel-Si-PET-0.8kPa surface, the smaller hysteresis energy was $0.3\times10^{-7}$ J for DN gel-glass hydrogel surface, but the maximum forces for the different DN hydrogel surfaces were almost same (i.e. 0.03 N). We propose that the soft PAAm layer on DN hydrogel surface acts as a stretchable and elastic protect layer based on the finite element simulation and the difference in mechanical hysteresis energy. The stress field around the indentation tip for PAAm, DN gel-glass and DN gel-Si-PET-0.8kPa was shown in **Figure 4-10**, there was contact damage on DN gel-Si-PET-0.8kPa surface from the cylindrical steel indenter owing to the mechanical contact or friction between the stiff indenter tip and soft hydrogel surface.

### 4.3.4 Fast reswelling of the process zone on DN hydrogel surfaces

Here, we focused on the DN gel-Si-PET-0.8kPa surface, mechanical damage, and fast reswelling phenomenon. Process zone (i.e. damage zone) on DN gel-Si-PET-0.8kPa surface was produced by regioselective indentation in air. Then the process zone was observed by a 3D laser microscope immediately. The indentation displacement was 1000 μm, the value of initial height for the process zone was -38 μm. In fact, the initial height is residual strain after mechanical indentation, smaller than the indentation displacement, owing to the elastic contribution of the second stretchable network. Time-lapse microscope observation shows the evolution of process zone on DN hydrogel surface with time, the topographic height of process zone increases from -38 μm to 12 μm in the initial immersion time (within 10 s). The time scale of the swelling is governed by the diffusion of the polymer network and water[11,12]. In our system, we found that the time scale for swelling to equilibrium of a small process zone (thickness of 1000 μm and diameter of 600 μm) was within 1 min.

### 4.3.5 Quantifying the amount of mechanoradical in the process zone

A hydrogel consisted of cross-linked polymer chains, the polymer chains fluctuate by thermal motion and can be stretched to break by a force[13]. Herein, the DN hydrogel was selectively damaged by mechanical indentation. The mechanical energy input by regioselective indentation was considered for polymer strand scission of the first rigid network in our DN hydrogel system, if the viscous dissipation and hydrodynamics were negligible. Mechanoradical, the radical produced by force-triggered polymer strand homolytic scission. The bond scission during tension is essentially a thermally activated process, which may also be modelled as an ultrafast first-order kinetic process[14,15]. The time scale for bond scission was estimated as $10^{-12}$ s for a polymer strand that experiences a force of ~6 nN[15]. The dissipated energy per mole of strands of the first network was estimated based on the analysis by Lake and Thomas[16]. Here, the mechanical energy required to break one C-C covalent bond, $\Delta U_{\mathrm{act}}$, that is considered be 25% of the C-C bond dissociation energy $E_{\mathrm{b}}$ (~350 kJ/mol). The number of C-C bonds in the bridging strands of the first network, $N$, was estimated by using the affine network theory[17]. Here, $N$ for the first network in the current study (synthesized from 1.0 M NaAMPS and 40 mM MBA) was estimated to be ~580 according to the published paper[18]. The process zone volume was roughly assumed as $\pi(d/2)^2L_{max}$. For example, when $L_{max}$ was 1000 μm, the volume of process zone was $\pi(568\ \mu m/2)^2 \times 1000\ \mu m = 2.53\times10^{-7}\ dm^3$, and the hysteresis energy $U_{hys}$ was $1.87\times10^{-4}$ J. The mechanical energy $U$ required to break a polymer strand with $N$ monomers was estimated as $U = N\Delta U_{act} \approx 580 \times (350\ kJ\ mol^{-1} \times 0.25) = 5.1\times10^7\ J\ mol^{-1}$. The number of moles of mechanoradical was $2(U_{hys}/U) = 7.4\times10^{-12}$ mol, and the mechanoradical concentration was roughly estimated as $(7.4\times10^{-12}\ mol)/(2.5\times10^{-7}\ dm^3) = 2.9\times10^{-5}\ mol\ dm^{-3}$ or $2.9\times10^{-5}$ M. The concentration of mechanoradical increased with the load displacement, as shown in **Figure 4-14**.

## 4.4. Summary

PAAm single-network hydrogel surface shows nearly elasticity owing to the large amount of water molecules between the polymer chains and the affine deformation of polymer networks. DN gel-Si-PET-0.8kPa surface show tough properties and non-linear large deformation, because the first rigid network is on the top-most surface layer of hydrogel. Large and gradient process zones occur around the indentation tip, the bonds scission in the process zone dissipate a lot of mechanical energy. Contact damage is produced by the direct physical contact and friction between steel indenter and hydrogel surface for DN gel-Si-PET-0.8kPa. Because an excessively large $L_{max}$ (>1000 μm) induced surface microcracks, $L_{max}$ was controlled in the range of 0–1000 μm to avoid the formation of microcracks on DN gel-Si-PET-0.8kPa surface. Fast reswelling of the process zone on DN hydrogel surface occurs within 1 min. The reswollen region have a maximum height of ~20 μm and a diameter of ~560 μm, when the indenter diameter is ~568 μm and displacement is ~1000 μm. These quantitative results confirmed that covalent bonds ruptured locally near the mechanical indention tip, which produced mechanoradicals in this localized process zone.

## References

1. T. Nakajima, H. Sato, Y. Zhao, S. Kawahara, T. Kurokawa, K. Sugahara, and J. P. Gong. A universal molecular stent method to toughen any hydrogels based on double network concept. *Adv. Funct. Mater.* **22**, 4426−4432 (2012).
2. R. E. Webber, C. Creton, H. R. Brown, and J. P. Gong. Large strain hysteresis and Mullins effect of tough double-network hydrogels. *Macromolecules* **40**, 2919−2927 (2007).

3. J. P. Gong. Why are double network hydrogels so tough? *Soft Matter* **6**, 2583−2590 (2010).
4. T. Matsuda, T. Nakajima, Y. Fukuda, W. Hong, T. Sakai, T. Kurokawa, U. Chung, and J. P. Gong. Yielding criteria of double network hydrogels. *Macromolecules* **49**, 1865−1872 (2016).
5. S. M. Liang, Z. L. Wu, J. Hu, T. Kurokawa, Q. M. Yu, and J. P. Gong. Direct observation on the surface fracture of ultrathin film double-network hydrogels. *Macromolecules* **44**, 3016−3030 (2011).
6. R. Long, C. Y. Hui, J. P. Gong, and E. Bouchbinder. The fracture of highly deformable soft materials: a tale of two length scales. *Annu. Rev. Condens. Matter. Phys.* **12**, 71−94 (2021).
7. M. Frauenlob, D. R. King, H. L. Guo, S. Ishihara, M. Tsuda, T. Kurokawa, H. Haga, S. Tanaka, and J. P. Gong. Modulation and characterization of the double network hydrogel surface-bulk transition. *Macromolecules* **52**, 6704−6713 (2019).
8. S. Hassan, J. Kim, and Z. G. Suo. Polyacrylamide hydrogels. IV. Near-perfect elasticity and rate-dependent toughness. *J. Mech. Phys. Solids* **158**, 104675 (2022).
9. I. Kolvin, J. M. Kolinski, J. P. Gong, and J. Fineberg. How supertough gels break. *Phys. Rev. Lett.* **121**, 135501 (2018).
10. J. Y. Sun, X. H. Zhao, W. R. K. Illeperuma, O. Chaudhuri, K. H. Oh, D. J. Mooney, J. J. Vlassak, and Z. G. Suo. Highly stretchable and tough hydrogels. *Nature* **489**, 133−136 (2012).
11. T. Tanaka, D. J. Fillmore. Kinetics of swelling of gels. *J. Chem. Phys*. **70**, 1214−1218 (1979).
12. T. Fujiyabu, T. Sakai, R. Kudo, Y. Yoshikawa, T. Katashima, U. Chung, and N. Sakumichi. Temperature dependence of polymer network diffusion. *Phys. Rev. Lett.* **127**, 237801 (2021).
13. J. Kim, G. G. Zhang, M. Shi, and Z. G. Suo. Fracture, fatigue, and friction of polymers in which entanglements greatly outnumber cross-links. *Science* **374**, 212−216 (2021).
14. A. F. Horn, E. W. Merrill. Midpoint scission of macromolecules in dilute solution in turbulent flow. *Nature* **312**, 140−141 (1984).
15. M. K. Beyer. The mechanical strength of a covalent bond calculated by density functional theory. *J. Chem. Phys.* **112**, 7307−7312 (2000).
16. G. J. Lake, A. G. Thomas. The strength of highly elastic materials. *Proc. R. Soc. Lond. A* **300**, 108−119 (1967).
17. M. Rubinstein. *Polymer Physics* Ch. 7 (Oxford Univ. Press, 2003).
18. T. Matsuda, R. Kawakami, R. Namba, T. Nakajima, and J. P. Gong. Mechanoresponsive self-growing hydrogels inspired by muscle training. *Science* **363**, 504−508 (2019).

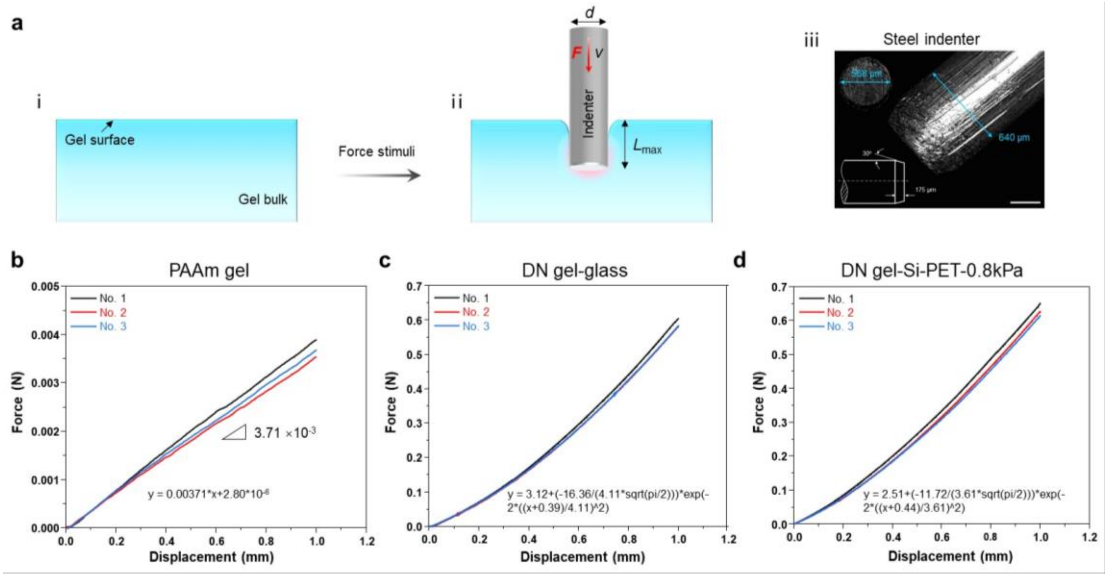

**Figure 4-1.** Mechanical indentation on hydrogel surfaces using a cylindrical steel indenter. **a**. Schematic illustration of the regioselective indentation on hydrogel surface, microscope image and scale of the cylindrical steel indenter. **b**. Force-displacement of three indentation on PAAm hydrogel surface, the linear function was Gaussian function fitting for the mean of three replicates. **c**. Force-displacement of three indentation on DN gel-glass hydrogel surface, the non-linear function was Gaussian function fitting for the mean of three replicates. **d**. Force-displacement of three indentation on DN-Si-PET-0.8kPa surface, the non-linear function was Gaussian function fitting for the mean of three replicates.

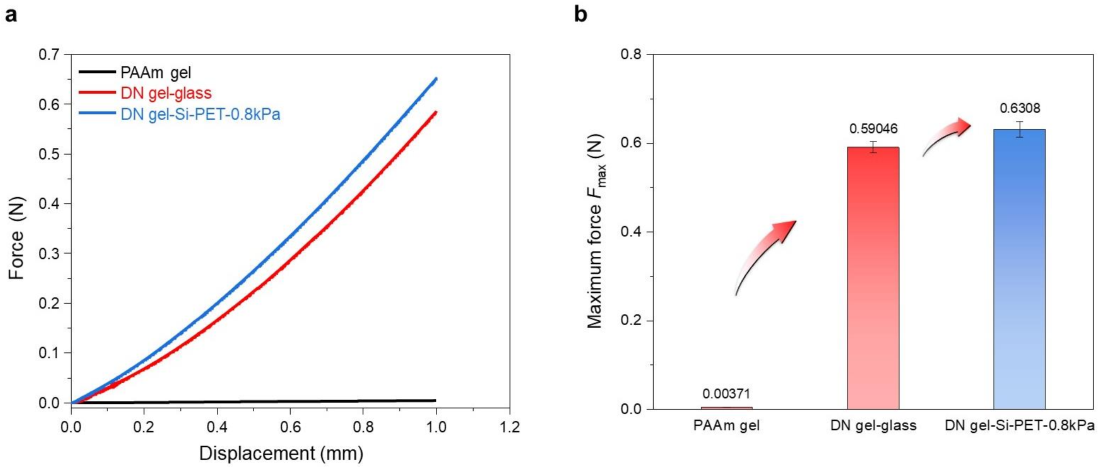

**Figure 4-2. a**. Comparative analysis of the force-displacement for different hydrogel surfaces. **b**. The maximum force $F_{max}$ of the mechanical indentation for different hydrogel surface, when the indentation displacement was 1 mm. Error bar represents the standard deviation for three replicates. Data in **b** are presented as mean values +/- standard deviation (SD).

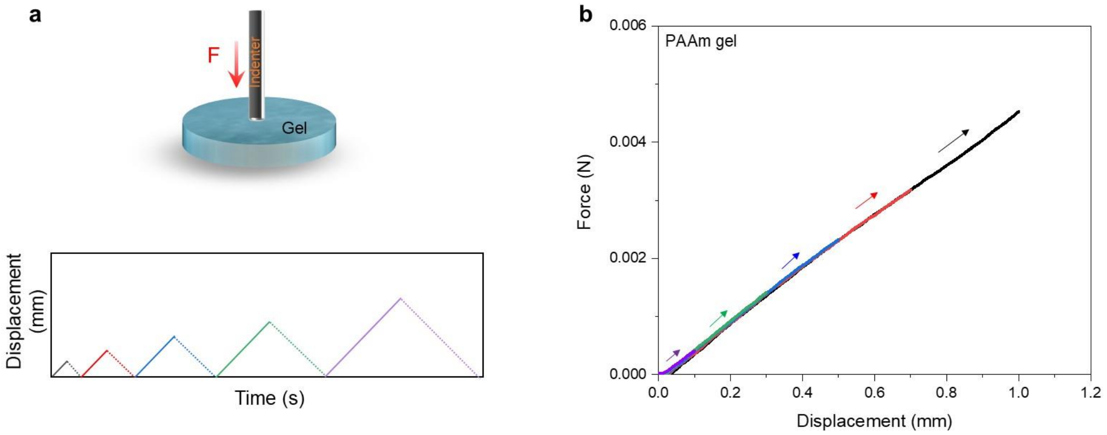

**Figure 4-3.** Cyclic mechanical indentation on PAAm SN hydrogel surface. **a**. Schematic illustration of the regioselective cyclic indentation on hydrogel surface. **b**. Linear force-displacement curves of the cyclic indentation on PAAm SN hydrogel surface.

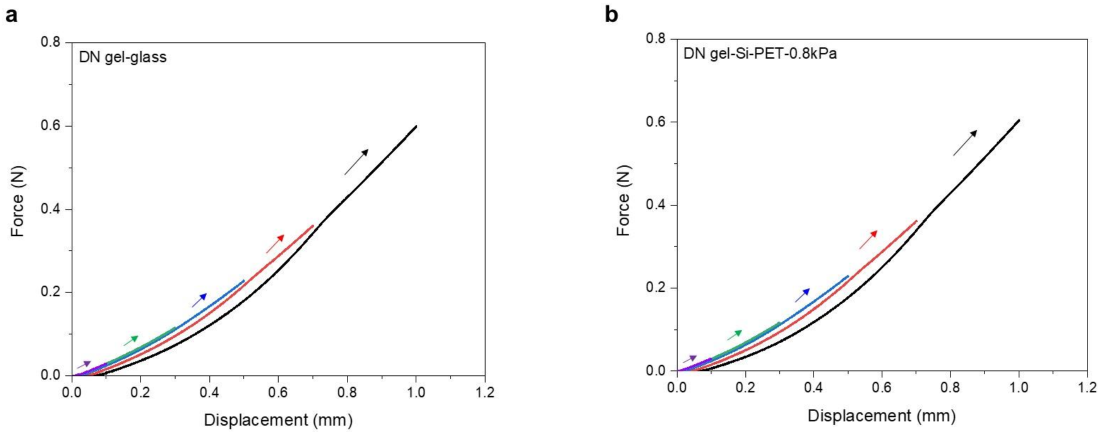

**Figure 4-4. a**. Force-displacement curves of the cyclic indentation on DN gel-glass hydrogel surface. **b**. Force-displacement curves of the cyclic indentation on DN-gel-Si-PET-0.8kPa surface.

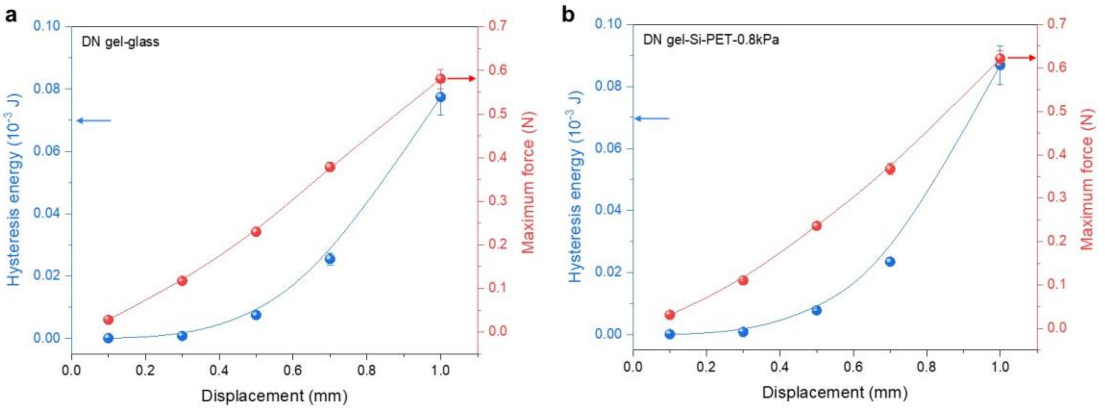

**Figure 4-5.** Quantitative analysis of the mechanical cyclic indentation on different DN hydrogel surfaces. **a**. The hysteresis energy $U_{\mathrm{hys}}$ and maximum force $F_{\mathrm{max}}$ measured at various indentation displacements $L_{\mathrm{max}}$ by mechanical indentation without monomer supply in the air (a cylindrical steel indenter diameter was $d$ = 568 μm, the velocity of indentation was 1 mm min$^{-1}$, DN gel-glass hydrogel thickness was ~3.8 mm). **b**. The hysteresis energy $U_{\mathrm{hys}}$ and maximum force $F_{\mathrm{max}}$ measured at various indentation displacements $L_{\mathrm{max}}$ by mechanical indentation for DN gel-Si-PET-0.8kPa. The $U_{\mathrm{hys}}$ was estimated from $U_{\mathrm{hys}} = \int_0^{L_{max}} (F_{\mathrm{load}} - F_{\mathrm{unload}})\mathrm{d}L$. Error bars represent standard deviation from three replicates. Data in **a** and **b** are presented as mean values +/- standard deviation (SD).

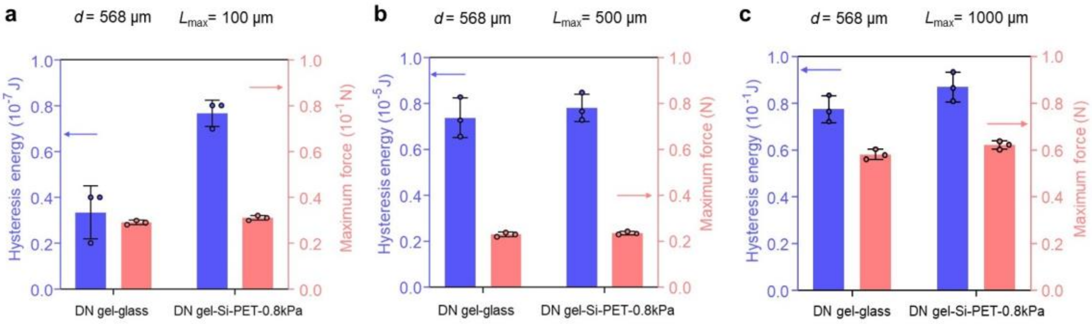

**Figure 4-6.** Comparison and analysis of the hysteresis energy and maximum force at different small displacements. **a**. The hysteresis energy $U_{\mathrm{hys}}$ and maximum force $F_{\mathrm{max}}$ for DN gel-glass and DN gel-Si-PET-0.8kPa surfaces when the indentation displacement was 100 μm. **b**. The hysteresis energy $U_{\mathrm{hys}}$ and maximum force $F_{\mathrm{max}}$ for DN gel-glass and DN gel-Si-PET-0.8kPa surfaces when the indentation displacement was 500 μm. **c**. The hysteresis energy $U_{\mathrm{hys}}$ and maximum force $F_{\mathrm{max}}$ for DN gel-glass and DN gel-Si-PET-0.8kPa surfaces when the indentation displacement was 1000 μm. Error bars represent standard deviation from three replicates. The circular dots of the histogram in **a**, **b** and **c** represent the measured data points of three. Data in **a**, **b** and **c** are presented as mean values +/- standard deviation (SD).

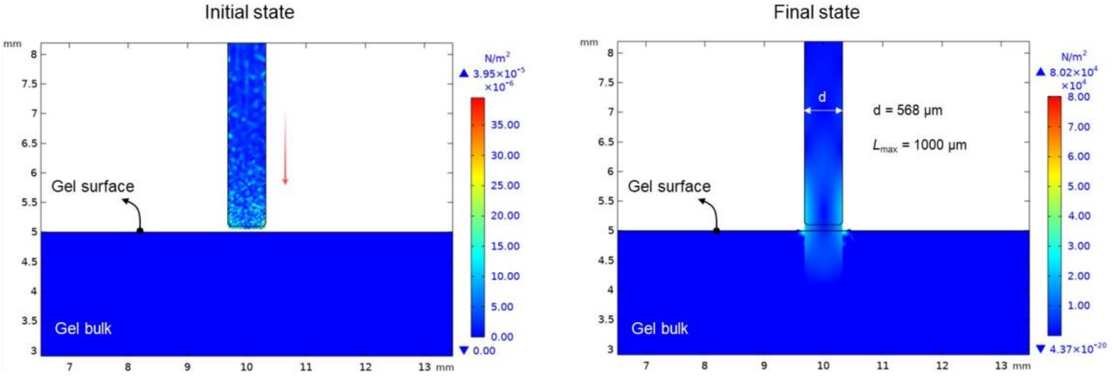

**Figure 4-7.** Finite element simulation was performed in COMSOL Multiphysics 5.6 using the Solid Mechanics module. Initial state shows the cylindrical steel indenter down to the PAAm hydrogel surface. Final state shows the indenter is pressed into PAAm hydrogel. Color scale shows the stress distribution around the indentation tip.

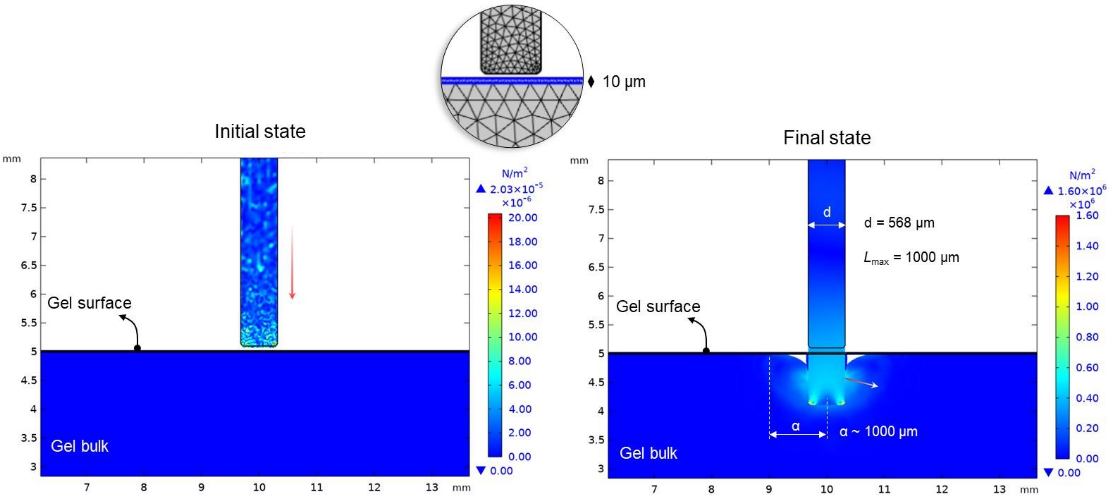

**Figure 4-8.** Finite element simulation was performed in COMSOL Multiphysics 5.6 using the Solid Mechanics module. Initial state shows the cylindrical steel indenter down to the DN gel-glass hydrogel surface. Final state shows the indenter is pressed into DN gel-glass hydrogel. There is a soft and pure elastic PAAm layer, ~10 μm thick, on the top-most surface of hydrogel. Color scale shows the stress distribution around the indentation tip.

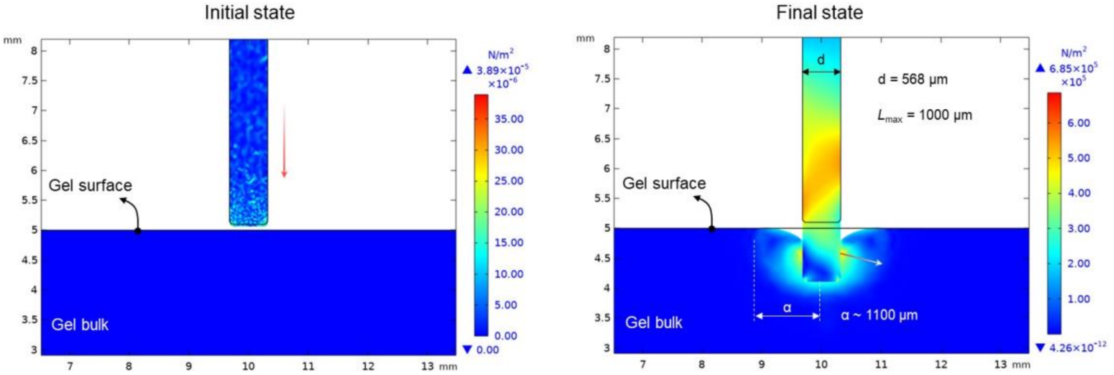

**Figure 4-9.** Finite element simulation was performed in COMSOL Multiphysics 5.6 using the Solid Mechanics module. Initial state shows the cylindrical steel indenter down to the DN gel-Si-PET-0.8kPa surface. Final state shows the indenter is pressed into DN gel-Si-PET-0.8kPa. Color scale shows the stress distribution around the indentation tip.

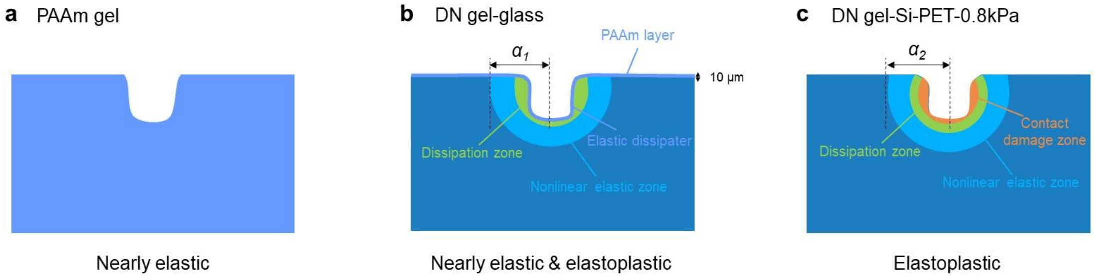

**Figure 4-10.** Stress field distribution around the indentation tip on different hydrogel surfaces based on the finite element simulation. **a**. PAAm SN hydrogel shows nearly elasticity without obvious dissipation zone and complex stress distribution. **b**. DN gel-glass with PAAm layer shows obvious dissipation zone under the PAAm layer, there is no contact damage from the steel indenter owing to the protection of PAAm layer. **c**. DN gel-Si-PET-0.8kPa without PAAm layer shows contact damage zone, dissipation zone and nonlinear elastic zone. Specially, there is contact damage on hydrogel surface from the steel indenter.

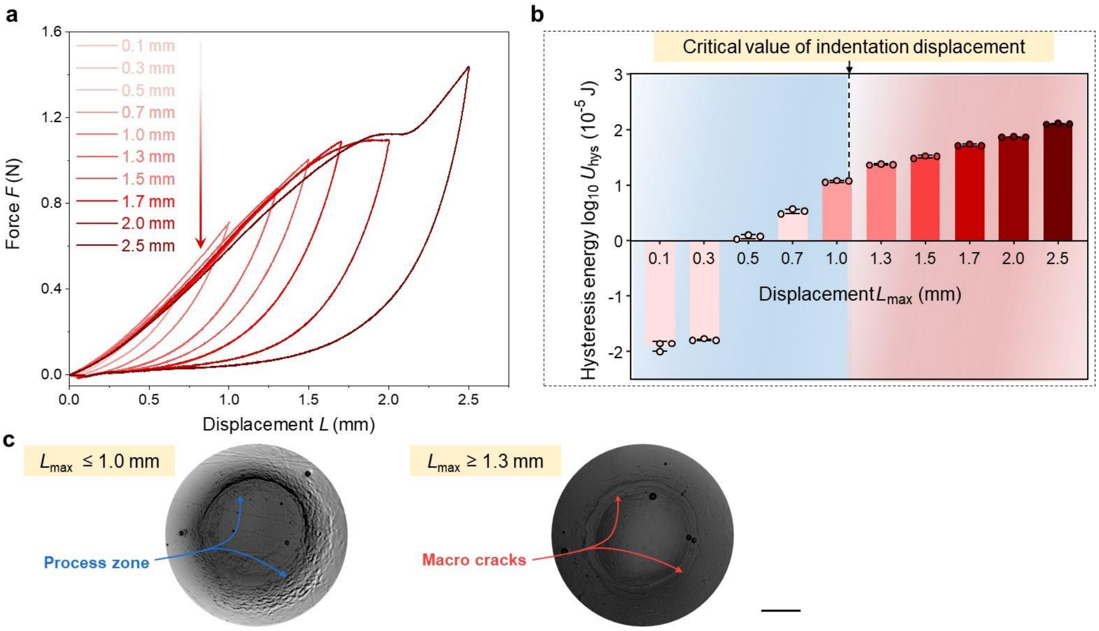

**Figure 4-11.** Mechanical indentation on the DN gel-Si-PET-0.8kPa surfaces with different displacements $L_{\max}$ using a cylindrical steel indenter, DN hydrogel thickness was ~3.8 mm. **a**. Pronounced hysteresis for the different mechanical indentation displacements. **b**. Calculated hysteresis energy for different indentation displacements. **c**. Microscope images of the process zones on DN hydrogel surfaces. When displacement $L_{\max}$ was increased beyond 1.0 mm, macro cracks appeared on DN hydrogel surfaces, which was marked by the arrow. Accordingly, the maximum displacement of intender without macroscopic damage was 1.0 mm. The displacement velocity was 1 mm min$^{-1}$. Error bars represent standard deviation from three replicates. The circular dots of the histogram in **b** represent the measured data points of three. Data in **b** are presented as mean values +/- standard deviation (SD). Scale bar, 200 µm.

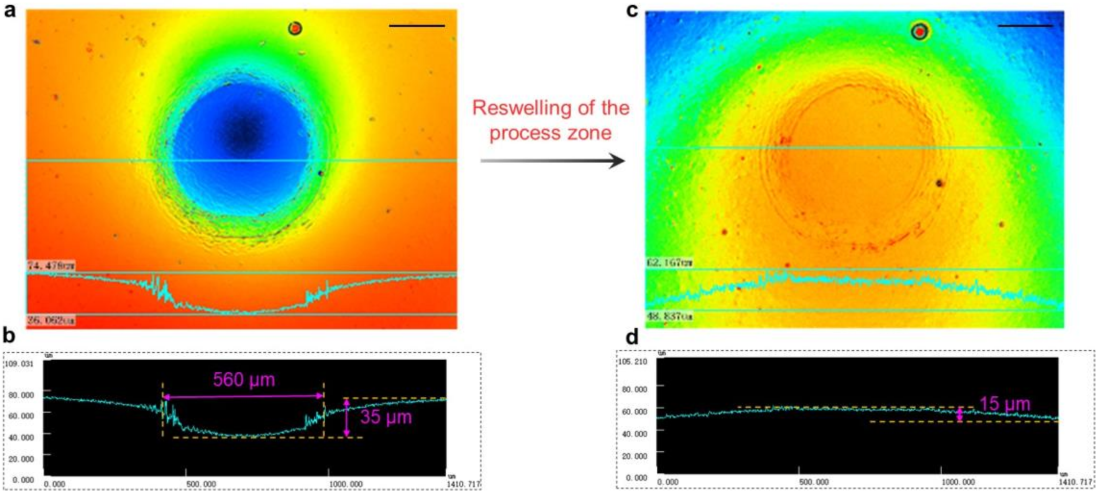

**Figure 4-12.** Reswelling of the process zone (or damaged zone) on DN gel-Si-PET-0.8kPa surfaces. Immersion time in water for the reswelling was several seconds. **a**. Image of the process zone on DN hydrogel surface. **b**. Profile and size of the process zone. **c**. Image of the reswollen zone on DN hydrogel surface**.** **d**. Profile and height of the reswollen zone. Scale bar, 200 μm. A cylindrical steel indenter of diameter $d$ = 568 μm and displacement $L_{\max}$ = 1000 μm, DN hydrogel thickness was ~3.8 mm.

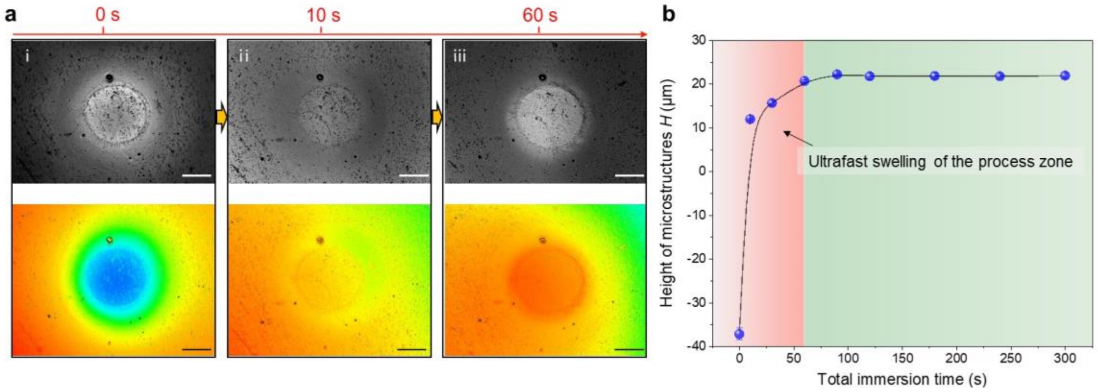

**Figure 4-13.** Observation of the fast swelling on DN gel-Si-PET-0.8kPa surface, the process zone was created by regioselective indentation under deionized water without monomer (cylindrical steel indenter diameter was ~568 μm, displacement was ~1000 μm). **a**. The process zone morphology changed over the immersion time. The area of process zone was around ~0.1 mm$^2$. **b**. Height of reswollen microstructure changed over the immersion time (time scale of equilibrium swelling was approximately 60 s). The height $H$ of a DN hydrogel surface for different total immersion times $t$ were characterized as follows. First, an indented DN gel surface was observed by the microscope in air ($t$ = 0 s, Figure 4-13 a (i)). The gel was then immersed in water for 10 s, picked up from water and wiped by clean tissues, then observed by the microscope in air ($t$ = 10 s, Figure 4-13 a (ii)). Afterwards, the gel was immersed in water for 20 s followed by the microscope observation in the same manner (total immersion time $t$ = 10 + 20 = 30 s). Such protocol was repeated several times for this DN hydrogel surface, resulting in $H$ as a function of $t$ up to 300 s. The light red shading in b indicates the fast swelling of the damage zone, the light green shading indicates the equilibrium process. Error bar represents the standard deviation for three replicates. Some error bars in **b** are hidden by the symbols. Data in **b** are presented as mean values +/- standard deviation (SD). Scale bars, 200 μm.

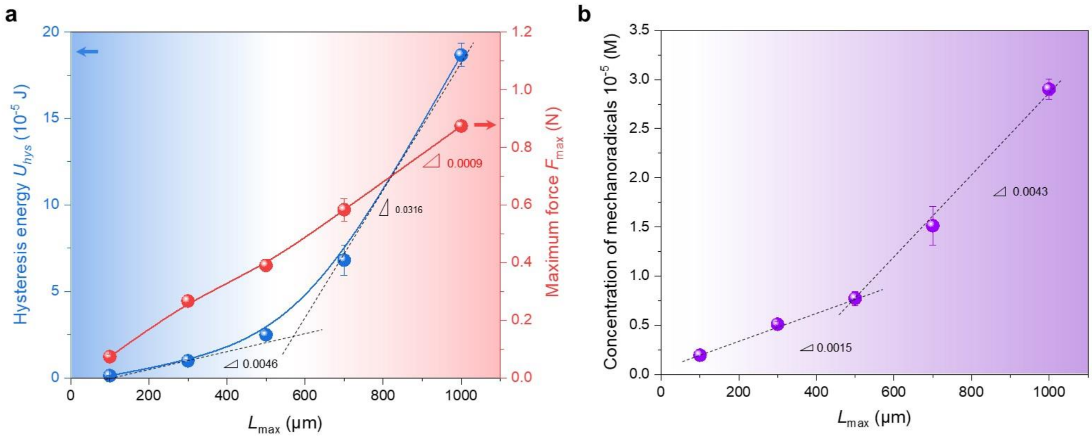

**Figure 4-14.** **a**. The hysteresis energy $U_{\mathrm{hys}}$ and maximum force $F_{\max}$ measured at various indentation displacements $L_{\max}$ by mechanical indentation without monomer supply in the air (a cylindrical steel indenter diameter was $d$ = 568 μm, the velocity of indentation was 1 mm min$^{-1}$, DN hydrogel thickness was ~3.8 mm). The $U_{\mathrm{hys}}$ was estimated from $U_{\mathrm{hys}} = \int_0^{L_{max}} (F_{\mathrm{load}} - F_{\mathrm{unload}})\mathrm{d}L$. **b**. The concentration of mechanoradicals in the process zone changed with indentation displacement $L_{\max}$. Error bar represents the standard deviation for three replicates. Some error bars in **a** and **b** are hidden by the symbols. Data in **a** and **b** are presented as mean values +/- standard deviation (SD).

# Chapter 5: Force-Triggered Rapid Microstructure Growth on Hydrogel Surfaces

## 5.1. Introduction

Hydrogel surfaces with microstructures have broad application scope ranging from adhesion and tissue engineering to actuators and flexible displays[1-3]. These microstructures are not limited to shape but include the surface distribution of physical and chemical properties, such as physical stiffness and chemical species. The chemical/physical microstructures on hydrogel surfaces are important for practical use, especially on tough double-network (DN) hydrogels that have promising applications as structural biomaterials. Despite great success in patterning synthetic materials, such as lithography, printing, buckling instabilities, and moulding. It remains largely unexplored to creating microstructures on DN hydrogel surfaces, the main challenges are: 1) the rigid and easily brittle nature of the highly pre-stretched first networks will lead to the failure of moulding; 2) there is a layer of polyacrylamide (PAAm, thickness: ~2.2 μm) without chemical modification sites on the normal DN hydrogel surfaces.

The hydrogel coded with DN gel-Si-PET-0.8kPa has a rough and rigid surface (elastic modulus is ~600 kPa). The first rigid network on the hydrogel surface determines the elastic modulus of the whole surface. Upon mechanical indentation, DN gel-Si-PET-0.8kPa surface deforms to fracture, and the mechanical fracture in the process zone is accompanied by homolysis of the first rigid network, which generates mechanoradicals at the broken ends of polymer strands[4-6]. The concentration of mechanoradicals is sufficiently high to initiate radical polymerization inside DN hydrogels fed with monomers, which enables force-triggered growth of DN hydrogels in the presence of reactive monomers and crosslinkers. Monomers and crosslinkers act as growth-building elements, analogous to nutrients in the natural growth of living organisms. The newly synthesized polymer strands enable novel mechanical properties or functions of DN hydrogel surfaces. In our previous work, the mechanical force was typically applied uniformly to the DN hydrogel so that the polymerization proceeded homogeneously inside the hydrogel bulk[4]. In the present work, we applied local mechanical indentation on DN hydrogel surfaces under a monomer aqueous solution, which induced regioselective polymerization of monomers on DN hydrogel surfaces resulting in various microstructures on hydrogel surfaces. As radical polymerization is applicable to various functional unsaturated monomers, force-triggered polymerization in DN hydrogels can, in principle, impart various chemical functions to the hydrogels. The rapid growth of microstructures includes three main processes: bond scission, chain growth, and swelling. Time-resolved near-infrared spectroscopy revealed that the force-triggered radical polymerization was almost completed within tens of seconds.

In this chapter, we mainly focused on the rapid microstructure growth on DN hydrogel surfaces triggered by mechanical force, and studied the quantitative relationship between microstructure feature height and hysteresis energy. We found that the force-triggered rapid strategy is chemical species-dependent, spatially controllable, and allows fine modulation of the size and composition of microstructures.

## 5.2. Experiments

### 5.2.1 Materials

Deionized water ($H_2O$) used was purified by a lab water purification system (Merck KGaA, Darmstadt, Germany). Acrylamide (AAm) was purchased from Junsei Chemical, 2-Acrylamido-2-methylpropanesulfonic acid sodium salt (NaAMPS) (49.7 wt % aqueous solution) was provided by Toa Gosei. *N*-isopropylacrylamide (NIPAm), acrylic acid (AAc), sodium *p*-styrenesulfonate (NaSS), 3-(methacryloylamino)propyltrimethylammonium chloride (MPTC),*N,N'*-Methylenebisacrylamide (MBA), and 2-oxoglutaric acid (α-keto) were purchased from Fujifilm Wako Pure Chemical Corporation. 8-Anilino-1-naphthalenesulfonic acid (ANS) was purchased from Tokyo Chemical Industry. Inc. Soda-lime glass plates and silicon rubbers were purchased from As One Corporation.

### 5.2.2 Regioselective indentation on DN hydrogel surfaces under monomer solution

The regioselective indentation on hydrogel surface was performed in an argon glove box using a mechanical tester (MCT-2150, A&D Co., Ltd.). Firstly, the cut DN hydrogels were immersed in deionized water to remove the residual monomers for at least two weeks. The DN hydrogels were immersed into a solution of different reactive monomers and crosslinkers overnight to incorporate the nutrients for subsequent surface microstructures growth. Then the DN hydrogels containing monomers and crosslinkers were first fixed on a rigid glass plate by super glue, which were moved to an argon glove box (MBRAUN, oxygen concentration less than 100 ppm) to remove oxygen. The DN hydrogels were indented selectively under the monomer solutions by a cylindrical steel indenter, which was fixed on the small tensile machine using a screw. After the indentation, the hydrogels were left still in the monomer solution for approximately 4 min, then they were picked up from the glove box. Finally, the hydrogels were immersed in deionized water for at least 1 min to obtain swollen microstructures on the hydrogel surfaces. The complex patterns on DN hydrogel surfaces or in hydrogel bulks were prepared using the three-dimensional (3D) printed resin indenters (designed by a commercial software Solidworks then printed by a commercial high-precision 3D printer system (Agilista 3100, Keyence Co., Ltd.), feature height is ~2 mm for all the 3D printed patterns). The parallel patterns were prepared using the home-made stacked metal blades, and the distance between the two blades was controlled using silicone rubber spacers (distance: 200 μm and 500 μm, typically).

### 5.2.3 In-situ transmission Fourier-transform near-infrared (FT-NIR) spectroscopy

To quantify different monomers conversion ratio in the force-triggered radical polymerization, an in-situ transmission FT-NIR spectroscopy was used. The near-infrared spectroscopy is sensitive to overtone and combinations of vibrational vibrations[7-9]. We found that there was a characteristic absorption peak at approximately 1613–1639 nm (wavenumber is 6100–6200 $\mathrm{cm}^{-1}$, within the near-infrared region) corresponds to C–H overtone stretching at the C=C double bond of alkene monomers. We performed the measurements in a customized small glove box filled with argon, DN hydrogels fed with different monomers were stretched to an over-yielding tensile strain ($\varepsilon \sim 3$) by a set of home-made clamps, the strain rate was ~1 $\mathrm{s}^{-1}$ and it took approximately ~6 s in the loading-unloading process, the tensile stress was around ~0.9 MPa. The absorbance $A$ was divided by sample thickness $l$, (i.e. the normalized absorbance $A/l$). The normalized absorbance was analyzed by the Beer-Lambert law[10], which was normally combined in the following mathematical equation.

$$A = \log_{10}\left(\frac{I_o}{I}\right) = \epsilon l c \tag{5-1}$$

$$A/l \propto c \tag{5-2}$$

where $\epsilon$ is the molar absorption coefficient ($\mathrm{M}^{-1}\mathrm{cm}^{-1}$), $c$ is the molar concentration of the attenuating substances (M), $I_\mathrm{o}$ is the intensity of incident infrared light, and $I$ is the intensity of transmitted infrared light. Note that $\epsilon$ is a characteristic constant related to the substances, so the value of $A/l$ is proportional to the molar concentration of substances.

The normalized absorbance $A/l$ is proportional to monomer concentration $c$ based on the Beer-Lambert law. The measurement background was the DN hydrogel without monomers, the baseline of water and polymer networks was subtracted in this experimental section. We firstly confirmed the transmission near-infrared spectrum calibration curves of DN hydrogels fed with different monomers (monomer concentration from 0 to 1.0 M) prior to the monomer conversion ratio measurements. A linear correlation between the normalized absorbance peak area $S$ and the monomer concentration $c$ was observed for DN hydrogels fed with different monomers. The observed normalized absorption peak area $S$ (selected peak area region within 6250–6100 cm$^{-1}$, unit/cm) depended on the monomer concentration.

$$S = \alpha c \tag{5-3}$$

Where $\alpha$ is the proportional constant which slightly depends on the monomer species ($\alpha$ is 9.14, 9.30, 11.95, and 10.38 for the monomers NIPAm, AAc, NaSS, and MPTC, respectively).

We measured the change of monomer concentration in tough DN hydrogel bulks before stretching and after stretching using the in-situ FT-NIR. The force-triggered variation in monomer concentration was associated with a change in transmitted light intensity at the monomer peak position around 6200–6100 cm$^{-1}$.

Here, the sample thickness $I$ was the initial thickness of DN hydrogels with monomers before stretching, under an assumption that thickness change by stretching is negligibly small. Since the normalized absorption peak area $S$ of different monomers is proportional to monomer concentration, the monomer conversion ratio (Conv) can be calculated based on the equation.

$$\begin{aligned}\mathrm{Conv} &= (1 - c_{\mathrm{t}}/c_{\mathrm{o}}) \\ &= (1 - S_1/S_0)\end{aligned} \tag{5-4}$$

Here, $c_{\mathrm{t}}$ and $c_0$ is the monomer concentration at time $t$, and initial monomer concentration, respectively. $S_1$ and $S_0$ is the normalized absorption peak area of the monomers at time $t$ and the initial time. The conversion ratio of monomer NIPAm was around 0.7 in the force-triggered radical polymerization at 1 min after the uniaxial stretching. Then we measured the transmission near-infrared spectrum change for different monomers (initial concentration was 1.0 M) when the radical polymerization time was fixed at 1 min, as shown in **Figure 5-9**. Monomer conversion ratios for different monomers (NaAMPS, NIPAm, AAc, NaSS, and MPTC) were 0.802 ± 0.005, 0.692 ± 0.007, 0.498 ± 0.016, 0.459 ± 0.008, and 0.593 ± 0.025, respectively. Error ranges represent standard deviation from three replicates. The measurement parameters for in-situ transmission FT-NIR were constant in the experiment. The number of scans was 32 that took around 20 s (hence the measured values at 1 min are the average of approximately 60–80 s after the stretching), resolution was 2 $cm^{-1}$, detector was triglycine sulfate (TGS), region of the spectral scan was 6300–6000 $cm^{-1}$, sample thickness was around ~2.5 mm.

### 5.2.4 Time-resolved near-infrared spectroscopy measurements

To study the kinetics of force-triggered radical polymerization with different monomers, a time-resolved near-infrared spectroscopy was used[11]. The rapid scan system of the spectroscopy enables the instrument to measure the spectrum every 0.07–0.08 s (one scan per one data) for providing real-time analysis of chemical reaction kinetics. The DN hydrogels with different monomers (NaAMPS and NIPAm, initial concentration was 1.0 M without crosslinker) were stretched to an over-yielding tensile strain ($\varepsilon \sim 3$) in a customized small glove box filled with argon, the strain rate was ~3 $s^{-1}$ and it took approximately ~1 s in the loading process, the tensile stress was around ~0.9 MPa, the thickness of DN hydrogels with different monomers was 1.5–2 mm. We measured the absorption value change for only one wavenumber (6175 $cm^{-1}$) in the time-resolved test. Monomer concentration decay during the polymerization was detected by the near-infrared spectroscopy at 298 K (25 °C), which was fast and highly efficient (within tens of seconds) in our force-triggered radical polymerization system. For smoothing the data, we took the moving average of the absorbance with a width of ± 0.3 s.

## 5.3. Results and discussion

### 5.3.1 Microstructures prepared by reswelling and force-triggered growth

To realize surface microstructure growth through force-triggered polymerization, DN hydrogels were first immersed in various monomer aqueous solutions. Without any further treatment, these chemically crosslinked DN hydrogels were permeable to small molecules, enabling efficient radical polymerization in the pressed regions of the hydrogel surface. Microstructures growth on hydrogel surface triggered by a regioselective mechanical force was carried out in a homemade experimental setup under an argon atmosphere. After the mechanical indentation followed by swelling, a convex micropattern was formed on the DN hydrogel surface. Unlike the micropatterning, the reswollen microstructure was prepared by damaging the hydrogel surface in the absence of monomers and re-immersing in deionized water.

Herein, four cylindrical steel indenters with different diameters were used to locally press the DN hydrogel surface. The indenter diameters are 84, 341, 568, and 866 μm for a, b, c, and d, respectively (**Figure 5-1**). We observed and measured the microstructure topography using a 3D laser microscope. The results show that topographical height and diameter of microstructures can be regulated by several experiment parameters, such as indentation displacement and indenter diameter. Microstructure diameter is dependent on the diameter of indenter, the diameter of microstructure prepared in NIPAm aqueous solution (initial concentration is 1.0 M) is almost the same as that of steel indenter (**Figure 5-2**). In order to study the difference between reswelling and micropatterning, the surface of the prepared DN hydrogel was locally pressed using a cylindrical steel indenter with a diameter $d$ = 568 μm and displacement $L_{\mathrm{max}}$ = 1000 μm without feeding any monomers in air. Upon mechanical indentation, the DN hydrogel effectively dissipated energy, as indicated by the pronounced mechanical hysteresis. The dissipated mechanical energy was considered for homolytic cleavage of the first brittle network strands in the pressed region. The cleavage of the first network appeared as a reswelling of the pressed region when the sample was re-immersed in deionized water, which occurred because the constraint to the second network by the pre-stretched first network was released by the rupture of the first brittle network. The reswollen region had a saturation height of ~20 μm and a diameter of ~560 μm (**Figure 5-3**), much lower than that of microstructure prepare by micropatterning (i.e. force-triggered radical polymerization).

### 5.3.2 Regulating the topographical height and diameter of microstructures

To investigate the formed microstructures, the pressed DN hydrogels were immersed in deionized water, and the topographical height ($H$) of the prepared microstructures was determined. When regulating the indentation displacement, the hysteresis energy and maximum force was changed for the cyclic indentation (**Figure 5-4**). The hysteresis energy of cyclic indentation was calculated by the mathematical equation, the maximum force is the highest point on the force-displacement curve.

$$U_{\mathrm{hys}} = \int_0^{L_{\mathrm{max}}} (F_{\mathrm{load}} - F_{\mathrm{unload}})\mathrm{d}L \tag{5-5}$$

In **chapter 4**, we have revealed the indentation displacement of 1000 μm is effective for damaging the hydrogel surface and inducing mechanoradicals while avoiding microscopic cracks. Here, the displacement was changed from 0 to 1000 μm, the more mechanoradicals were produced around the crack tip at larger displacement. More mechanoradicals can induce the formation of more new polymer chains in the process zone. Here, we found that the topographical height of microstructure is dependent on the hysteresis energy $U_{\mathrm{hys}}$, as shown in **Figure 5-5 a**. However, the microstructure diameter was almost same for the different displacements (**Figure 5-5 b**). Using selective mechanical indentation, we monitored the patterning and properties of microstructures in well-defined process zones. The height of the microstructures could be regulated by the mechanical hysteresis energy, as revealed by their almost proportional relationship. Therefore, the topographic height, diameter, and shape of the microstructures can be easily regulated based on the application requirements. As force-triggered radical polymerization is generic, we further used a series of monomers to fabricate various microstructures on DN hydrogel surface. The typical profiles, topographic height, and diameter of the microstructures were compared. The anionic monomer NaAMPS showed the highest topographic height among all the evaluated micropatterning systems. There was an obvious dependence between the topographic height and monomer species (**Figure 5-6**).

### 5.3.3 Monomer conversion ratio in force-triggered radical polymerization

To elucidate the underlying mechanisms of micropatterning by using different monomers, we further investigated the monomer conversion ratio in force-triggered radical polymerization. Here, stretched DN hydrogels with monomers were characterized using an in-situ transmission Fourier-transform near-infrared (FT-NIR) spectroscopy (**Figure 5-7**). The results reveal that the conversion ratio of NaAMPS (~0.80) is the highest, and the conversion ratio of NIPAm (~0.69) is higher than those of the other three ionic monomers (AAc, NaSS, and MPTC) in the force-triggered radical polymerization (**Figure 5-9**). We propose that the conversion ratio is one of the main factors causing topographic height differences because a higher conversion ratio induces a higher osmotic pressure difference. The difference in the conversion ratio of these reactive monomers may be related to the substituent groups on the vinyl and/or acryloyl units, or the polarity of the monomer functional groups, which determines the relative stability of the C=C bonds during radical polymerisation[12,13]. Furthermore, we showed that the presence of a crosslinker (*N,N'*-methylenebisacrylamide, MBA) does not affect both the conversion ratio and topographic height (**Figure 5-10**). The topographic height of the microstructures was largely dependent on the fed monomer concentration (**Figure 5-12**). The results demonstrate that the force-triggered radical polymerization rate is higher than that of the local diffusion of monomers.

### 5.3.4 Kinetics of the force-triggered radical polymerization

In order to clearly show the force-triggered radical polymerization of DN hydrogel in situ, a big indenter was used to locally impress a DN hydrogel bar under the monomer solution (concentration of NIPAm was 1.5 M). The turbid part rapidly occurs in the DN hydrogel bulk within 20 s, owing to the force-triggered radial polymerization (**Figure 5-13**). Nearly rapid patterning includes three main processes: bond scission, chain growth, and swelling. The time scale $\bar{\tau}_1$ for bond scission is estimated as $10^{-12}$ s for a polymer strand that experiences a force of ~6 nN[14]. Force-triggered radical polymerisation occurs through molecule-by-molecule addition growth, which implies the sequential formation of individual bonds. The active centres (i.e. chain-end mechanoradicals) induced by bond scission in the polymer backbones are retained by a single polymer molecule throughout its growth. The radicals can be quenched by the well-known chain-terminating process during radical polymerisation[15]. Time-resolved near-infrared spectroscopy revealed that the force-triggered radical polymerisation was almost completed within tens of seconds (**Figure 5-14**); hence, the polymerisation timescale $\bar{\tau}_2$ was estimated to be $10^0$–$10^1$ s. After chain growth, the microstructures immediately swell in an aqueous solution under osmotic pressure. The time scale of the swelling is governed by the diffusion of the polymer network and water. In our system, we found that the time scale $\bar{\tau}_3$ for swelling to equilibrium of a small process zone (thickness of ~1000 μm and diameter of ~600 μm) was within 1 min (**Figure 5-15**). Time-lapse microscope observation of the microstructure on DN hydrogel surface revealed that the rapid micropatterning was finished earlier than 4 minutes (**Figure 5-16**). We propose that the nearly rapid micropatterning is a force and temperature-dependent dynamic process, which is dominated by the above-mentioned three processes. Despite micropatterning occurring through a sequential, multi-step process, the overall rate of micropatterning is determined by the kinetics of the slowest step, i.e. swelling.

## 5.4. Summary

In summary, we demonstrated a facile method for rapid surface patterning of hydrogels via force-triggered growth. Such a force-triggered growth strategy is spatially controllable, allowing fine modulation of the size and shape of microstructures. Microstructures of various size can be customized owing to the quantitative relationship between microstructure height and indentation displacement, monomers, indenter shape and diameter. The nearly rapid microstructure growth is a force and temperature-dependent dynamic process, which is dominated by the three processes: bond scission, chain growing, and swelling. Despite microstructure growth occurring through a sequential, multi-step process, the overall rate of microstructure growth is determined by the kinetics of the slowest step, i.e. swelling. Various chemical functions could be imparted to the microstructures by using functional monomers. It is worth mentioning that, unlike conventional light-triggered microstructure growth that is limited to the photoactive substrates, this force-triggered growth is, in principle, not limited to DN hydrogels but could be applied to different types of multiple-network polymeric materials.

## References

1. M. D. Bartlett, A. B. Croll, D. R. King, B. M. Paret, D. J. Irschick, and A. J. Crosby. Looking beyond fibrillar features to scale gecko-like adhesion. *Adv. Mater.* **24**, 1078−1083 (2012).
2. B. G. Munoz-Robles, I. Kopyeva, C. A. Deforest. Surface patterning of hydrogel biomaterials to probe and direct cell–matrix interactions. *Adv. Mater. Interfaces* **7**, 2001198 (2020).
3. Q. M. Wang, G. R. Gossweiler, S. L. Craig, and X. H. Zhao. Cephalopod-inspired design of electro-mechano-chemically responsive elastomers for on-demand fluorescent patterning. *Nat. Commun.* **5**, 4899 (2014).
4. T. Matsuda, R. Kawakami, R. Namba, T. Nakajima, and J. P. Gong. Mechanoresponsive self-growing hydrogels inspired by muscle training. *Science* **363**, 504−508 (2019).
5. J. Sohma. Mechanochemistry of polymers. *Prog. Polym. Sci.* **14**, 451−596 (1989).
6. Y. C. Simon, and S. L. Craig. *Mechanochemistry in Materials* Ch. 2 (Royal Society of Chemistry, 2017).
7. L. Bokobza. Near infrared spectroscopy. *J. Near Infrared Spectrosc.* **6**, 3−17 (1998).
8. L. A. Rodrı´guez-Guadarrama. Application of online near infrared spectroscopy to study the kinetics of anionic polymerization of butadiene. *Eur. Polym. J.* **43**, 928−937 (2007).
9. S. Beuermann, M. Buback, P. Hesse, T. Junkers, and I. Lacik. Free-radical polymerization kinetics of 2-acrylamido-2-methylpropanesulfonic acid in aqueous solution. *Macromolecules* **39**, 509−516 (2006).
10. D. Swinehart. The Beer-Lambert law. *J. Chem. Educ.* **39**, 333−335 (1962).
11. M. Buback, H. Hippler, J. Schweer, and H. Vogele. Time-resolved study of laser-induced high-

pressure ethylene polymerization. *Makromol. Chem. Rapid Commun.* **7**, 261−265 (1986).

12. V. P. Zubov, M. V. Kumar, M. N. Masterova, and V. A. Kabanov. Reactivity of allyl monomers in radical polymerization. *J. Macromol. Sci. Chem.* **13**, 111−131 (1979).
13. K. Matyjaszewski, T. P. Davis. *Handbook of Radical Polymerization* Ch. 1 (John Wiley & Sons. Press, 2003).
14. M. K. Beyer. The mechanical strength of a covalent bond calculated by density functional theory. *J. Chem. Phys.* **112**, 7307−7312 (2000).
15. P. C. Hiemenz, T. P. Lodge. *Polymer Chemistry* Ch. 3 (CRC. Press, 2007).

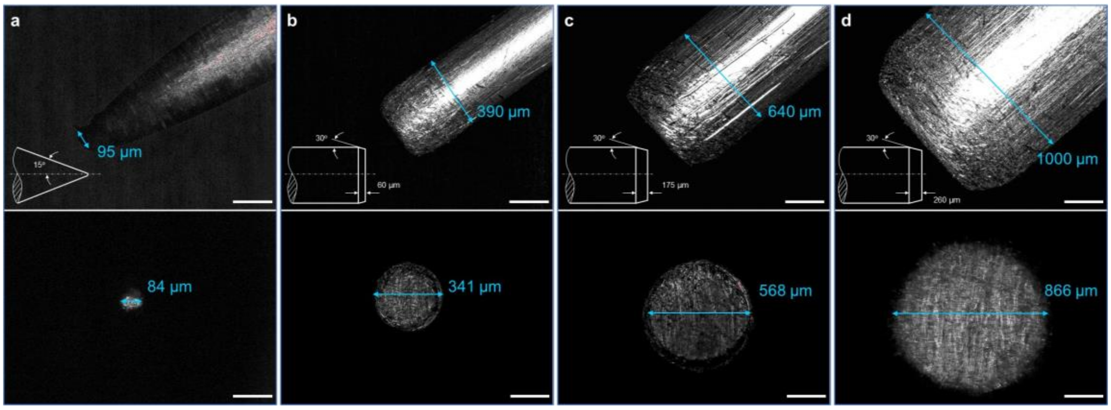

**Figure 5-1**. **a-d**. Microscope images of the cylindrical steel indenters with different diameters. The side view of the indenters (upper row). Insets, schematic diagram of engineering drawing for the cylindrical steel indenters. The bottom view of indenters (lower row). Scale bars, 200 µm.

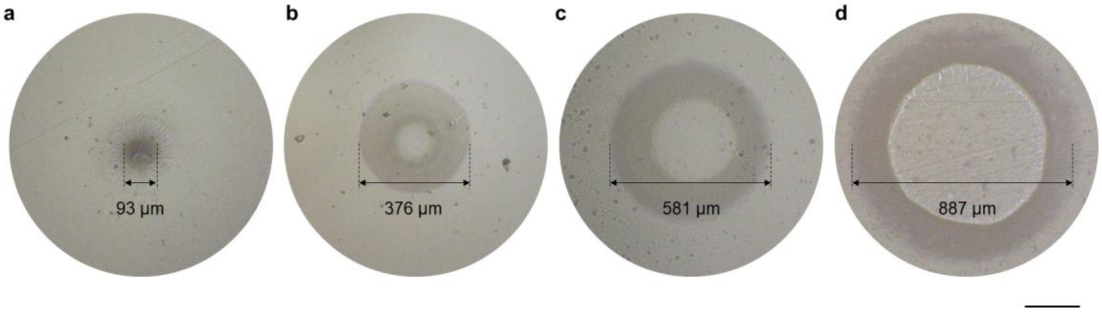

**Figure 5-2**. **a-d.** Microscope images of the microstructures on DN hydrogel surfaces, which were indented with different cylindrical steel diameters. The scale and shape of microstructures depends on the indenters. The experiments were carried out in NIPAm aqueous solution (concentration of NIPAm was 1.0 M) under argon atmosphere. The indenter diameters were 84, 341, 568, and 866 µm for a, b, c, and d, respectively. The indentation depth $L_{\max}$ was 1000 µm. Scale bar, 200 µm.

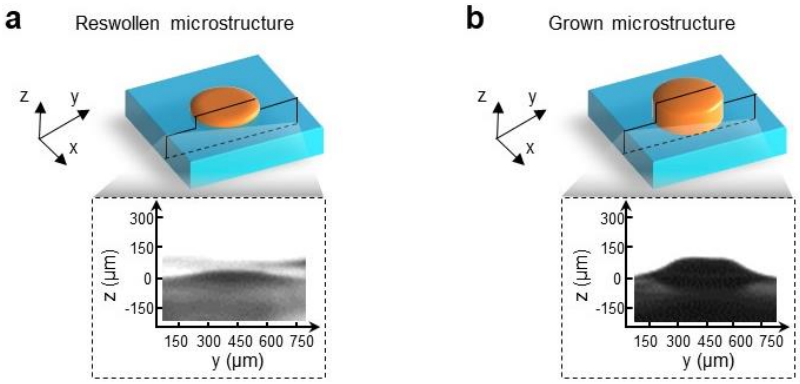

**Figure 5-3**. **a.** Schematic illustration and microscopic image of the reswollen microstructure on DN hydrogel surface. **b**. Schematic illustration and microscopic image of the grown microstructure induced by force-triggered radical polymerization.

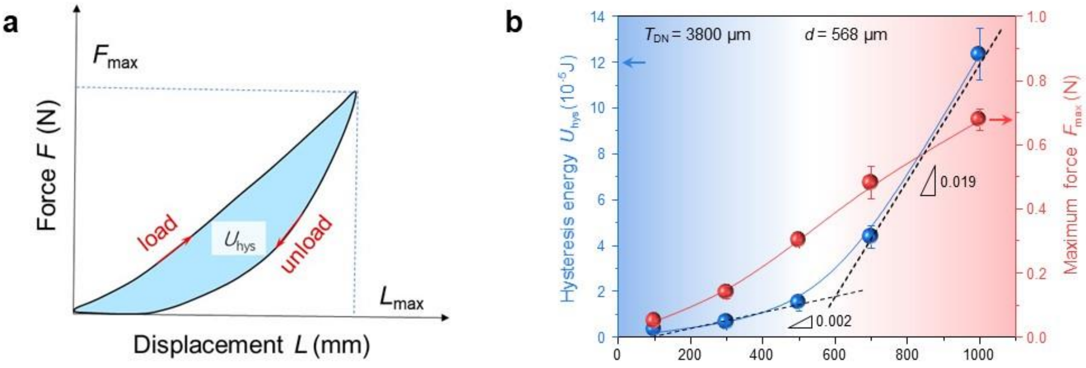

**Figure 5-4**. **a.** Quantification of the mechanical energy dissipated by cyclic indentation on tough DN hydrogel surfaces using a cylindrical steel indenter. The area beneath the force-displacement curve gives the work done by mechanical force to the DN hydrogel surfaces. **b**. The hysteresis energy $U_{\text{hys}}$ and maximum force $F_{\max}$ measured at various indentation displacements $L_{\max}$ by mechanical indentation without monomer supply in the air (a cylindrical steel indenter diameter was $d$ = 568 μm, the velocity of indentation was 1 mm min$^{-1}$, DN hydrogel thickness was ~3.8 mm). Error bar represents the standard deviation for three replicates. Some error bars in **b** are hidden by the symbols. Data in **b** are presented as mean values +/- standard deviation (SD).

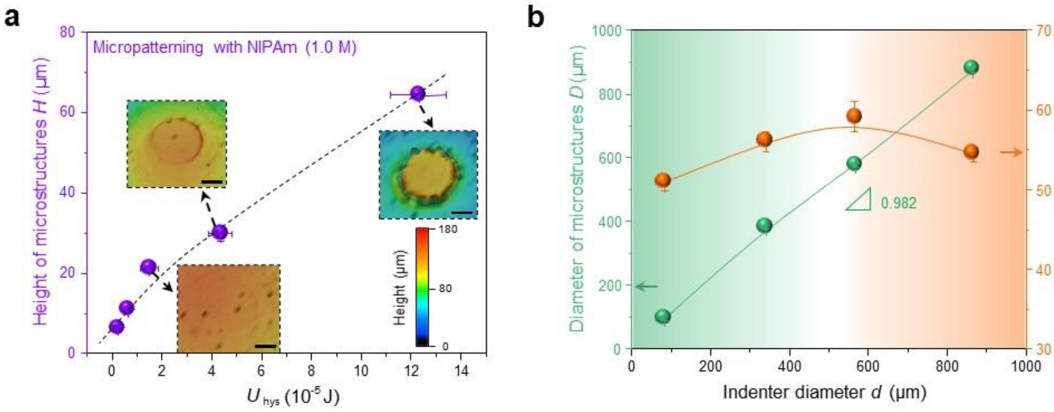

**Figure 5-5**. **a.** Dependence of the topographical height of microstructures on the mechanical hysteresis energy $U_{\mathrm{hys}}$. Scale bars, 200 μm. **b**. Topographical diameter and height of microstructures versus indenter diameter *d* for micropatterning with NIPAm on DN hydrogel surfaces ($L_{\max} = 1000$ μm). Error bar represents the standard deviation for three replicates. Some error bars in **a** and **b** are hidden by the symbols. Data in **a** and **b** are presented as mean values +/- standard deviation (SD).

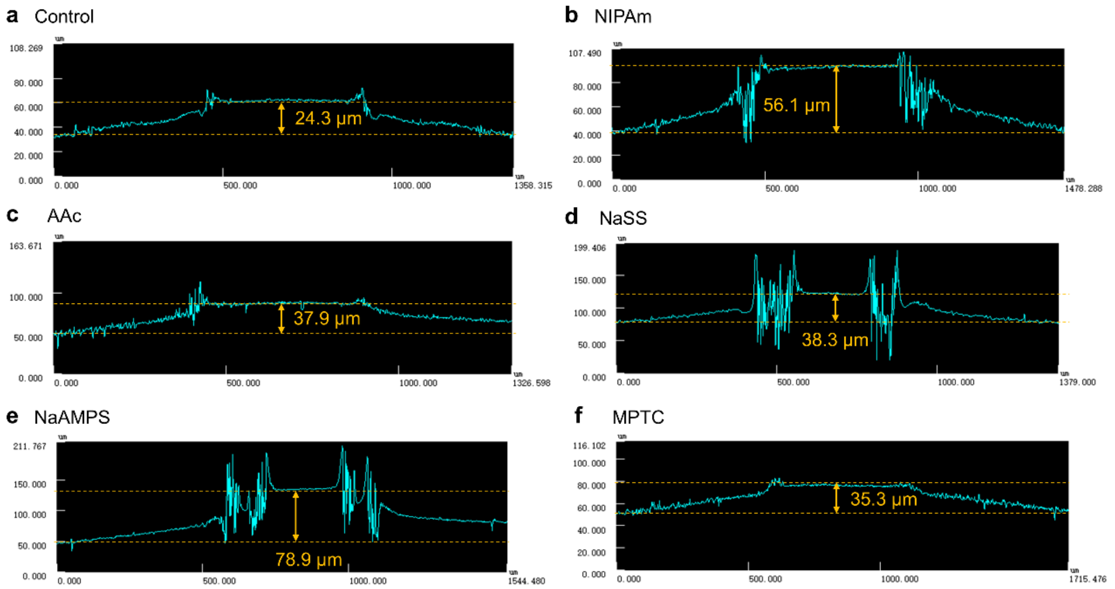

**Figure 5-6. a-f.** The typical profiles of the microstructures on DN hydrogel surfaces using different functional monomers, the control sample was prepared in pure water without monomer and crosslinker supply. Monomer concentration was 1.0 M without crosslinker for all cases except for the control.

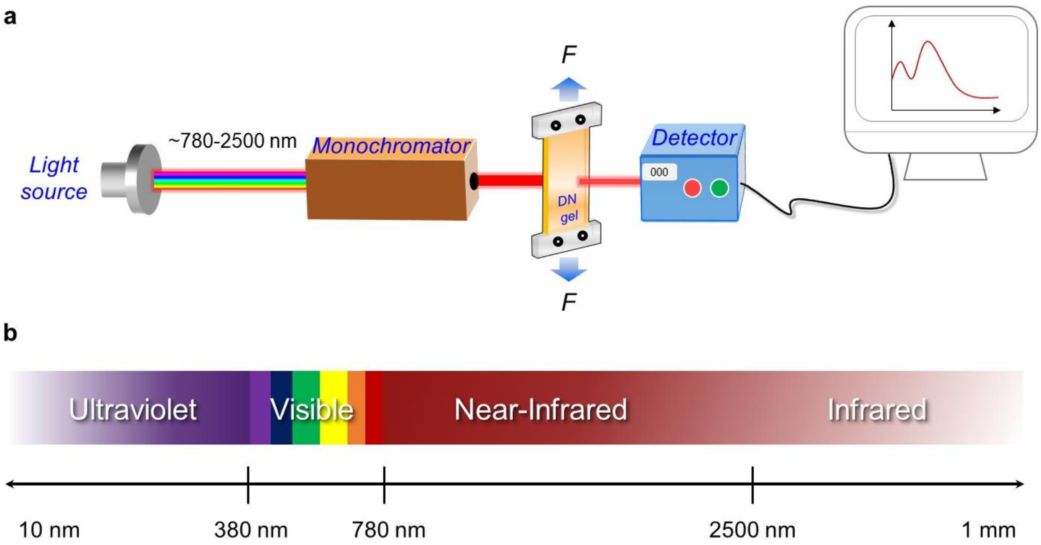

**Figure 5-7. a.** Schematic of an in-situ transmission FT-NIR spectroscopy, DN hydrogels fed with monomers and crosslinker were stretched to the necking strain in an argon atmosphere (*l* is the original thickness, sample thickness change is not considered in the mechanical stretching). **b**. Light spectrum regions, the near-infrared light region is selected to detect monomer concentration.

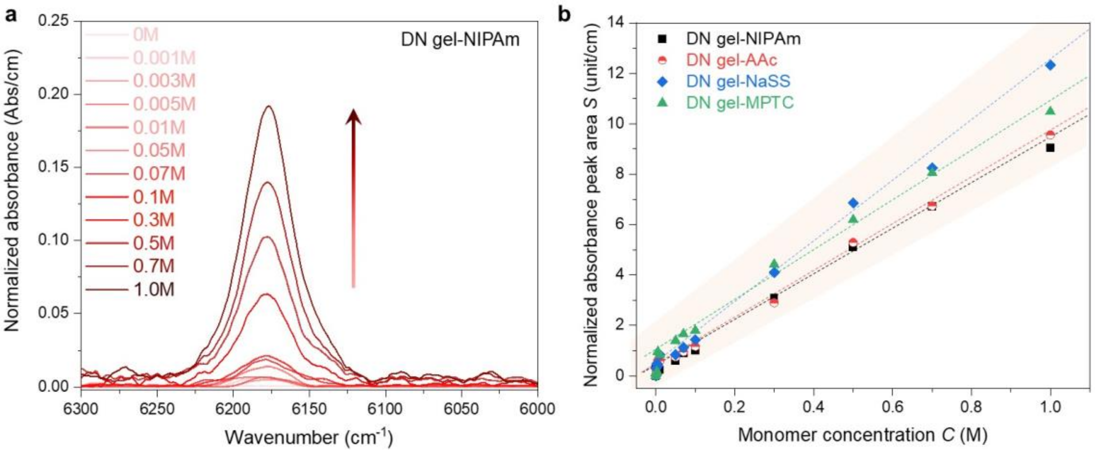

**Figure 5-8. a**. Transmission near-infrared spectrum of DN hydrogels fed with different monomer concentrations (NIPAm, 0 M-1.0 M). **b**. Calibration curves of DN hydrogels fed with different monomers.

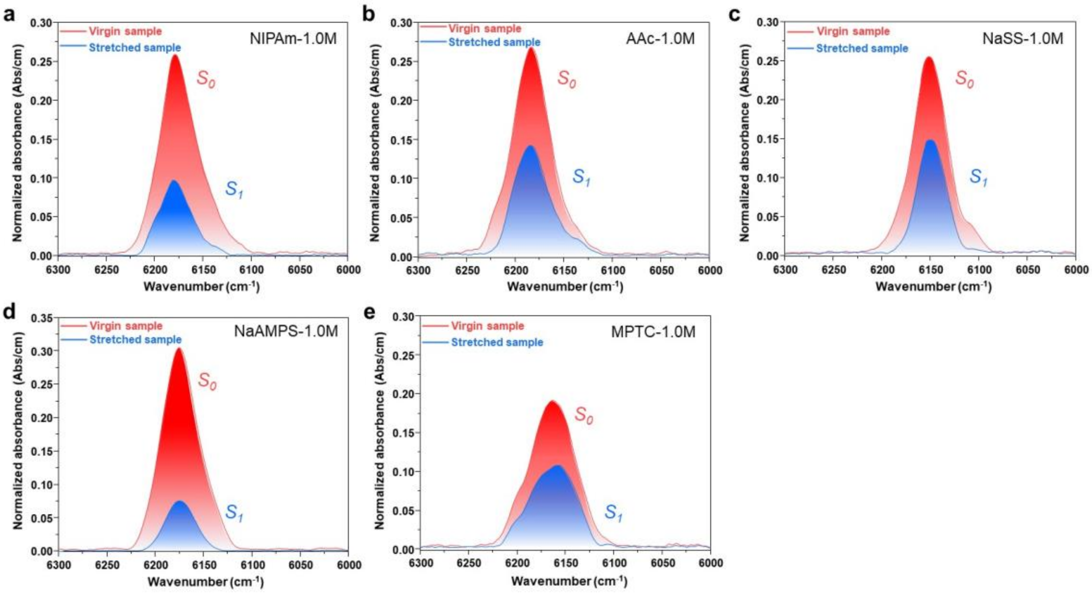

**Figure 5-9.** Transmission near-infrared spectra of DN hydrogel fed with different monomers before stretching ($S_0$) and after stretching ($S_1$), measurement waiting time was 1 min. **a**. NIPAm-1.0M (initial concentration was 1.0 M). **b**. AAc-1.0M. **c**. NaSS-1.0M. **d**. NaAMPS-1.0M. **e**. MPTC-1.0M. Crosslinker *N,N′*-methylenebisacrylamide (MBA) was not fed in this experiments.

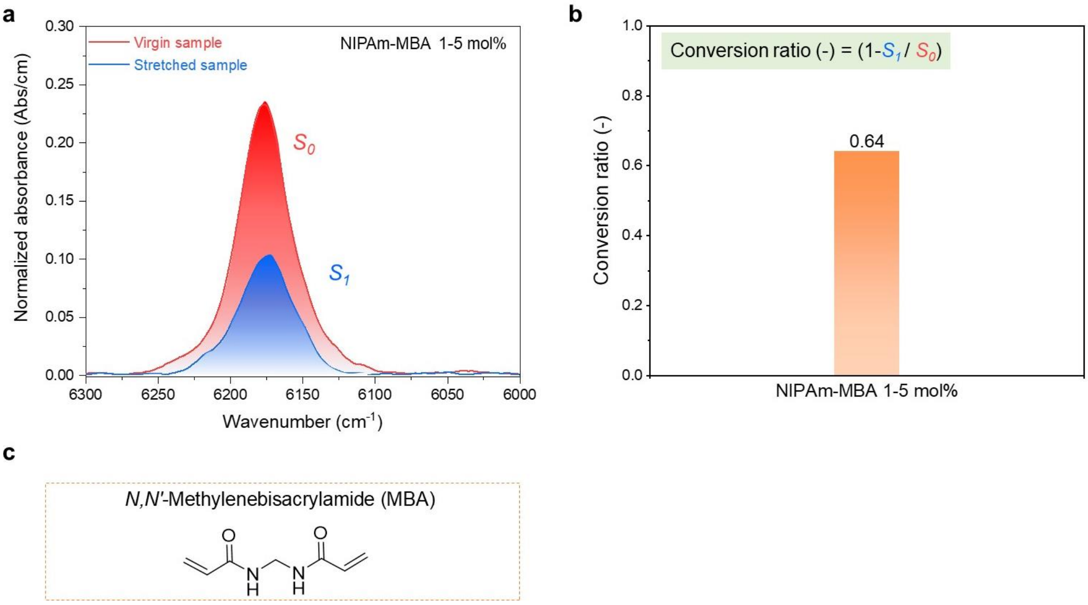

**Figure 5-10. a.** Transmission near-infrared spectra of DN hydrogel fed with NIPAm monomer and crosslinker MBA before stretching (peak area, $S_0$) and after stretching (peak area, $S_1$), measurement waiting time was 1 min. NIPAm monomer concentration was 1.0 M, the molar ratio of crosslinker MBA respect to NIPAm monomer was 5 mol%. **b**. The conversion ratio for DN hydrogels fed with NIPAm and MBA. Here, conversion ratio was calculated based on the inset equation. **c**. Molecular structure of *N,N′*-methylenebisacrylamide (MBA).

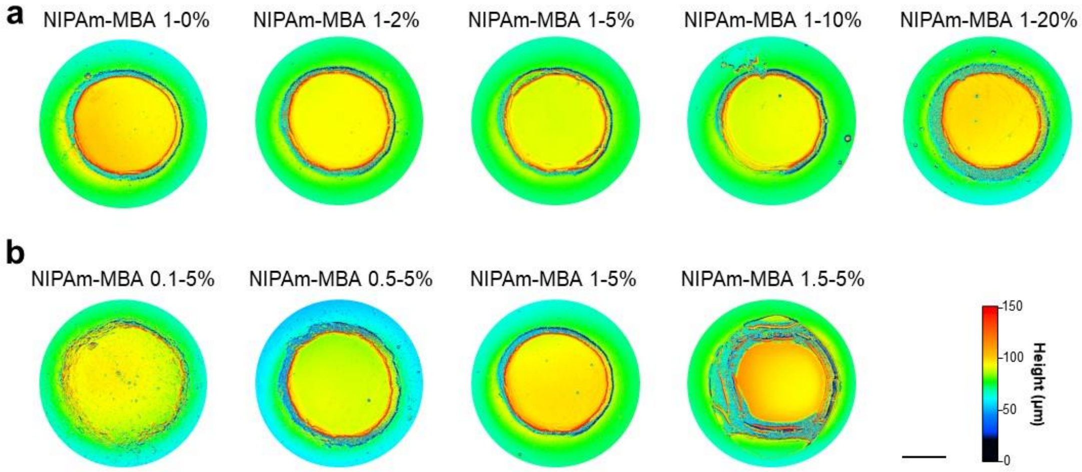

**Figure 5-11. a**. Three-dimensional laser microscopy observation of the microstructures using different crosslinker concentrations (sample NIPAm-MBA 1-0% indicates that the monomer NIPAm concentration was 1.0 M and crosslinker MBA concentration was 0 M). **b**. Three-dimensional laser microscopy observation of the microstructures using different monomer concentrations. Scale bar, 200 μm.

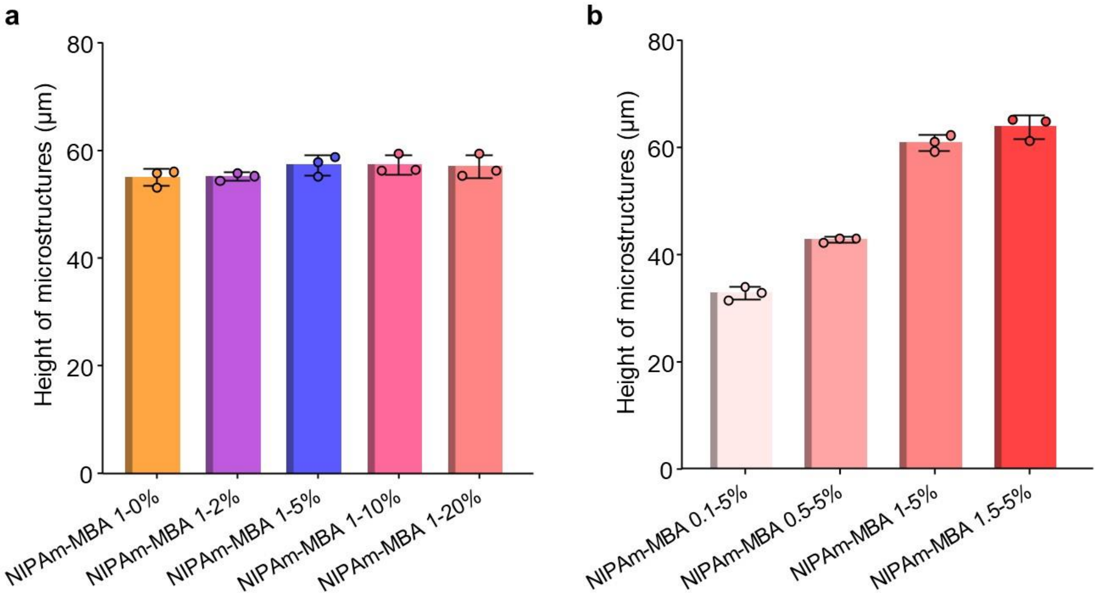

**Figure 5-12. a**. The height of microstructures using different crosslinker ratios (Here, the percentage was molar percentage). **b**. The height of microstructures using different monomer concentrations. The experiments were performed at 25 $^{o}$C. Error bar represents the standard deviation for three replicates. The circular dots of the histogram in **a** and **b** represent the measured data points of three. Data in **a** and **b** are presented as mean values +/- standard deviation (SD).

**a** Instantaneous patterning in NIPAm aqueous solution

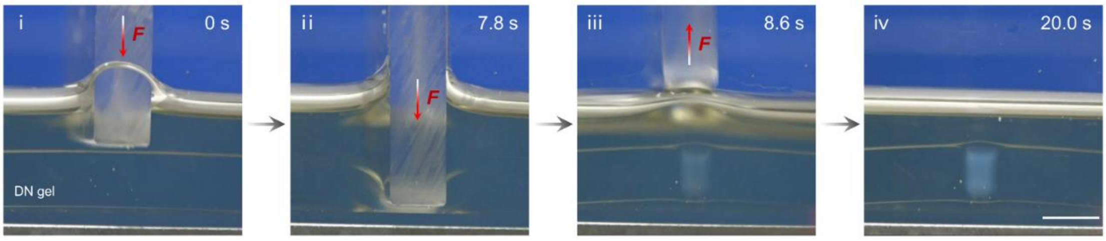

**b** Mechanical indentation in water (control)

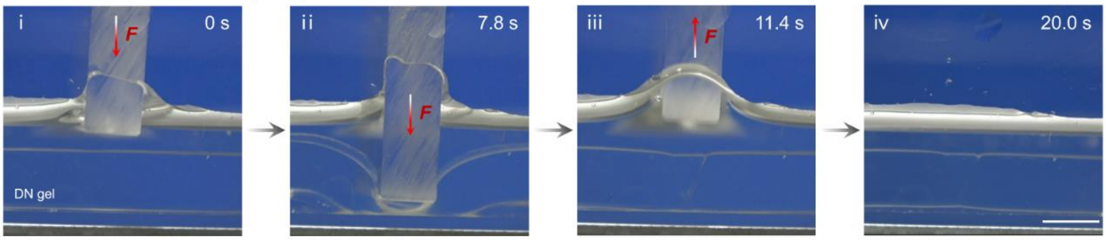

**Figure 5-13.** Time sequential snapshots to show rapid patterning triggered by mechanical force. **a**. Patterning in monomer aqueous solution (Here, concentration of NIPAm was 1.5 M). **b**. In deionized water without a mechanochemically prepared patterns. Scale bars, 5 mm.

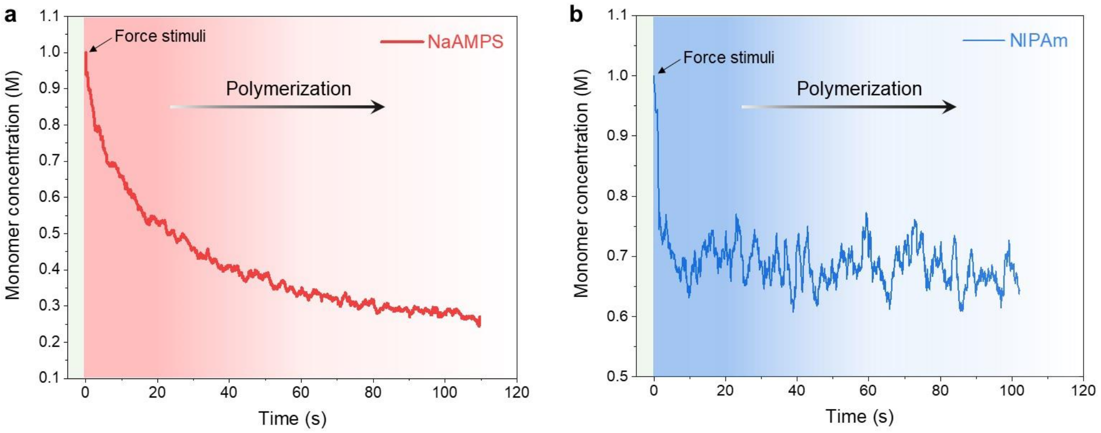

**Figure 5-14.** Kinetics of the force-triggered radical polymerization. The time-resolved near-infrared spectroscopy revealed that the force-triggered radical polymerization almost completed within tens of seconds. **a**. Time-resolved concentration of NaAMPS versus time. **b.** Time-resolved concentration of NIPAm versus time. The initial monomer concentration for NaAMPS and NIPAm was 1.0 M, the temperature was 25 °C. DN hydrogels fed with monomers were stretched beyond yielding point under argon atmosphere, tensile stress was ~0.9 MPa. Here, the curves of time-resolved near-infrared spectroscopy were the average value of at least two replicates.

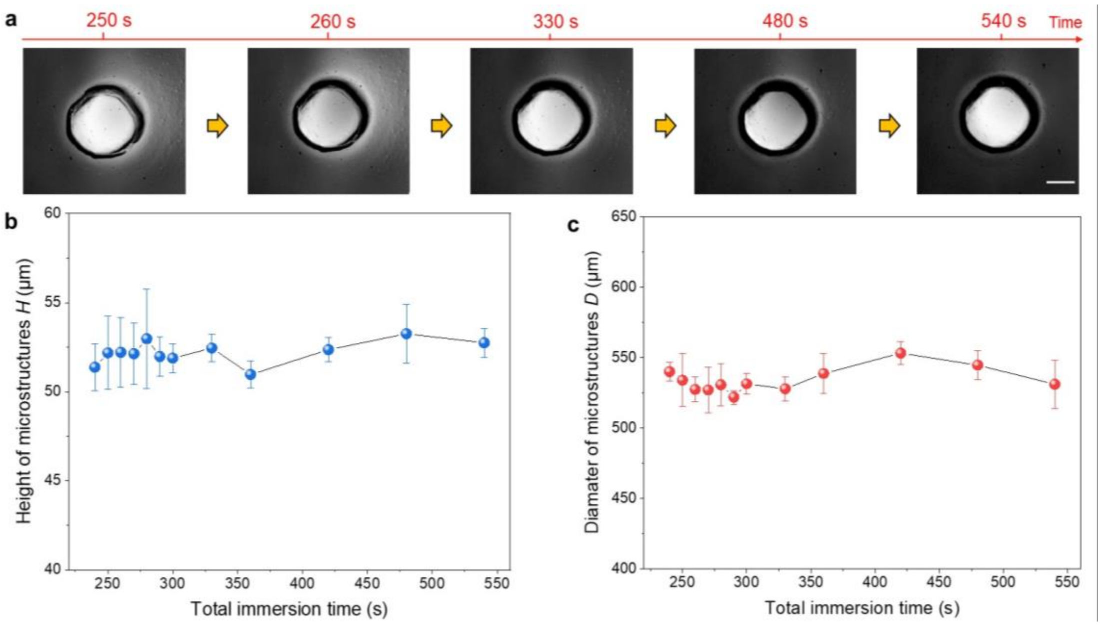

**Figure 5-15.** Evolution of microstructures on DN hydrogel surface in monomer aqueous solution. The microstructures were created by regioselective indentation under NIPAm aqueous solution (cylindrical steel indenter diameter was ~568 μm, displacement was ~1000 μm, indentation speed was 10 mm min$^{-1}$, the concentration of NIPAm was 1.0 M). **a**. Microstructure morphology changed over immersion time. **b**. Height of microstructures changed over immersion time. **c**. Diameter of microstructures changed over immersion time. The height *H* and diameter *D* of a microstructure on DN hydrogel surface for different total immersion times *t* were characterized as follows. First, a DN hydrogel was indented under the monomer solution in the glove box. The indented gel in the solution was immediately taken out from the glove box, then the gel was observed by the microscope in air after wiping the solution on the hydrogel surface by clean tissues. The time between the end of the indentation and the first microscope observation was 4 min (because of physical distance from the glove box to the microscope), during which the hydrogel was kept in the solution. Hence, we assumed the immersion time *t* of 240 s for the first observation. After the first observation, the hydrogel was immersed again in the solution for 10 s, picked up from solution and wiped by clean tissues, then observed by the microscope in air (total immersion time $t$ = 240 +10 = 250 s). Such step of immersion and observation was repeated several times for this DN hydrogel surface, resulting in *H* and *D* as a function of *t* up to 540 s. The results show that the micropatterning was finished before the first observation at $t$ = 240 s. Error bars represent the standard deviation from three replicates. Data in b and c are presented as mean values +/- standard deviation (SD). Scale bar, 200 μm.

# Chapter 6: Specific Applications of the Micropatterned Hydrogels

## 6.1. Introduction

Since the birth of synthetic polymer gels or hydrogels in the 1960s, research on this kind of fascinating soft material has progressed rapidly. Hydrogels are three-dimensional hydrophilic polymer networks swollen by water molecules, which show solid properties in a macroscopic view but present liquid-like behavior in a microcosm. Owing to their unique integration of elasticity, low friction, permeability to small molecules, and biocompatibility, hydrogels are extensively explored and widely used in diverse applications, such as cartilage, contact lenses, drug delivery vehicles, and biological tissue engineering[1-5]. By tuning the polymer chemistry, degree of cross-linking (modulus or stiffness), and solvent properties, hydrogels are often used for a wide range of biomedical engineering applications. The chemical and physical structures on the hydrogel surface are important for practical use, especially for tough double-network (DN) hydrogels that have promising applications as structural biomaterials[6-8]. At the same time, various biophysical, biochemical, and biological cues of material surfaces have been known to regulate cell differentiation, cell adhesion[9-11]. In nature, the nano- or micropatterns could be used for regulating surface wettability and water droplet directional movement owing to the anisotropic distribution of physical or chemical patterns on plant surfaces[12-15]. However, the various charming micropatterns on tough hydrogel surface have proven to be challenging owing to the two main reasons: 1) the rigid and easily brittle nature of the highly pre-stretched first networks can lead to the failure of moulding; 2) there is a layer of polyacrylamide (PAAm, thickness: 1−10 μm) without chemical modification sites on the normal DN hydrogel surfaces. Furthermore, the potential biomimetic applications of the micropatterned DN hydrogel have rarely been studied in previous works.

In this chapter, we created various complex physical and/or chemical micropatterns on DN hydrogel surfaces by the force-triggered rapid microstructure growth, and we mainly focused on the specific applications and underlying mechanisms of the micropatterned DN hydrogels for cell culture and water droplet control. The results reveal that the micropatterned DN hydrogels could be used not only for directed growth and enhanced myogenesis of muscle cell but also for water droplet directional transport. We envision that our force-triggered rapid microstructure growth strategy and the micropatterned hydrogels hold promise for biomedical engineering.

## 6.2. Experiments

### 6.2.1 Materials

Deionized water ($H_2O$) used was purified by a lab water purification system (Merck KGaA, Darmstadt, Germany). Acrylamide (AAm) was purchased from Junsei Chemical, 2-Acrylamido-2-methylpropanesulfonic acid sodium salt (NaAMPS) (49.7 wt % aqueous solution) was provided by Toa Gosei. *N,N′*-Methylenebisacrylamide (MBA), *N*-isopropylacrylamide (NIPAm), 8-anilino-1-naphthalenesulfonic acid (ANS), and 2-oxoglutaric acid (α-keto) were purchased from Fujifilm Wako Pure Chemical Corporation. Soda-lime glass plates and silicon rubbers were purchased from As One Corporation. The mouse myoblast cell line C2C12, labelled with a green fluorescence protein (GFP), was kindly provided by S. Kohsaka. Self-prepared Dulbecco's modified Eagle's medium containing 10% foetal bovine serum and 1% penicillin/streptomycin was used for cell culture. Homemade phosphate buffered saline (PBS) was used for washing. Bovine serum albumin (BSA), and the myoblast determination protein (MyoD (G-1)) and 4`,6-diamidino-2-phenylindole, dihydrochloride (DAPI) were purchased from Thermo Fisher Scientific.

### 6.2.2 Programmable patterning on hydrogel surfaces

Firstly, the complex patterned indenters were printed using a commercially available high-precision three-dimensional (3D) printer system (Agilista 3100, Keyence Co., Ltd.). The surface patterns of indenters were designed by a commercial software Solidworks (Dassault Systèmes SolidWorks Corporation, USA) prior to the course of 3D printing. The surface quality of 3D printed indenter was defined as glossy surface. The material of 3D printed indenters was high strength resin. The topographic height of the printed patterns was ~2 mm, photos of 3D printed indenters are shown in **Figure 6-1**. The rapid micropatterning on hydrogel surface (DN-Si-PET-0.8kPa) was performed in an argon glove box using a mechanical tester (MCT-2150, A&D Co., Ltd.). Herein, the micropatterns of "G E L" were shown in **Figure 6-2**. The 3D printed indenters were fixed on a home-made metal holder, and the holder with indenters was fixed on the sensor of a small tensile machine (MCT-2150, A&D Co., Ltd.) using a screw. The DN hydrogels were immersed in the mixed aqueous solution of NIPAm and ANS (NIPAm: 1.0 M, ANS: 0.3 mM) for overnight. The immersed DN hydrogels were fixed on a rigid glass plate by super glue, then they were moved to an argon glove box to remove oxygen. The complex patterns were created by indenting selectively on DN hydrogel surfaces under the solution using the 3D printed indenters. The indentation depth was ~1 mm for the preparation of the complex patterns. The convex array structures were prepared by a homemade metal indenter (**Figure 6-3**). The parallel patterns were prepared using the stacked metal blades, the distance between which was controlled using a silicone rubber spacer (**Figure 6-4)**.

### 6.2.3 Observation of the micropatterned hydrogel surfaces

First, we directly observed the microstructures on DN hydrogel surfaces by three-dimensional (3D) laser microscope, the morphology and size of microstructures can be clearly quantified. We created various thermo-responsive poly(*N*-isopropylacrylamide) (PNIPAm) patterns on DN hydrogel surfaces, and used a fluorescent molecular probe, 8-anilino-1-naphthalenesulfonic acid (ANS), which emits a strong fluorescence signal in hydrophobic environments, to image the complex patterns on hydrogel surfaces (**Figure 6-5**). The DN hydrogels with the grown patterns were immediately observed at high temperatures (50 °C) and ultraviolet light (UV, wavenumber is ~365 nm) irradiation after the mechanical indentation. **Figure 6-6** shows various fluorescent patterns on DN hydrogel surfaces prepared using the force-triggered programmable patterning. In addition, a bamboo-knot-like pattern and parallel stripe pattern in the hydrogel bulk were also prepared using the regioselective mechanical indentation. These images were taken by an optical camera (Canon, EOS 7D) under UV irradiation.

### 6.2.4 Cell culture on the micropatterned hydrogel surfaces

The mouse myoblast cell line C2C12, labelled with a green fluorescence protein (GFP), were utilized to study the effects of patterned substrates on cell morphology and adhesion. The cells were cultured in Dulbecco's modified Eagle's medium containing 10% foetal bovine serum and 1% penicillin/streptomycin at 37 °C in a humidified atmosphere containing 5% $CO_2$. The 4–7th passages of the C2C12 cells were used in this study. After steam sterilization, the patterned DN hydrogel disk was placed in a 6-well polystyrene tissue culture dish, and the C2C12 cells were seeded on the patterned DN hydrogel surfaces at an initial cell density of $1\times10^5$/mL. A cell dispersion solution was applied onto the hydrogel surface in a dropwise manner to produce a relatively uniform distribution of cells on the hydrogel surface. All cell-loaded hydrogel samples were cultured at 37 °C in a humidified atmosphere containing 5% $CO_2$. The samples were transferred to new wells for observation under a fluorescence microscope. The cell morphology and proliferation on the patterned DN hydrogel surface were monitored using an Olympus IX 71 fluorescence microscope (Olympus, Japan) equipped with a digital CCD camera with a lens (magnification of 10 and 20).

### 6.2.5 Immunocytochemistry staining

The muscle cells cultured for 7 days in the media were fixed with 3 wt% paraformaldehyde (PFA) solution for 15 min, treated with 0.1% v/v Triton X-100 for 4 min to make the cell membrane permeable, and incubated in the blocking solution (1 wt% BSA in PBS) for 20 min. For each step, the samples were washed three times with phosphate buffered saline (PBS). The samples were incubated overnight at 4 °C with a mouse monoclonal antibody (Alexa fluor 488-labeled MYH (sc-376157), Santa Cruz) at a 1:1000 dilution in PBS, and the MyoD protein was stained with MyoD antibody, the nuclei were stained with 0.1% v/v DAPI for 10 min. The washing steps using PBS were included between each staining step. The fluorescence images were obtained with a fluorescence microscope (Olympus IX 71 (Olympus, Japan)). The obtained images were analyzed using the ImageJ software (National Institutes of Health, Bethesda, MD). The cellular orientations of C2C12 myoblasts or myotubes were quantitatively analyzed to determine the angle between the pattern direction and the longest axis of the cells. The aspect ratio of myoblasts, defined as the ratio between the body length of the longest axis and that of the shortest axis across the nuclei, was also analyzed.

### 6.2.6 Quantitative real time PCR (qRT-PCR)

Total ribonucleic acid (RNA) was isolated from myoblast C2C12 using a RNeasy Mini Kit (Qiagen, Valencia, CA) according to the manufacturer’s protocols and reverse transcribed into cDNA using the SuperScript® VILO™ cDNA Synthesis Kit (Invitrogen, Carlsbad, CA). The relative expression levels of RNA were normalized to glyceraldehyde-3-phosphate dehydrogenase (GAPDH). qRT-PCR samples were prepared with the same amount of cDNA, Power SYBR green PCR master mix, and the following primers: GAPDH (forward: 5′-AGC CAC ATC GCT CAG ACA C-3′, reverse: 5′-GCC CAA TAC GAC CAA ATC C-3′); MyoD (forward: 5′-GCC TGA GCA AAG TGA ATG AG-

3′, reverse: 5′-GCA GAC CTT CGA TGT AGC G-3′); MHC (forward: 5′-AGC AGA CGG AGA GGA GCA GGA AG-3′, reverse: 5′-CTT CAG CTC CTC CGC CAT CAT G-3′); Myf5 (forward: 5′-CCT GTC TGG TCC CGA AAG AAC-3′, reverse: 5′-GAC GTG ATT CGA TCC ACA AT G-3′). qRT-PCR was performed using StepOnePlus™ Real-Time PCR System (Applied Biosystems, Waltham, MA) using Power SYBR® Green Master Mix (Invitrogen).

### 6.2.7 Time-lapse imaging

A set of two-dimensional (2D) time-series images from muscle cells obtained using wide-field microscopy. Detection and tracking of cell clusters in time-lapse microscopy images were carried out in a humidified incubator (37 ºC, 5% $CO_2$) for two days. Buffer solutions containing pH stabilizer were used.

### 6.2.8 Water contact angle of the micropatterned hydrogel surfaces

Liquid contact angle of the patterned DN hydrogels was measured by using a Drop master 300 (Kyowa Interface Science Co., Ltd.) in air at 25 ºC. For the static contact angle measurements, liquid volume was 10 μL for water droplet, free water on hydrogel surfaces was wiped off using cleaning tissues prior to each measurement, waiting time was 5 s for each measurement. The dynamic contact angle measurements were also carried out using the same machine, liquid droplet (10 μL) was extruded with a pipette. The contact angle was the average value of three measurements.

### 6.2.9 Water droplet directional transport

Droplets of deionised water of different volume (2–25 μL) were used for the directional transport experiments. The water droplets were dyed with methylene blue prior to using. The dyed water droplets were deposited using a micropipette. As soon as each droplet contacted the hydrogel surface, the droplet dynamics on the hydrogel surface was monitored using a commercially available camera (Canon, EOS 7D). The relative humidity was maintained at approximately 30%, and the room temperature was maintained at 25 °C.

## 6.3. Results and discussion

### 6.3.1 Stimuli-responsive fluorescent patterns

Fluorescence images represent various complex PNIPAm-patterns on DN hydrogel surfaces. In addition, bamboo knot-like pattern and parallel stripe pattern can be programmatically created in

DN hydrogel bulks (**Figure 6-6**). Here, the PNIPAm-patterned DN hydrogels can emit fluorescence signal reversibly once stimulated by high temperature (above the low critical solution temperature of PNIPAm, 32 °C) and ultraviolet light (UV, wavenumber is ~365 nm). The mechanism of fluorescence emission of the PNIPAm-patterned DN hydrogel is shown in **Figure 6-5**[16,17]. The fluorescence intensity can be changed with temperatures, the quantitative data shows this obvious dependence of fluorescence intensity with external temperature (**Figure 6-7**). The increase in chain entanglement of PNIPAm induces more hydrophobic regions in the clusters of polymer chains at high temperature. The increase of hydrophobic regions or hydrophobic intensity will significantly increase the fluorescence intensity of PNIPAm-patterned regions. Furthermore, the patterned hydrogel shows remarkable material properties including high toughness, extreme stretchability, and rapid elastic recovery. These superior material properties would lead to the potential use of patterned DN hydrogel as flexible display devices or smart sensors (**Figure 6-8**).

### 6.3.2 Cell adhesion

To demonstrate potential biological applications, we engineered topographies and chemistries on DN hydrogel surfaces to control cell adhesion and orientation (**Figure 6-9, Figure 6-10**). It is known that cell adhesion is a strict requirement for survival of cells, and it orchestrates critical roles in many cellular functions including migration, proliferation, differentiation, and apoptosis[18]. In fact, cell prefers to adhere on the hydrophobic surface rather than hydrophilic surface, this is because the hydration layer on hydrophilic surface prevents cells from adhering to the substrate. The aggregated cell clusters indicate that weak or no adhesion between cells and the pure single-network hydrogel surfaces (**Figure 6-11**). However, the adherent and scattered cell morphology indicate that cell can adhere to the hydrophobic PNIPAm hydrogel surfaces at 37 °C (**Figure 6-11 c**). **Figure 6-12** shows the effect of chemistry on cell adhesion and orientation, we propose that the hydrophobic PNIPAm and PDMA patterns, and the charged PNaAMPS patterns can induce cell adhesion through hydrophobic and Coulomb interactions, respectively. In particular, the PNIPAm pattern surface is rougher than the DN hydrogel substrate, phase separation of PNIPAm may lead to the increase in surface roughness (**Figure 6-15**). We propose that the rough surface is more favorable for cell adhesion due to the topological adhesion (**Figure 6-16**). In order to exclude the influence of the microenvironment on cell adhesion, we prepared different patterns with different monomers on one hydrogel surface. The results show that cell prefers to adhere to the hydrophobic patterns selectively (**Figure 6-17**). So, we can foresee that our microstructures process potential applications in cell screening.

### 6.3.3 Single cell elongation

The alignment and complex hydrophobic patterns can induce cell adhesion and forming cell patterns (**Figure 6-18**). Zooming in **Figure 6-18 c** clearly shows the elongation of individual cell. The aligned hydrophobic PNIPAm domains on the DN hydrogels induced cell aggregation and orientation through hydrophobic interactions with cells[19]. Topographical contact guidance was derived from an orchestrated interplay between the extracellular matrix, biophysical cues, and cell recognition sites that affect their decision[20-22].

The PNIPAm pattern can induce single cell elongation, aspect ratio of single cell elongation is 10, which is bigger than that of control samples (**Figure 6-19**). The cell nucleus is also elongated on the PNIPAm pattern (**Figure 6-20**). Our results show that PNIPAm is more beneficial to cell proliferation than DN hydrogel substrate (**Figure 6-21**). The guide of this topographical structure can be confirmed by time-lapse observation (**Figure 6-22**).

### 6.3.4 Enhanced myogenesis

The PNIPAm pattern was shown to support myoblast cell (named C2C12) adhesion and elongation. The aligned engineered surfaces have been proved to promote skeletal muscle cell morphogenesis and aligned myotube formation in early research[23-25]. The gene expression analysis results confirm that the PNIPAm pattern enhanced the myogenesis of myoblast cell (**Figure 6-23**).

### 6.3.5 Water droplet directional transport on patterned DN hydrogel surfaces

Next, we show that the anisotropic DN hydrogel surfaces with parallel PNIPAm patterns can be used for regulating surface wettability and water droplet directional transportation. The static water contact angle shows lower contact angle on PNIPAm patterned hydrogel surfaces (**Figure 6-24**). We speculate that the rough PNIPAm pattern has a diversion effect on the water droplet, which results in a smaller contact angle. The control experiments show that water droplet can flow automatically along the pattern direction in the horizontal direction (**Figure 6-25**). In this case, the driving force of the droplet movement may be the enhanced capillary force of the rough surface of

PNIPAm pattern.

When a droplet is placed on a vertically placed surface, whether it stays stationary or moves depends on the competition of wetting asymmetry of the droplet on the surface and gravity on the droplet (**Figure 6-26**). The resistance against sliding increases with the difference between the receding angle ($\theta_{Res}$) and advancing angle ($\theta_{Adv}$) of the droplet on a solid surface, while the driving force (i.e. gravity) for droplet sliding, increases with the droplet size. As shown in **Figure 6-27**, the difference of receding angle and advancing angle of a water droplet (10 μL) on the surface of DN hydrogel with parallel PNIPAm lines aligned in vertical direction is 15°, which is only half of that on the surface of DN hydrogel with PNIPAm lines aligned in horizontal direction or on a smooth DN hydrogel surface. This result indicates that the micro-patterns can be used to regulate surface droplet transportation. In fact, the transport velocity is a linear function of water droplet volume on the patterned surface when the PNIPAm lines are set in vertical direction. However, there is a critical value around 10 μL for the droplet to move when the lines are set in horizontal direction, as like on the smooth surface. The experimental results demonstrate that the vertically patterned surface could induce faster water transport, and the transport velocity depends on the water droplet volume (**Figure 6-28**).

## 6.4. Summary

We successfully created various complex patterns on DN hydrogel surfaces by the regioselective mechanical indentation. The PNIPAm-patterned DN hydrogel surface shows reversible fluorescence emission using external stimuli of temperature and ultraviolet light. The PNIPAm pattern was proved to support muscle cell adhesion and proliferation. The rough and hydrophobic PNIPAm patterns induced cell adhesion through hydrophobic interactions and topological adhesion. The gene expression analysis results confirm that the PNIPAm pattern enhanced the myogenesis of muscle cell. The anisotropic DN hydrogel surfaces with parallel PNIPAm patterns can be used for regulating surface wettability and water droplet directional transportation. We thus envision that our rapid patterning strategy and micropatterned tough DN hydrogels hold promise for microsensor arrays, soft adhesion, flexible displays, and biomedical devices.

## References

1. F. C. Yang, J. C. Zhao, W. J. Koshut, J. Watt, J. C. Riboh, K. Gall, and B. J. Wiley. A synthetic

hydrogel composite with the mechanical behaviour and durability of cartilage. *Adv. Funct. Mater.* **30**, 2003451 (2020).

2. J. K. Xu, X. S. Li, and F. Q. Sun. Cyclodextrin-containing hydrogels for contact lenses as a platform for drug incorporation and release. *Acta Biomater.* **6**, 486−493 (2010).
3. T. R. Hoare, D. S. Kohane. Hydrogels in drug delivery: Progress and challenges. *Polymer* **49**, 1993−2007 (2008).
4. J. Kisiday, M. Jin, B. Kurz, H. Hung, C. Semino, S. Zhang, and A. J. Grodzinsky. Self-assembling peptide hydrogel fosters chondrocyte extracellular matrix production and cell division: Implications for cartilage tissue repair. *PNAS* **99**, 9996−10001 (2002).
5. Q. F. Mu, Q. S. Zhang, W. Yu, M. L. Su, Z. Y. Cai, K. P. Cui, Y. N. Ye, X. Y. Liu, L. L. Deng, B. J. Chen, N. Yang, L. Chen, L. Tao, and Y. Wei. Robust multiscale orientated thermoresponsive fibrous hydrogels with rapid self-recovery and ultra-fast response underwater. *ACS Appl. Mater. Interfaces* **12**, 33152−33162 (2020).
6. T. Nonoyama, J. P. Gong. Tough double network hydrogel and its biomedical applications. *Annu. Rev. Chem. Biomol. Eng*. **12**, 393−410 (2021).
7. M. A. Haque, T. Kurokawa, and J. P. Gong. Super tough double network hydrogels and their application as biomaterials. *Polymer* **53**, 1805−1822 (2012).
8. M. Frauenlob, D. R. King, H. L. Guo, S. Ishihara, M. Tsuda, T. Kurokawa, H. Haga, S. Tanaka, and J. P. Gong. Modulation and characterization of the double network hydrogel surface-bulk transition. *Macromolecules* **52**, 6704−6713 (2019).
9. C. J. Bettinger, R. Langer, and J. T. Borenstein. Engineering substrate topography at the micro- and nanoscale to control cell function. *Angew. Chem. Int. Edit.* **48**, 5406−5415 (2009).
10. B. G. Munoz-Robles, I. Kopyeva, and C. A. Deforest. Surface patterning of hydrogel biomaterials to probe and direct cell–matrix interactions. *Adv. Mater. Interfaces* **7**, 2001198 (2020).
11. M. Nikkhah, F. Edalat, S. Manoucheri, and A. Khademhosseini. Engineering microscale topographies to control the cell substrate interface. *Biomaterials* **33**, 5230−5246 (2012).
12. H. W. Chen, P. F. Zhang, L. W. Zhang, H. L. Liu, Y. Jiang, D. Y. Zhang, Z. W. Han, and L. Jiang. Continuous directional water transport on the peristome surface of Nepenthes alata. *Nature* **532**, 85−89 (2016).
13. Y. M. Zheng, H. Bai, Z. B. Huang, X. L. Tian, F. Q. Nie, Y. Zhao, J. Zhai, and L. Jiang. Directional water collection on wetted spider silk. *Nature* **463**, 640−643 (2010).
14. K. Chu, R. Xiao, and E. N. Wang. Uni-directional liquid spreading on asymmetric nanostructured surfaces. *Nat. Mater.* **9**, 413−417 (2010).
15. J. Ju, Y. M. Zheng, and L. Jiang. Bioinspired one-dimensional materials for directional liquid

transport. *Acc. Chem. Res.* **47**, 2342−2352 (2014).

16. T. Matsuda, R. Kawakami, T. Nakajima, and J. P. Gong. Crack tip field of a double-network gel: visualization of covalent bond scission through mechanoradical polymerization. *Macromolecules* **53**, 8787−8795 (2020).
17. L. N. Chen, C. Yan, and Z. J. Zheng. Functional polymer surfaces for controlling cell behaviors. *Mater. Today* **21**, 38−59 (2018).
18. J. A. Rowley, G. Madlambayan, and D. J. Mooney. Alginate hydrogels as synthetic extracellular matrix materials. *Biomaterials* **20**, 45−53 (1999).
19. L. Y. Wang, H. L. Liu, F. L. Zhang, G. N. Li, and S. T. Wang. Smart thin hydrogel coatings harnessing hydrophobicity and topography to capture and release cancer cells. *Small* **34**, 4697−4701 (2016).
20. C. J. Bettinger, R. Langer, and J. T. Borenstein. Engineering substrate topography at the micro- and nanoscale to control cell function. *Angew. Chem. Int. Edit.* **48**, 5406−5415 (2009).
21. Q. H. Wu, M. Maire, S. Lerouge, D. Therriault, and M. C. Heuzey. 3D printing of microstructured and stretchable chitosan hydrogel for guided cell growth. *Adv. Biosyst.* **1**, 1700058 (2017).
22. P. Lavrador, V. M. Gaspar, and J. F. Mano. Mechanochemical patternable ECM-mimetic hydrogels for programmed cell orientation. *Adv. Healthcare Mater.* **9**, 1901860 (2020).
23. A. Cooper, S. Jana, N. Bhattarai, and M. Q. Zhang. Aligned chitosan-based nanofibers for enhanced myogenesis. *J. Mater. Chem.* **20**, 8904−8911 (2010).
24. S. Jana, A. Cooper, and M. Q. Zhang. Chitosan scaffolds with unidirectional microtubular pores for large skeletal myotube generation. *Adv. Healthcare Mater.* **2**, 557−561 (2013).
25. S. H. Ku, C. B. Park. Combined effect of mussel-inspired surface modification and topographical cues on the behavior of skeletal myoblasts. *Adv. Healthcare Mater.* **2**, 1445−1450 (2013).

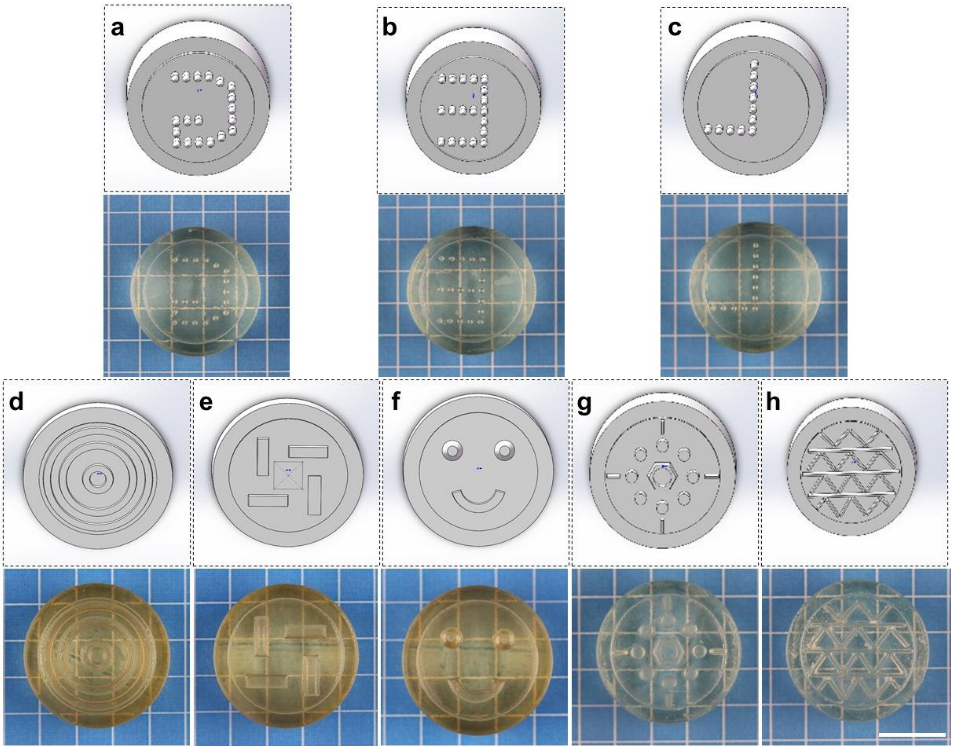

**Figure 6-1. a-h.** Photos of customized models with complex patterns for 3D printing and 3D printed resin indenters. The topographic height of all the 3D printed patterns was 2 mm. Scale bar, 10 mm.

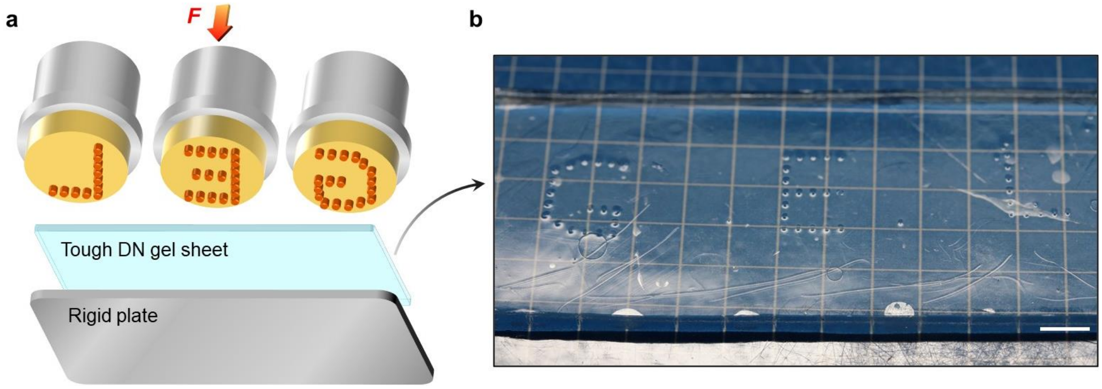

**Figure 6-2. a.** Schematic illustration for programmable micropatterning on DN hydrogel surface. **b**. DN hydrogel surface with the created alphabet of “G E L”. Patterning in NIPAm and MBA aqueous solution (NIPAm concentration was 1.0 M, crosslinker MBA concentration was 5 mol% of the monomer concentration). Scale bar, 5 mm.

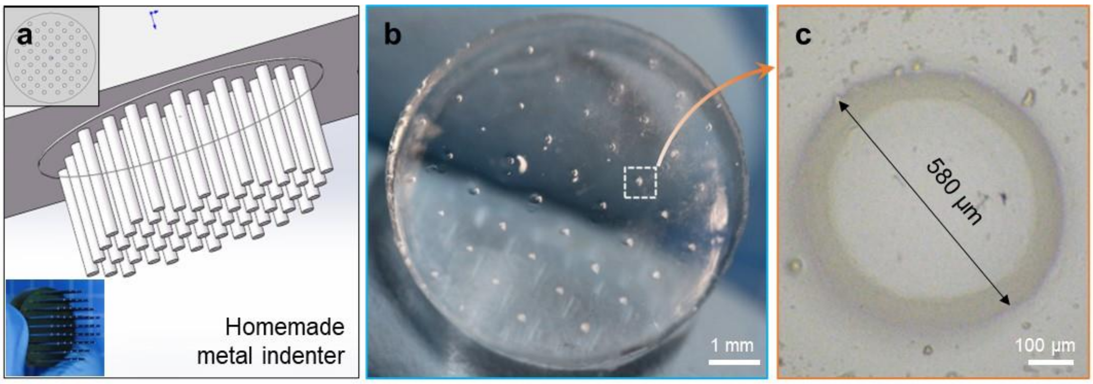

**Figure 6-3. a.** Schematic illustration and photo for the homemade metal indenter, the number of steel rod was 57. **b**. Photo for the PNIPAm-patterned DN hydrogel surface. **c**. Microscope image for one microstructure on DN hydrogel surface. NIPAm 1.0 M was used for **b** and **c**.

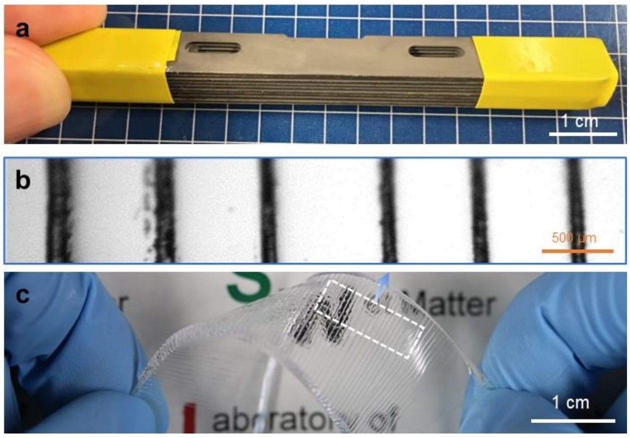

**Figure 6-4. a.** Photo for the homemade stacked metal blades, the distance between which was controlled using silicone rubber spacers (Here, the spacer thickness is 500 μm, the blade thickness is 113 μm). **b**. Microscope image for the parallel patterned hydrogel surface. **c**. Photo for the hydrogel with parallel patterns. NIPAm 1.0 M was used for **b** and **c**.

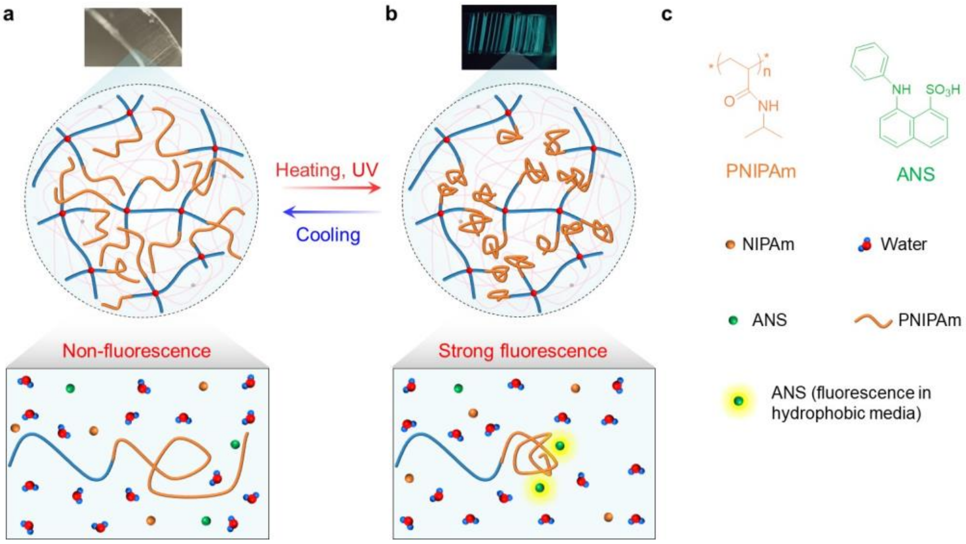

**Figure 6-5.** Molecular mechanism of fluorescence emission from the PNIPAm-patterned region on DN hydrogel surfaces. **a**. The patterned region of DN hydrogel hardly exhibits fluorescence at 25 ºC. **b**. The patterned region was visualized when observed at a temperature that exceeds the lower critical solution temperature (LCST, 32 ºC) of PNIPAm, because the fluorescent molecule ANS exhibits strong fluorescence only in the hydrophobic environment. **c**. Molecular structures and schematic illustration of PNIPAm, ANS, NIPAm, and water.

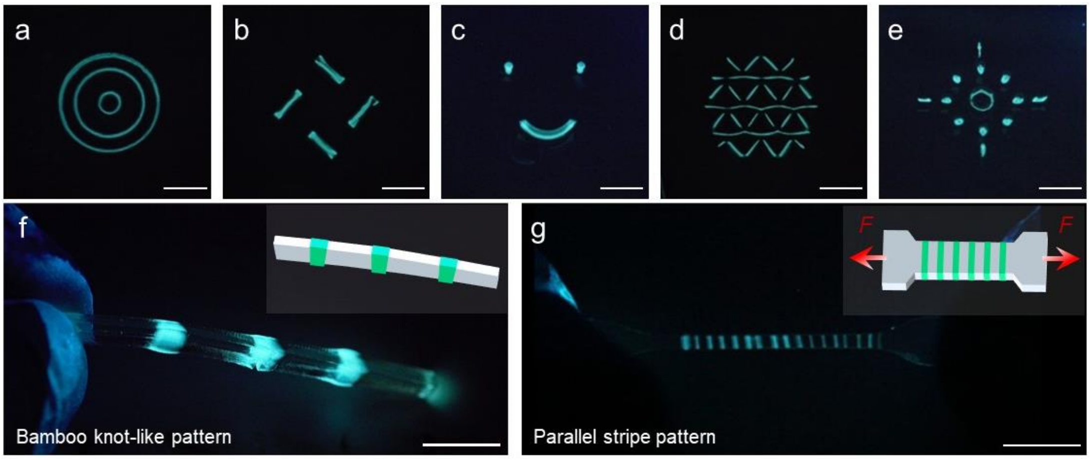

**Figure 6-6**. Programmable fluorescent patterns on DN hydrogel surfaces. **a-e**. Fluorescence images showing various complex PNIPAm-patterns on DN hydrogel surfaces. Scale bars, 5 mm. **f, g**. Programmable patterns in the DN hydrogel bulk. Insets, cartoon representation of the bamboo knot-like pattern and parallel stripe pattern under stretching. Scale bars, 10 mm.

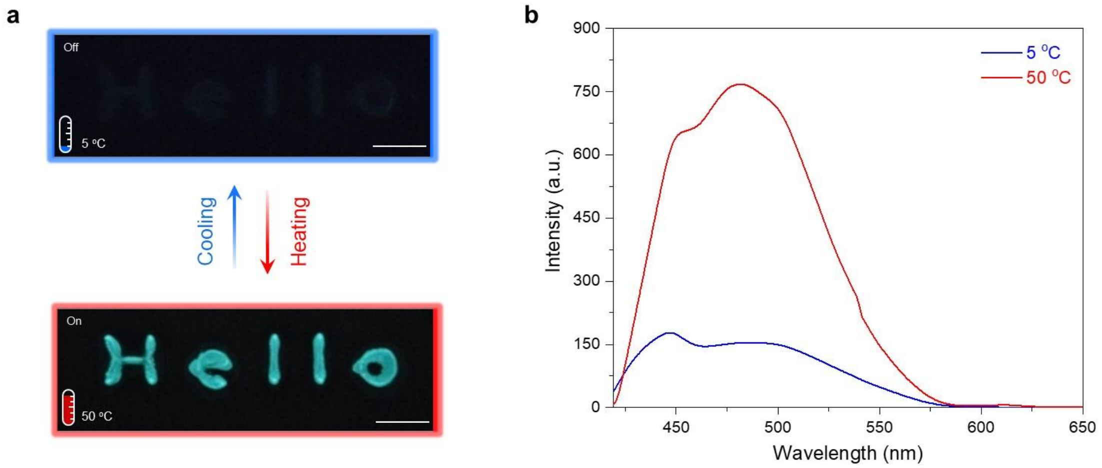

**Figure 6-7. a.** A fluorescent pattern that reads “Hello” for the stimulus-responsive display device. The left image highlighted with blue frame indicates weak fluorescence emission at low temperature (5 °C), the left image with red frame indicates strong fluorescence emission at high temperature (50 °C). The cyclic change of external temperature can trigger the on-off switching of fluorescence emission. Scale bars, 2.5 mm. **b**. Quantification of fluorescence intensity of the pattern region on DN hydrogel surface at different temperatures. Here, the excitation wavelength was 402 nm, the emission wavelength was from 414 nm to 650 nm. The hydrogel samples were held at a constant temperature (5 °C or 50 °C) for at least 30 minutes prior to the fluorescence intensity test.

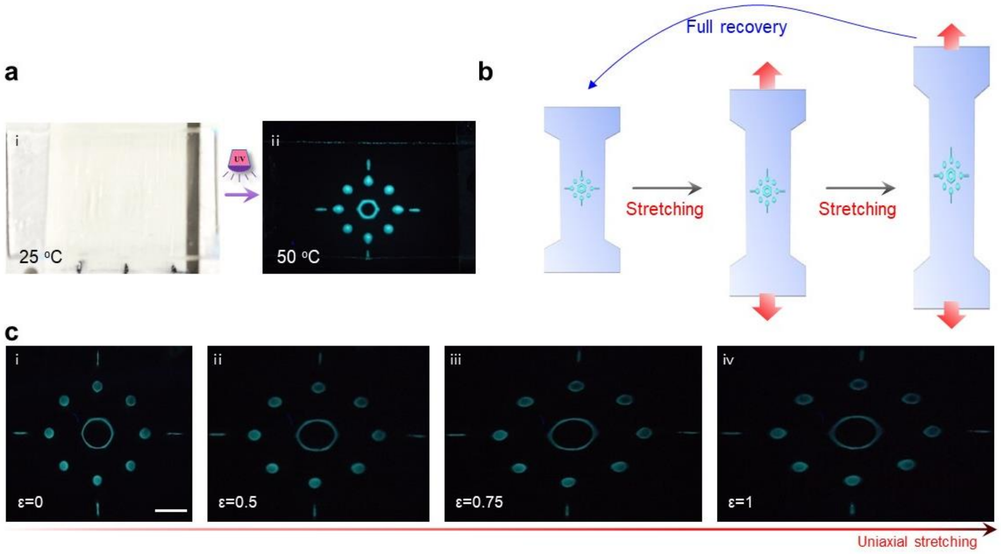

**Figure 6-8. a**. i PNIPAm-patterned DN hydrogels at 25 °C without UV irradiation. ii PNIPAm-patterned DN hydrogels at 50 °C under UV irradiation. **b**. Schematic illustration of the stretched patterned DN hydrogel, large stretchable and full elastic recovery. **c**. A PNIPAm-patterned DN hydrogel was uniaxially stretched to different strains ε, which can act as a stretchable display device. Here, concentration of NIPAm was 1.0 M for the patterning process. Scale bar, 5 mm.

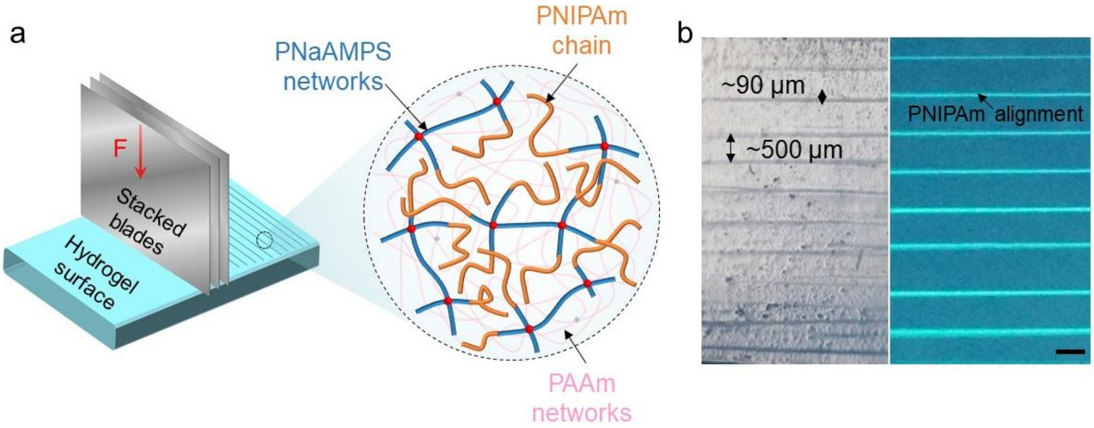

**Figure 6-9. a**. Schematic illustration of the regioselective indentation using stacked metal blades, the distance between the blades was controlled using silicone rubber spacers (spacer thickness of ~0.5 mm). **b**. Photo of the patterned DN hydrogel surface (left), fluorescent image showing where the newly formed PNIPAm alignments are (right). NIPAm 1.0 M was used for **b**.

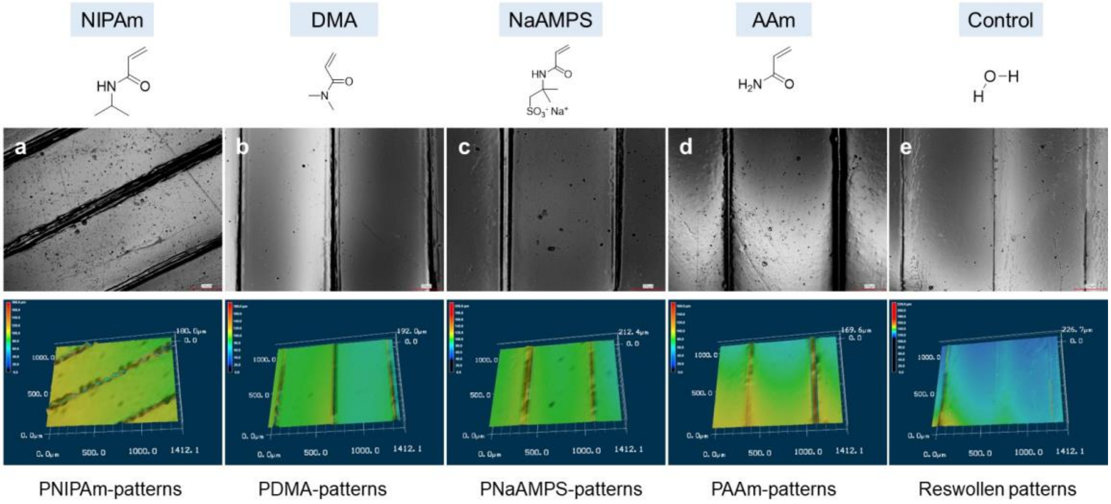

**Figure 6-10.** Surface observation of DN hydrogels with parallel patterns made by a stacked metal blade. Indentation depth was 1.0 mm. **a**. Images of the PNIPAm-patterned DN hydrogel surface (prepared in NIPAm solution, concentration of NIPAm was 1.0M). **b**. Images of the PDMA-patterned DN hydrogel surface (prepared in DMA solution, concentration of DMA was 1.0M). **c**. Images of the PNaAMPS-patterned DN hydrogel surface (prepared in NaAMPS solution, concentration of NaAMPS was 1.0M). **d**. Images of the PAAm-patterned DN hydrogel surface (prepared in AAm solution, concentration of AAm was 1.0M). **e**. Surface images of the DN hydrogel damaged in water (without monomer, control sample). The grown micropatterns were rough and have feature sizes, as shown in the three-dimensional images (bottom row). Scale bars, 200 μm.

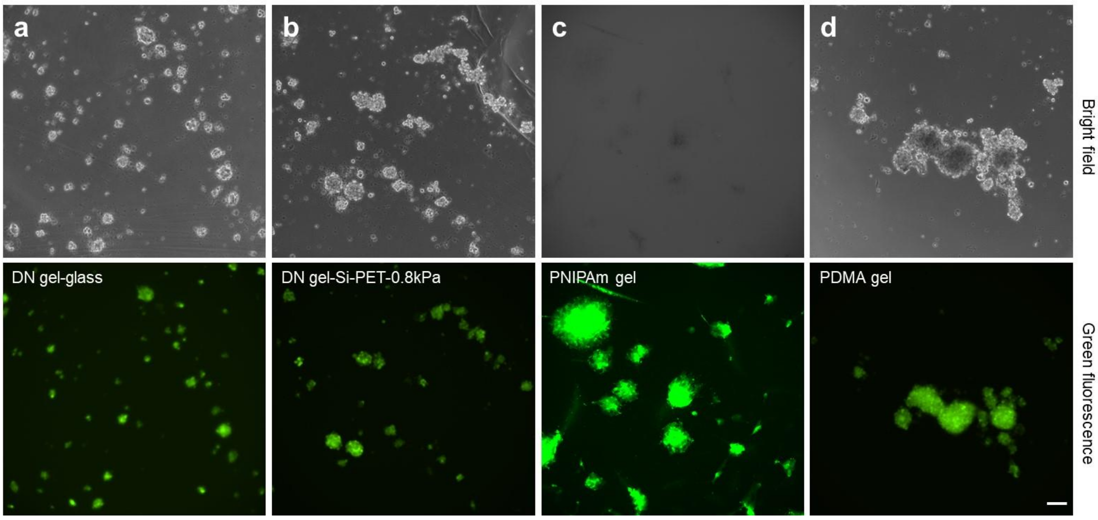

**Figure 6-11.** Morphology of cell clusters (C2C12) on different hydrogel substrates at 5 days culture. **a**. DN gel-glass. **b**. DN gel-Si-PET-0.8kPa. **c**. PNIPAm gel. **d**. PDMA gel. Scale bar, 100 μm.

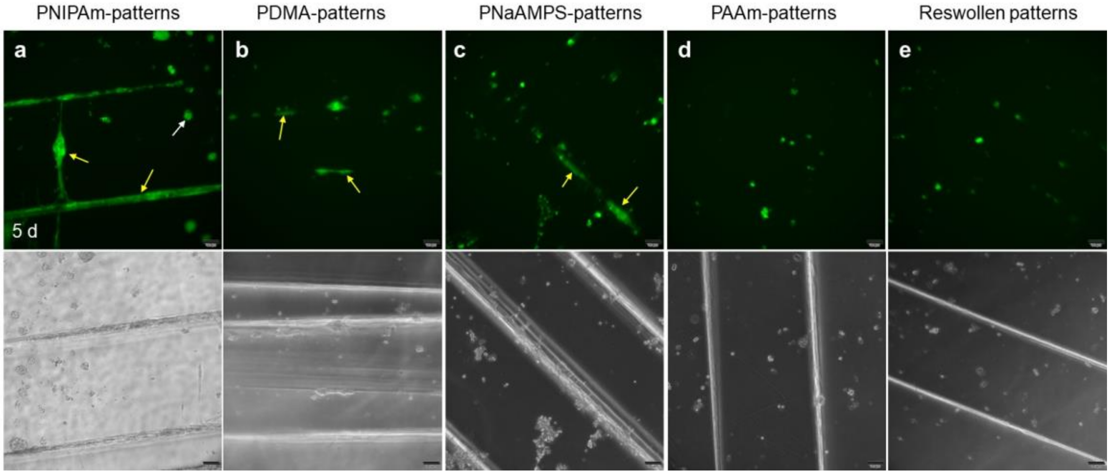

**Figure 6-12.** Differences in cell adhesion on different chemical micropatterns. **a**. PNIPAm-patterns. **b**. PDMA-patterns. **c**. PNaAMPS-patterns. **d**. PAAm-patterns. **e**. Reswollen patterns. Images were obtained after 5 days of cell culture. Scale bars, 100 μm.

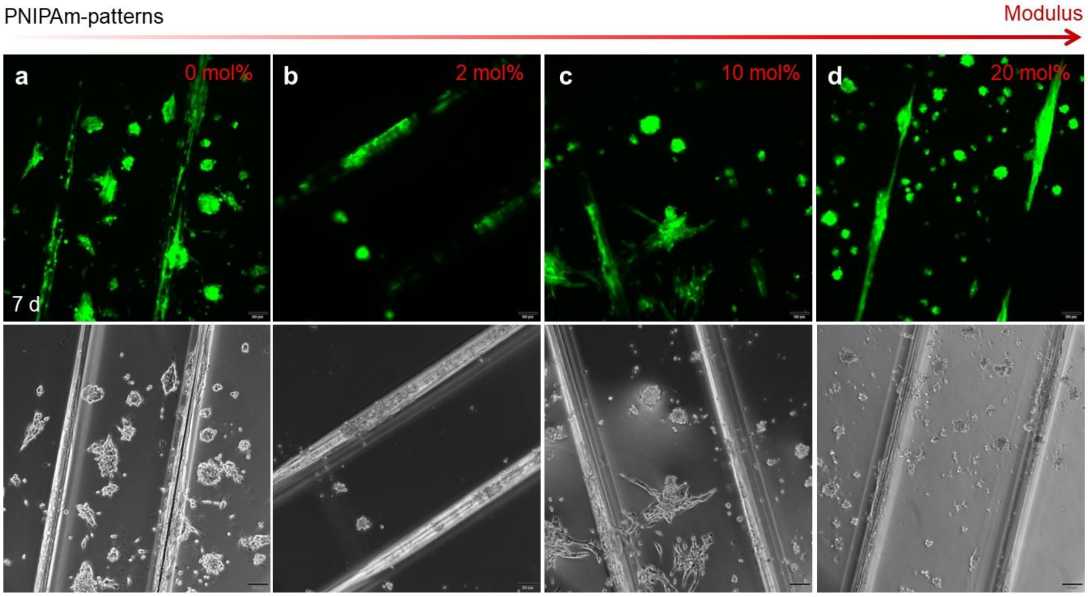

**Figure 6-13**. Effects of microstructure modulus on cell adhesion. Here, the modulus of microstructures can be tuned by changing the ratio of crosslinker to monomer. **a**. 0 mol% crosslinker to monomer. **b**. 2 mol% crosslinker to monomer. **c**. 10 mol% crosslinker to monomer. **d**. 20 mol% crosslinker to monomer. NIPAm 1.0 M was used for the PNIPAm-pattern preparation. Myoblast cells (C2C12) labelled with a green fluorescence protein (GFP) were cultured at 37 $^{o}$C for 7 days. Scale bars, 100 μm.

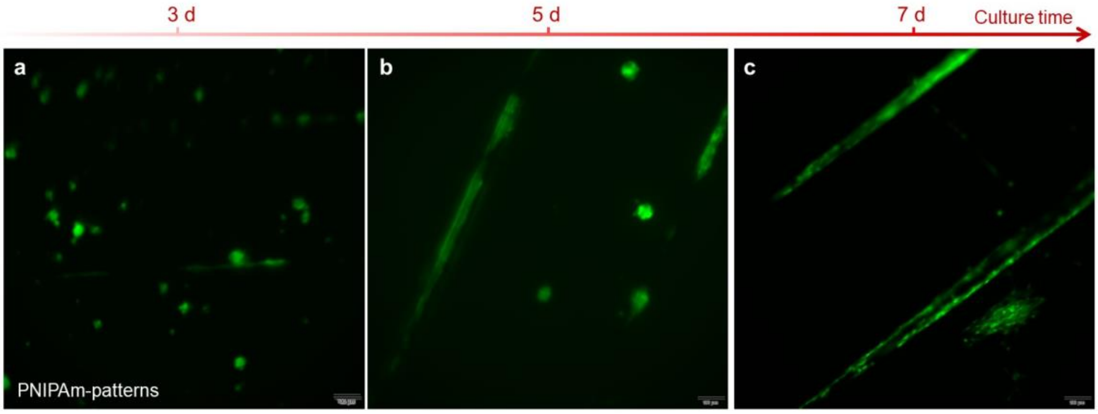

**Figure 6-14.** The increase in fluorescence intensity on the micropattern indicates that the amount of adhered cell on PNIPAm-patterns increases with culture time. Here, the increase in amount of cell adhered on PNIPAm-patterns is mainly due to cell proliferation over culture time. **a**. 3 days. **b**. 5 days. **c**. 7 days. Scale bars, 100 µm.

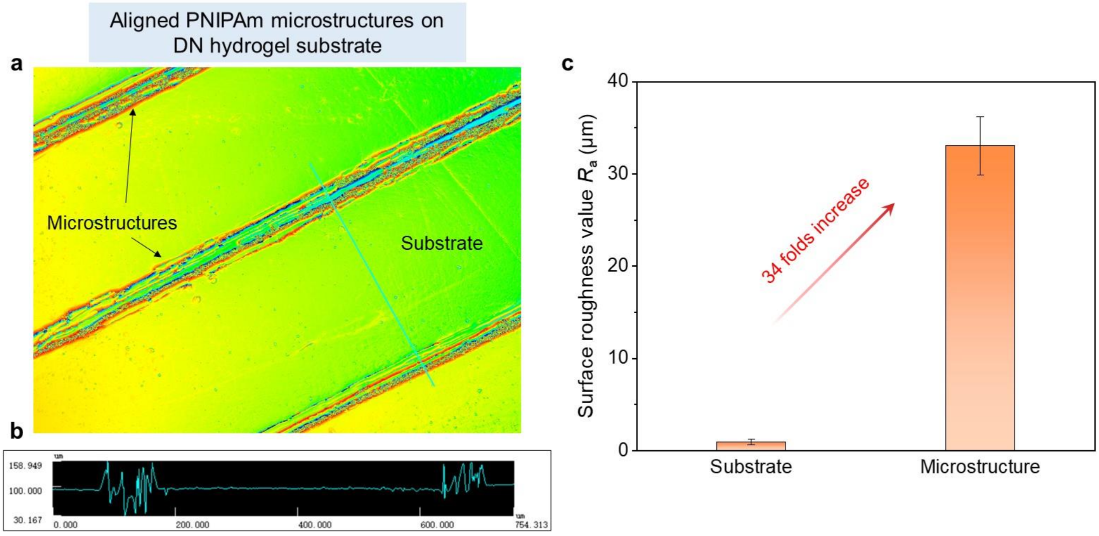

**Figure 6-15.** Surface topography and roughness of the micropatterned hydrogel surface. **a**. Three-dimensional image of the micropatterned hydrogel surface. **b**. Profile of the alignment microstructures. **c**. Surface roughness comparison of the hydrogel substrate and microstructures.

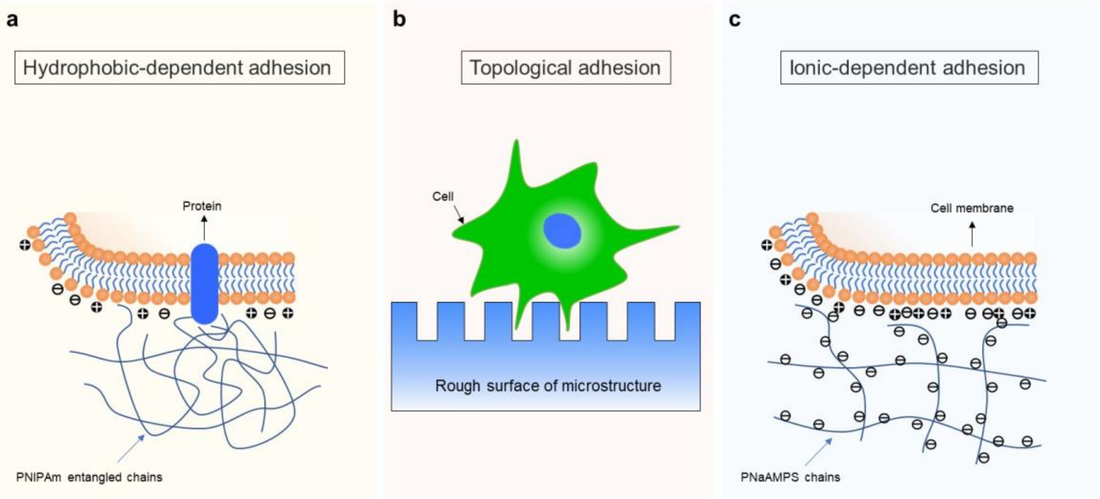

**Figure 6-16**. Schematic illustration of the origin of adhesion between cell and microstructure. The cell surface is composed of a bilayer of phospholipids with both negative and positive charges. **a**. The hydrophobic-dependent adhesion between cell and PNIPAm patterns. **b**. Topological adhesion between cell and the rough surface of microstructures. **c**. The ionic-dependent adhesion between cell and the negatived charged PNaAMPS patterns.

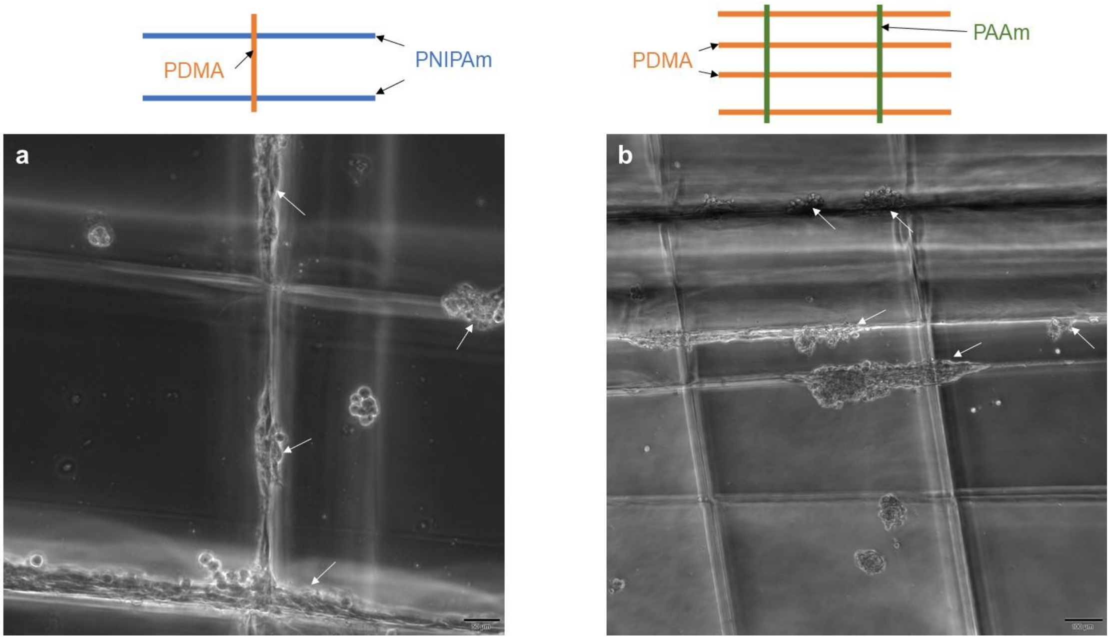

**Figure 6-17**. Selective adhesion of cells on the micropatterns. **a**. Hydrophobic PNIPAm and PDMA patterns induce cell adhesion. **b**. Hydrophobic PDMA patterns induce cell adhesion, but the hydrophilic PAAm patterns cannot induce cell adhesion.

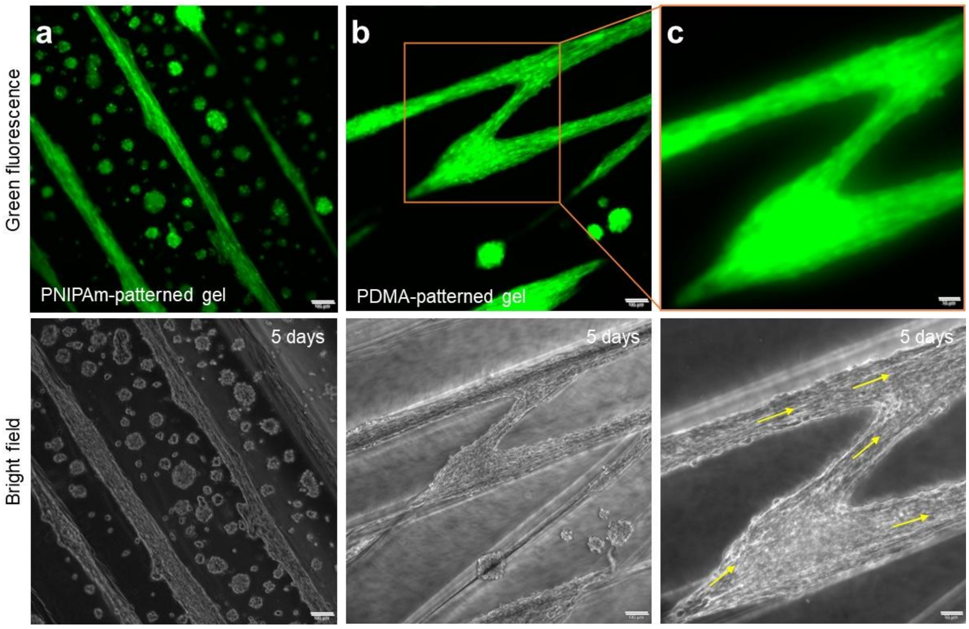

**Figure 6-18.** Cell adhesion and orientation on these hydrophobic patterns. **a**. Fluorescent and bright field microscope images of cells (C2C12) cultured on PNIPAm-patterned hydrogel. **b**. Fluorescent and bright field microscope images of cells (C2C12) cultured on PDMA-patterned hydrogel. Scale bars, 100 μm. **c**. Enlarged area of crossed cell patterns, which shows the elongated cell morphology. Scale bars, 50 μm.

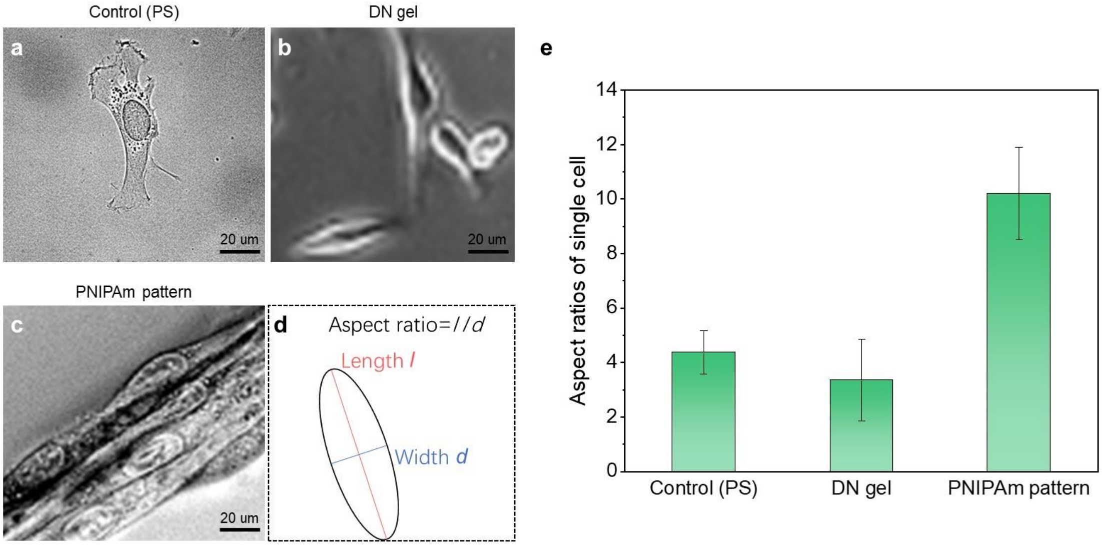

**Figure 6-19.** Cell morphology on different substrates. **a**. Control (Polystyrene, PS). **b**. DN gel. **c**. PNIPAm pattern. **d**. Schematic of cell aspect ratio. **e**. Comparison histogram of cell aspect ratio on different substrates. Error bar represents the standard deviation for three replicates. Data in **e** are presented as mean values +/- standard deviation (SD).

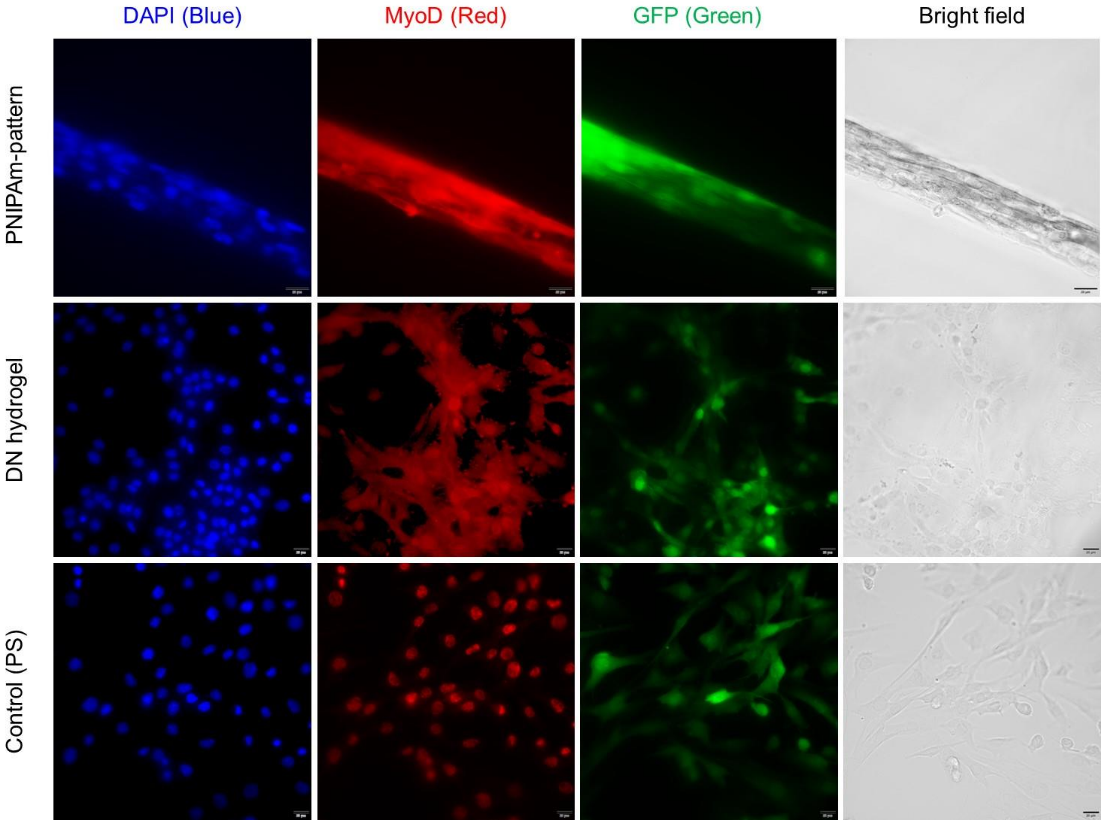

**Figure 6-20**. Cell morphology and protein expression identified by molecular marker immunostaining after culture for 7 days on different surfaces.

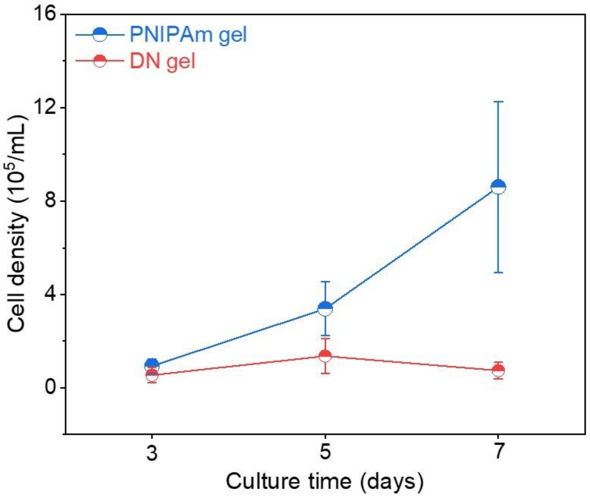

**Figure 6-21.** Cells can proliferate rapidly on the surface of PNIPAm hydrogel. Proliferation of cells is inhibited on the surface of DN hydrogel.

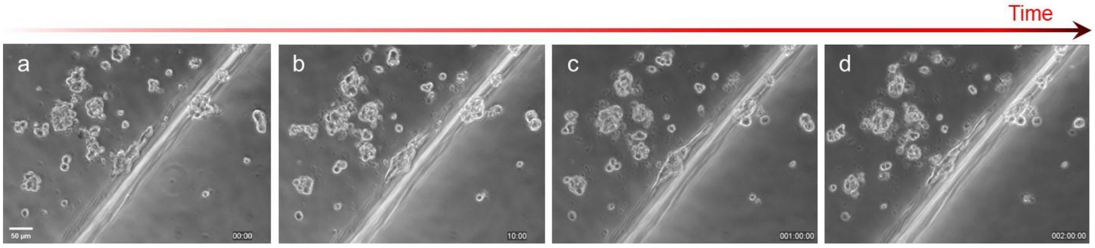

**Figure 6-22.** Real-time observation of cell elongation on the PNIPAm pattern. **a**. 0 min. **b**. 10 min. **c**. 1 day. **d**. 2 days.

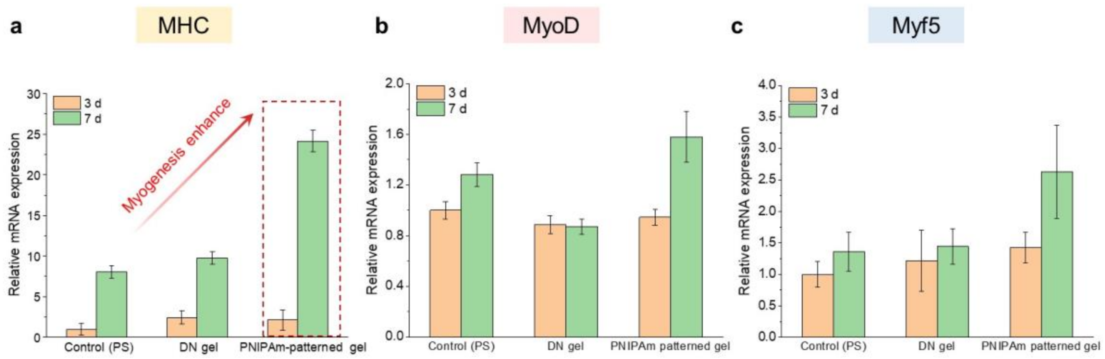

**Figure 6-23**. Myogenic gene expressions by muscle cells grown on control plates (PS), DN gel, PNIPAm-pattern gel scaffolds after culture in media for three and seven days. The expression was relative to the GAPDH expression. Error bar represents the standard deviation for three replicates. Data in **a, b** and **c** are presented as mean values +/- standard deviation (SD).

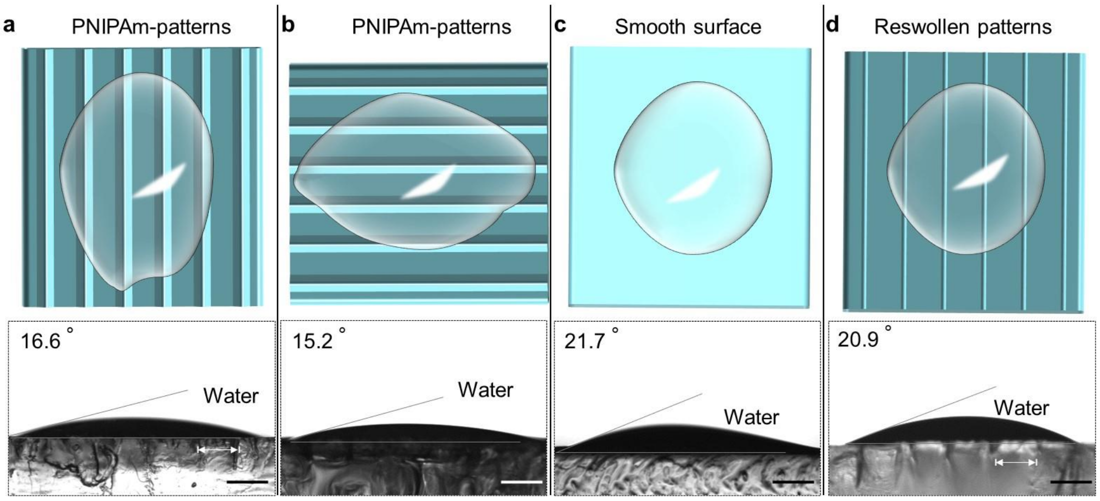

**Figure 6-24. a-d**. Illustrations of water droplet (upper arow) and optical images of static water contact angles (lower row) on different hydrogel surfaces placed horizontally. The white arrows in optical images in a and d indicate the distance (~500 μm) between the two stripes of patterns. The water droplet was 10 μL, room temperature 25 °C. Scale bars, 500 μm.

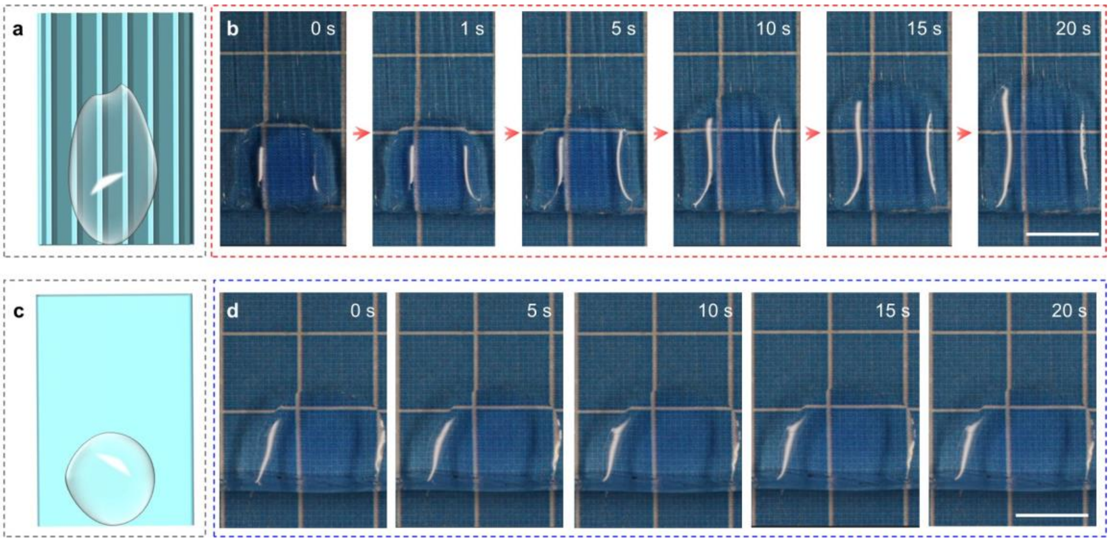

**Figure 6-25. a.** Schematic illustration of water droplet directional movement on parallel PNIPAm-patterned DN hydrogel surface. **b**. Time sequential snapshots to show the dyed water droplet directional movement on parallel patterned DN hydrogel surfaces. Here, the patterned DN hydrogel was placed horizontally on the table. **c**. Schematic illustration of water droplet directional movement on smooth flat DN hydrogel surface. **d**. Time sequential snapshots to show the dyed water droplet directional movement on smooth flat DN hydrogel surface. Here, the PNIPAm-patterned and smooth DN hydrogels were placed horizontally on a table, the morphology of the water droplets is observed by an in-situ camera. Scale bars, 5 mm.

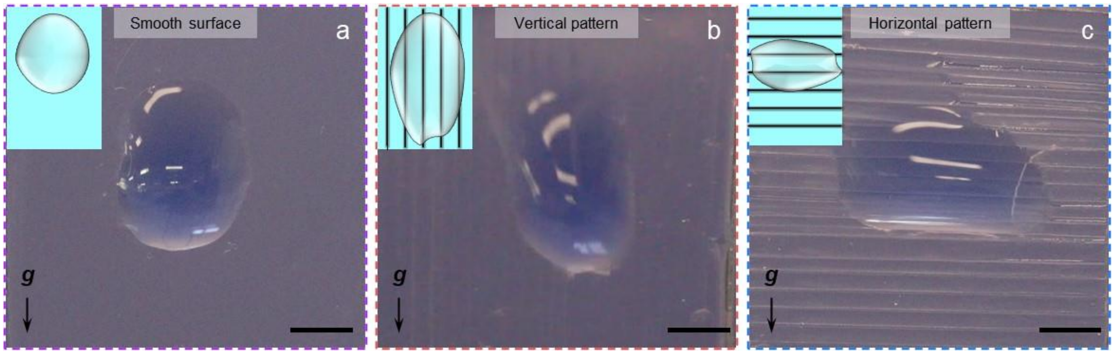

**Figure 6-26. a.** Schematic illustration of water droplet directional movement on parallel PNIPAm-patterned DN hydrogel surface. **b**. Time sequential snapshots to show the dyed water droplet directional movement on parallel patterned DN hydrogel surfaces. Here, the patterned DN hydrogel was placed horizontally on the table. Scale bars, 5 mm.

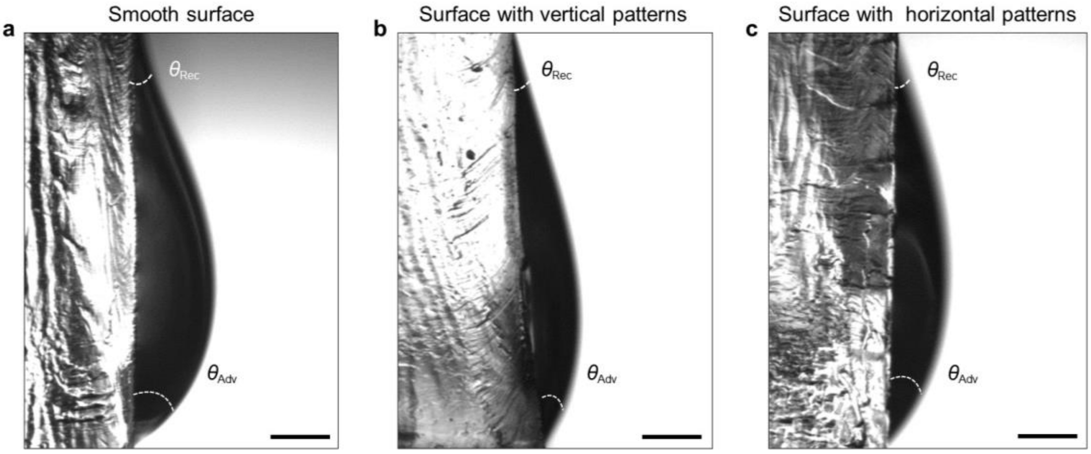

**Figure 6-27.** Contact angle hysteresis and sliding angle of water droplets on different hydrogel surfaces. **a**. Smooth surface (advancing angle is 50$^o$, receding angle is 20$^o$). **b**. Vertical pattern (advancing angle is 30$^o$, receding angle is 15$^o$). **c**. Horizontal pattern (advancing angle is 42$^o$, receding angle is 12$^o$). The advancing and receding angles for the water droplet. Scale bars, 500 μm.

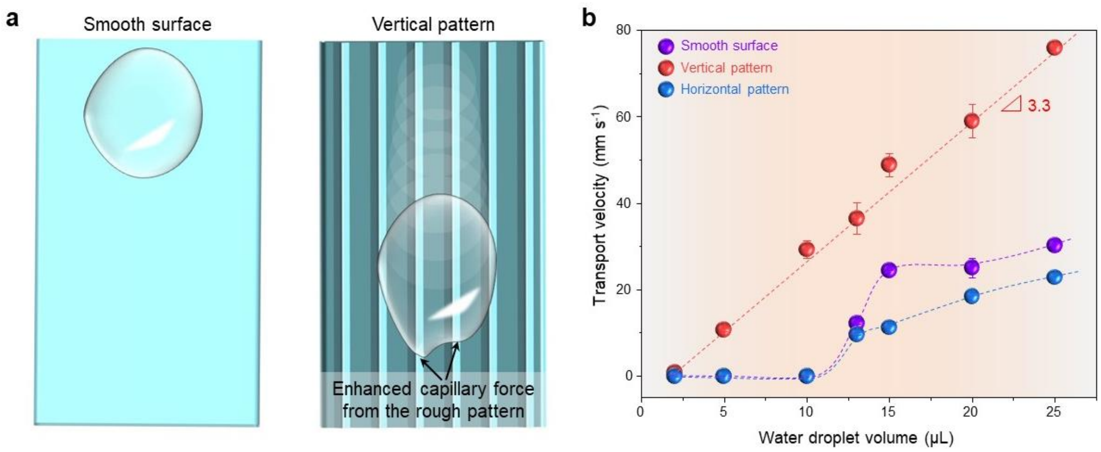

**Figure 6-28**. **a**. Schematic of water droplet transportation on the smooth hydrogel surface and hydrogel surface with vertical patterns (NIPAm 1.0 M was used), the rough pattern was benefit for water wetting and directional transport due to the enhanced capillary force. **b**. Dependence of transport velocity on water droplet volume for different hydrogel surfaces, there was a critical value around 10 μL for smooth surface and horizontal pattern. However, the transport velocity was a linear function of water droplet volume for vertical pattern (Slope, 3.3 mm s$^{-1}$ μL$^{-1}$). Error bar represents the standard deviation for three replicates. Data in **b** are presented as mean values +/- standard deviation (SD).

# Chapter 7: General Conclusions and Outlook

Inspired by living organisms, we present a force stamp method to grow microstructures on the surface of hydrogels based on a force-triggered polymerization mechanism of double-network (DN) hydrogels. This dissertation has described the essential issues and strategies to realize the growing microstructures on hydrogel surfaces through productive chemistry remodeling.

First, I carefully reviewed the current trend of polymeric materials especially on the productive mechanochemistry in materials. Given the progress and big challenges on the productive mechanochemistry in traditional hydrogel materials, I focused on an essential issue in this research, that is, the precise regulation of microstructures growth on tough hydrogel surfaces through the productive mechanochemistry. In a DN hydrogel, the force-triggered chemical reaction could be well-controlled by macroscopic force and the reaction could be highly efficient. The stress concentration of the rigid and brittle network caused by bond breaking could be effectively suppressed by the presence of the soft and stretchable networks. Therefore, the force-activated bond breaking in a DN hydrogel does not cause catastrophic failure of the material, and the amount of bond breaking inside a DN hydrogel increases with the stress/strain imposed to the material.

To achieve the surface microstructures growth, a special DN hydrogel surface was used for the candidate material to achieve the force-triggered microstructures growth, because the rigid first network is exposed on the hydrogel surface, regioselective indentation induces the bond scission of the first network, reswelling of the damaged zone suggesting plenty of mechanoradicals are produced on the hydrogel surface.

To estimate the mechnaoradical concentration, Lake-Thomas analysis and Morse approximation were used to calculate the amount of bond scission. The energy balance concept give a rough estimation of mechanoradical concentration as $2.9\times10^{-5}$ M in the damaged zone. I also found that the contact damage to the hydrogel surface caused by the metal indenter induces a large amount of mechanoradicals.

Because a large amount of mechanoradicals is induced on the hydrogel surfaces, the radical is high enough for efficient radical polymerization on the DN hydrogels fed with monomers. Once re-immersed in pure water, the microstructures with different feature size and chemistry induced by mechanical force were achieved. In addition, as exemplified by mechanical force induced NIPAm and AAc polymerization at the selective area, diverse on-demand functions can be imparted by using the programmed force stamp.

To expand the potential applications of the micropatterned DN hydrogels, I have created aligned microstructures composed of different monomers on DN hydrogel surfaces. Myoblast cells (C2C12) were cultured on these DN hydrogel surfaces at 37 °C. Many cells were found to adhere preferentially and align on the regions with functionalized micropatterns. Our results further reveal that the cells on the micropattern exhibit elongated shapes along with the stripe-like patterns than those on the non-patterned regions that show spherical shapes. I also found that the preferential growth and elongation of the cells on the micropatterns are related to the presence of the hydrophobic polymers, not due to the surface topological effect brought by local internal damage of the DN hydrogel.

I also show that the anisotropic DN hydrogel surfaces with parallel PNIPAm patterns can be used for regulating surface wettability and water droplet directional transportation. When a droplet is placed on a vertically placed surface, whether it stays stationary or moves depends on the competition of wetting asymmetry of the droplet on the surface and gravity on the droplet.

The dissertation has opened the productive use of mechanical force to activate chemical bond formation on hydrogel surfaces, and the facile method is nicely distinct from other forms of lithography, many of which are not suitable to hydrogel patterning. I believe such a facile force-triggered patterning promotes the wide application of hydrogels in various fields.

# List of Publications

1. Qifeng Mu, Kunpeng Cui, Zhijian Wang, Takahiro Matsuda, Wei Cui, Hinako Kato, Shotaro Namiki, Tomoko Yamazaki, Martin Frauenlob, Takayuki Nonoyama, Masumi Tsuda, Shinya Tanaka, Tasuku Nakajima, and Jian Ping Gong. Force-Triggered Rapid Microstructure Growth on Hydrogel Surface for On-Demand Functions. *Nature Communications* **13**, 6213 (2022).

## Other original papers

2. Wei Cui, Yong Zheng, Ruijie Zhu, Qifeng Mu, Xiaoyu Wang, Zhisen Wang, Shengqu Liu, Min Li, and Rong Ran, "Strong Tough Conductive Hydrogels via the Synergy of Ion-Induced Cross-Linking and Salting-Out." *Advanced Functional Materials* **32**, 2204823 (2022).
3. Zhi Jian Wang, Julong Jiang, Qifeng Mu, Satoshi Maeda, Tasuku Nakajima, and Jian Ping Gong, "Azo-Crosslinked Double-Network Hydrogels Enabling Highly Efficient Mechanoradical Generation." *Journal of the American Chemical Society* **144**, 3154-3161 (2022).
4. Wei Cui, Ruijie Zhu, Yong Zheng, Qifeng Mu, Menghan Pi, Qiang Chen, and Rong Ran, "Transforming Non-adhesive Hydrogels to Reversible Tough Adhesives via Mixed-Solvent-Induced Phase Separation." *Journal of Materials Chemistry A* **9**, 9706-9718 (2021).
5. Qifeng Mu, Qingsong Zhang, Wen Yu, Mengling Su, Zhongyu Cai, Kunpeng Cui, Yanan Ye, Xiaoyun Liu, Lingli Deng, Bingjie Che, Ning Yang, Li Chen, Lei Tao, and Yen Wei, "Robust Multiscale-Oriented Thermoresponsive Fibrous Hydrogels with Rapid Self-Recovery and Ultrafast Response Underwater." *ACS Applied Materials & Interfaces* **12**, 33152-33162 (2020).

## Other written works

6. Qifeng Mu. Collection of Research Achievements of Professor Jian Ping Gong's Group at Hokkaido University in 2021, *Frontier Science of Polymer Materials,* 31th January 2021, https://mp.weixin.qq.com/s/UYBNSgpYv3N55r5qK5e3Cw.
7. Qifeng Mu. Recent Advances in Soft Matter Research: A Review of Research Work of Professor Jian Ping Gong's Group at Hokkaido University in 2020, *Frontier Science of Polymer Materials,* 28th December 2020, https://mp.weixin.qq.com/s/kQGwZ9ALLErlq3VohRHsug.

## Presentation in conferences related to doctoral dissertation

1. Qifeng Mu, Tasuku Nakajima, Jian Ping Gong, “Gradient of Molecular Brushes Grafted on DN Hydrogels in Response to Selectively Destructive Stress” The 7th International Life and Science Symposium (ILSS), Sapporo (Japan), November 1, 2019 (Poster presentation).

# Acknowledgements

My study at the Graduate School of Life Science of Hokkaido University will soon come to an end, at the completion of my doctoral graduation thesis, I wish to express my sincere appreciation to all those who have offered me invaluable help during the four years of my study in the Laboratory of Soft and Wet Matter.

Firstly, I would like to express my heartfelt gratitude to my supervisor, Professor Jian Ping Gong, and Professor Tasuku Nakajima for their constant encouragement and guidance. They have walked me through all the stages of the writing of this thesis. Without their consistent and illuminating instruction, this thesis could not have reached its present form.

Secondly, I should give my hearty thanks to all the other faculty members of the Laboratory of Soft and Wet Matter for their patient instructions in various courses and their precious suggestions for my study here.

Lastly, my thanks would go to my beloved family, especially my wife, for their loving consideration and great confidence in me all through these years. I also owe my sincere gratitude to my Japanese and Chinese friends in Sapporo, who gave me their help and time by listening to me and helping me work out my problems during the difficult course of the thesis.

Qifeng Mu

20th September 2022